Universal Quantum Viscosity in a Unitary Fermi Gas

by

Chenglin Cao

Department of Physics
Duke University

Date:_____

Approved:

_____
John Thomas, Supervisor

_____
Steffen Bass

_____
Robert Behringer

_____
Calvin Howell

_____
Ying Wu

Dissertation submitted in partial fulfillment of the
requirements for the degree of Doctor of Philosophy
in the Department of Physics
in the Graduate School of
Duke University

2012

ABSTRACT

Universal Quantum Viscosity in a Unitary Fermi Gas

by

Chenglin Cao

Department of Physics
Duke University

Date:_____

Approved:

_____
John Thomas, Supervisor

_____
Steffen Bass

_____
Robert Behringer

_____
Calvin Howell

_____
Ying Wu

An abstract of a dissertation submitted in partial fulfillment of
the requirements for the degree of Doctor of Philosophy
in the Department of Physics
in the Graduate School of
Duke University

2012

Abstract

Unitary Fermi gases, first observed by our group in 2002, have been widely studied as they provide model systems for tabletop research on a variety of strongly coupled systems, including the high temperature superconductors, quark-gluon plasmas and neutron stars. A two component ^{6}Li unitary Fermi gas is created through a collisional Feshbach resonance centered near 834G, using all-optical trapping and cooling methods. In the vicinity of the Feshbach resonance, the atoms are strongly interacting and exhibit universal behaviors, where the equilibrium thermodynamic properties and transport coefficients are universal functions of the density n and temperature T. Thus, unitary Fermi gases provide a paradigm to study nonperturbative many-body physics, which is of fundamental significance and crosses several fields.

This dissertation reports the first measurement of the quantum shear viscosity in a ^{6}Li unitary Fermi gas, which is also the first measurement of a transport coefficient for a unitary Fermi gas. While equilibrium thermodynamic quantities have been theoretically and experimentally studied for the past few year, the measurement of a transport coefficient for a unitary Fermi gas provides new challenges for state of the art nonperturbative many-body theory as transport coefficients are more difficult to calculate than equilibrium thermodynamic quantities.

Two hydrodynamic experiments are employed to measure the shear viscosity η in different temperature regimes: anisotropic expansion is used for the high tem-

perature regime and radial breathing mode is employed for the low temperature regime. In order to consistently and quantitatively extract the shear viscosity from these two experiments, hydrodynamic theory is utilized to derive universal hydrodynamic equations, which include both the friction force and the heating arising from viscosity. These equations are simplified and solved by considering the universal properties of unitary Fermi gases as well as the specific conditions for each experiment.

Using these universal hydrodynamic equations, shear viscosity is extracted from the anisotropic expansion conducted at high temperatures and the predicted $\eta \propto T^{3/2}$ universal scaling is demonstrated. The demonstration of the high temperature scaling sets a benchmark for measuring viscosity at low temperatures.

For the low temperature breathing mode experiment, the shear viscosity is directly related to the damping rate of an oscillating cloud, using the same universal hydrodynamic equations. The raw data from the previously measured radial breathing experiments are carefully analyzed to extract the shear viscosity. The low temperature data join with the high temperature data smoothly, which yields the full measurement of the quantum shear viscosity from nearly the ground state to the two-body Boltzmann regime.

The possible effects of the bulk viscosity in the high temperature anisotropic expansion experiment is also studied and found to be consistent with the predicted vanishing bulk viscosity in the normal fluid phase at unitarity.

Using the measured shear viscosity η and the previously measured entropy density s, the ratio of η/s is estimated and compared to a string theory conjecture, which suggests that $\eta/s \geq \hbar/4\pi k_B$ for a broad class of strongly interacting

quantum fluids and defines a perfect fluid when the equality is satisfied. It is found that η/s is about 5 times the string theory limit, for a unitary Fermi gas at the normal-superfluid transition point. This shows that our unitary Fermi gas exhibit nearly perfect fluidity at low temperatures.

As presented part of this dissertation is the development of consistent and accurate methods of calibrating the energy and temperature for unitary Fermi gases. While the energy is calculated from the cloud dimensions by exploiting the virial theorem, the temperature is determined using different methods for different temperature regimes. At high temperatures, a universal second virial coefficient approximation is applied to the energy density, from which a variety of thermodynamic quantities, including the temperature, are derived in terms of the measured cloud size. For low temperatures, the previous calibration from the energy E and entropy S measurement is improved by using a better calculation of the entropy and adding constraints at high temperatures, using the second virial approximation. A power law curve with a discontinuous heat capacity is then fitted to the E-S curve and the temperature is obtained using $\partial E/\partial S$. The energy and temperature calibrations developed in this dissertation are universal and therefore can be applied to other thermodynamic and hydrodynamic experiments at unitarity.

For Bonnie Cao

Contents

List of Tables

List of Figures

Acknowledgements

I would like to begin by thanking my parents, who have been giving me endless and unconditional love ever since I was born. They give me true freedom to choose what I like to do and support me in all the aspects once I make my decision. I feel their love and care every minute. As their only kid, I owe them too much and I always feel bad about it. I want to let them know that I love them and I wish they can feel my love for them. Thanks for everything, Mom and Dad.

The next person to thank is my advisor Dr.John Thomas. If my parents have given me the largest impact on my personality, it is crystal clear to me that John has given the largest impact on my academic life. I joined John's group in 2007. Throughout the five year working with John, I am truly impressed by his enthusiasm, his passion, his knowledge, his perseverance and his kindness. He enlightens me and stimulates my interests in physics. He is dedicated to what he has been doing and his major and substantial contributions to this field have been widely recognized. More than that, he is a great teacher who is willing to teach and also knows how to teach his students. He cares about his students and runs his group as a family. John, I am privileged to have you as my advisor and I am very grateful to your seasoned guidance and help. Special thanks to you for the shoes auction joke you made on me. I will remember your New York accent and you 2 GB per second speaking speed and 10 GB per second thinking speed!

When I got into this cold atom field, I had no background in it and I was really

bad at pretty much everything related to the lab work. I was really worried that I might not be able to do any single experiment myself. Thanks to the former postdoc Jessie whom I had two year overlap with. Jessie taught me everything in the lab with patience, not only as a senior lab colleague but also as a true friend. I have absolutely no hesitations to say that it is Jessie who trains me and makes the lab transition so smoothly that I feel comfortable and confident to handle the system myself after he leaves our lab. Jessie, I feel so lucky to have had you as the postdoc when I was still a rookie student. I will always remember the "Jessie and Charles" show in the lab!

I am also indebted to Dr.Du. He is the former postdoc who worked on the other apparatus. Although we were not working on the same system, Du was willing to help me with all kinds of questions, no matter whether it is related to what he does. Besides the lab work, he encourages me in a variety of aspects and makes me feel that he is always here when I need help. Brother Du, thanks for all your help.

It is definitely crucial to have a great lab environment and good lab environment is created by every lab member. I am grateful to all the lab colleagues that I have worked with. When I joined John's lab, in addition to postdoc Jessie and Du, there are three senior graduate students: Le, Bason and James. It was Le who introduced me into John's group in 2007 and he has been as supportive as possible since then. Not only does he help me increase my knowledge in cold atom field, but also he shares all kinds of information with me and treats me as a true friend. Bason has great personality. Although I have only had one year overlapped with him in John's group, I feel that he is a reliable person that I can

really trust and get help from. James was a senior graduate student who worked on the same system when I began working in the lab and then he graduated and changed his role as a postdoc. James is a super smart guy and he also teaches me a lot in the lab. Yingyi, Ethan and Willie are the three graduate students who got into this lab roughly the same time with me. Ethan works on the same system with me and we have made progress together in the lab. Besides the lab work, he helps me improve my spoken English and increase my knowledge on the western culture. We also share with each other all the interesting stuff that belong to our age and constantly make jokes on each other. That was a lot of fun! Thanks! Ethan. Yingyi and Willie work on the other system. Yingyi, thanks for taking so many great pictures for our lab. Willie, thanks for giving me the nickname of Houzi but I think you are the real Houzi as well as a true friend of mine. In 2010, Haibin and Ilya joined our lab as postdoc. Haibin is a great and dedicated physicist and he knows a lot not only in experimental techniques but also theory. Ilya is always ready to help others and is very optimistic about everything he does. Besides the senior lab members I mentioned above, we also have Chinyun, Arum and Nithiya who will be the future of this lab. I am sure that they will have their success in this lab. Good luck guys and go JET labs!

Parents by chance and friends by choice. Thanks to Josh(A), Josh(K), Dong, Ivan, and Sam in my year. Thanks to Joel, Seth and Kristine from Dan's lab. Thanks to all the other friends. I am sorry that I cannot name you all here but I feel so lucky to know you and have you as my friends in my life. Long live the friendship!

I would like to thank all my committee members Dr.Bass, Dr.Beringer, Dr.Howell

and Dr.Wu. Thank you all for every suggestion and help. I also want to thank Dr.Liu for talking interesting physics and mathematics together and thank Dr.Gao for all the suggestions you gave me.

Finally, I dedicate my deepest love and appreciation to my fiancee Bonnie Cao. Your love gives me courage and confidence to face whatever defeat comes to me. If it were not you, it is impossible to make through every difficulty I have faced to reach this point. Darling, I will always love you and I dedicate the whole thesis to you!

Chapter 1

Introduction

The realization of Bose-Einstein condensation (BEC) in dilute atomic vapors [1–3] opened a door to a new era of exploring fascinating physics in a low temperature regime that has never been achieved before. Weakly interacting bosonic atoms are confined in a small volume and cooled to ultra-low temperatures where the quantum behavior dominates. The atomic density, temperature and interatomic interaction can be experimentally manipulated and controlled, which offers an unprecedented opportunity to study few-body and many-body quantum physics.

While the study of BECs is still actively ongoing, a new journey of making and understanding quantum degenerate ultra-cold Fermi gases has already begun. Quantum degeneracy occurs at ultra-low temperatures when particle wave packets start to overlap with each other. This is not a big problem for bosons (particles with integer spins) as they can crowd into the same quantum state to reach degeneracy and form condensates at sufficient low temperatures. However, fermions (particles with half-integer spin) tend to avoid sharing space with their neighbors as a consequence of the famous Pauli exclusion principle. Interestingly, this Pauli principle is expected to suppress three-body recombination rates, yielding an unique opportunity to achieve a stable strongly interacting degenerate Fermi gas. In contrast, a strongly interacting Bose gas is unstable due to three-body

collision. Therefore, it is important as well as challenging to create a quantum degenerate Fermi gas, especially a strongly interacting degenerate Fermi gas.

A weakly interacting degenerate Fermi gas was first made in 1999 [8] by virtue of the magnetic trap techniques first used for a BEC. It took even longer to find a way to incorporate strong interactions into a degenerate Fermi gas and make it experimentally stable and observable. In 2002, a strongly interacting degenerate Fermi gas was first observed by our group in a dilute two component ^{6}Li atomic vapor, using all-optical methods [7]. Fermionic atoms are cooled down to quantum degeneracy and the atomic interactions are dramatically enhanced through a collisional Feshbach resonance, which occurs by coupling the energy of two colliding atoms into a bound molecular state. In the vicinity of the Feshbach resonance, ultra-cold fermionic atoms are so strongly interacting that their s-wave collisional properties have no dependence on the microscopic details of the interaction potential and the particle species, leading to a strongly interacting system exhibiting universal behavior. Under this circumstance, the s-wave cross section reaches its largest possible value (unitary limit) $4\pi/k^2$, where the relative wave number of two colliding atoms k is set by the thermal de Broglie wavelength λ_T and the interparticle distance L. As a result, this regime is called the unitarity and the strongly interacting degenerate Fermi gas is also referred to as the unitary Fermi gas. Due to its universality, the unitary Fermi gas provides an effective and controllable table-top tool to model a variety of novel strongly coupled systems in nature, including quark-gluon plasmas in nuclear physics and neutron stars in astrophysics.

The attainment of the strongly interacting degenerate Fermi gases not only permits the modeling of other strongly coupled systems in nature, but also enables

quantitative investigations of BEC and BCS theory over a wide variety range of physical conditions. Unitarity is reached through a collisional Feshabch resonance. On the one side of the resonance where the scattering length is positive, two fermions in different spin states can form a molecule with a size much smaller than the interatomic spacing so that they are tightly bounded. These molecules are essentially composite bosons, which can undergo BEC if cooled to sufficient low temperature to make the thermal de Broglie wavelength λ_T comparable to the interparticle spacing L. On the one side of the resonance, the s-wave scattering length is negative, which does not support bound molecules. Instead, cooled below a certain temperature, fermions in this regime can form the so-called Cooper pairs on top of a filled Fermi sea due to many-body effects. The Cooper pair is very loosely bounded with its typical size much larger than the interatomic spacing. When cooled down to sufficient low temperature, the coopers can flow without resistance on top of the Fermi sea, which give rise to fermionic superfluidity. The Copper pair arises from many-body effects, which involves a totally different physical picture compared to that of a BEC. However, it is clear that BEC is a special limit of BCS and BCS is also a special limit of BEC. At resonance, BEC molecules and BCS Copper pairs are intimately connected. As a result, this unitary regime, also referred to as BEC-BCS crossover, is of great significance and of broad interest for exploring fundamental quantum few-body and many-body physics.

This dissertation reports the first measurement of shear viscosity in a two component ^{6}Li unitary Fermi gas. In this chapter, I begin by discussing some basic concepts and properties of unitary Fermi gases in Section 1.1. I will try to leave detailed equations or complicated calculations for the following chapters and

only focus on the very basic issues that will give a flavor of what a unitary Fermi gas is and why it is so important. After that, I will briefly review the current progress in studying unitary Fermi gases over the past few years. In Section 1.2, I will discuss the definition of the shear viscosity in a classical fashion and then specifically put it into the context of a unitary Fermi gas, which will facilitate our understanding of the quantum viscosity measurements in the following chapters. As the motivation of studying the quantum viscosity, a string theory conjecture will be introduced and perfect fluidity will be defined in order to draw broad interest. Finally, Section 1.3 lists the organization of the whole thesis.

1.1 Unitary Fermi gases

A unitary Fermi gases was first created by cooling and trapping a two component dilute ^{6}Li atomic vapor using all-optical methods [7]. ^{6}Li is chosen over other possible atoms for two reasons. First, it has a board collisional (Feshbach) resonance, which permits the s-wave scattering length to diverge at specific magnetic field. Second, ^{6}Li has an unusually large and negative triplet scattering length even in absence of magnetic field. Hence, the critical temperature T_c for the superfluid transition is predicted to be high enough for experimental observations. As required by the Pauli exclusion principle, ultra-cold fermions in the same quantum state are not able to interact with each other, which makes it impossible to achieve degeneracy through evaporative cooling using only one-component Fermi gases. Therefore, two different ^{6}Li internal states are used instead.

Using well developed all-optical cooling and trapping techniques [12], we are able to lower the temperature of the atoms to well below μK, where quantum

degeneracy occurs. Quantum mechanically, due to the wave-particle duality, a particle with mass m and temperature T can be described by a wave packet with its characteristic size determined by the thermal de Broglie wavelength $\lambda_T = h/(\sqrt{2\pi m k_B T})$. In the classical regime, where the temperature is high and the density is low, this de Broglie wavelength λ_T is negligibly small compared to the particle size and the interparticle spacing. Hence, wave packets of different particles never overlap and the particle-like nature dominates. As we lower the temperature and increase the atomic density, the de Broglie wavelength starts to be comparable to the interparticle spacing $L = n^{-1/3}$, where n is the number density. This is when the phase space density $n\lambda_T^3 \sim 1$ and wave packets of different particles start to overlap with each other, leading to quantum degeneracy. Under this circumstance, the wave-like nature becomes important and quantum effects must be taken into account.

We should not be confused by the seeming inconsistency between the aforementioned diluteness of the gas and the desired high density to achieve quantum degeneracy. Actually, there are three length scales that need to be considered. The interatomic distance $L = n^{-1/3}$, the effective range r_0 of the interatomic potential and the thermal de Broglie wavelength λ_T. On the one side, the gas is dilute in the sense that the interatomic distance L is much larger than the effective potential range r_0. Once the interatomic distance L becomes comparable to r_0, the short range approximation breaks down and the collision process of two atoms explores the details of the interaction potential, which destroys the universality. On the other side, we increase the atomic density to make the interatomic distance L smaller and decrease the temperature to make the thermal de Broglie wavelength λ_T larger. Once $L \sim \lambda_T$, the quantum degeneracy is approached and

quantum effects start to dominate.

While cooling fermionic ^{6}Li atoms, we tune an external magnetic field to a collisional Feshbach resonance. In the vicinity of the Feshbach resonance, the s-wave scattering dominates at low temperatures and the scattering length is drastically enhanced and eventually diverges, leaving the system no dependence on the interaction strength. As mentioned before, the effective potential range r_0, usually on the order of 1 nm, is much smaller than the interatomic distance $L \sim 0.2\mu$m. Therefore, the collision process has no dependence on the microscopic details of the interaction potential and r_0 should not introduce any length scale into the system. As a result, there are only two natural length scales, the interparticle spacing L and the thermal de Broglie wavelength λ_T. If the temperature is substantially lowered, the thermal de Broglie wavelength λ_T eventually becomes much larger than L, leaving the interatomic distance L as the only length scale for the system.

When the interatomic distance L and the thermal de Broglie wavelength λ_T set the length scale for a unitary Fermi gas, all the local quantities should be dependent only on the density n and the local temperature T [27]. Hence, unitary Fermi gases are expected to exhibit universal behavior, which is independent of the atomic species and the interaction potential. As a result, the unitary Fermi gas provides us with an excellent paradigm to mimic and study other strongly coupled systems.

1.1.1 Motivation for studying unitary Fermi gases

Unitary Fermi gases produced in the laboratory can be connected to a number of strongly interacting systems ranged in a wide variety of fields. Some of these

strongly interacting system may be experimentally difficult to access or detect. Two systems that are currently of great interest are a quark-gluon plasma and a high temperature superconductor.

According to the standard model, there are 12 flavors of elementary fermions, six of which are quarks. Protons and neutrons, once believed to be elementary particles, are known to be decomposable into quarks. Quarks have a spin quantum number of 1/2 and are bound to other quarks through the exchange of gluons. At extremely high temperature $\sim 2 \times 10^{12}$ K, quarks and gluons can be separated to form a quark-gluon plasma. Such extreme conditions are rare, but believed to exist tens of μs after the Big Bang [66].

Recently, a quark-gluon plasma has been produced at the Relativistic Heavy Ion Collider (RHIC) at Brookhaven National Laboratory. Two gold ions are accelerated to 100 GeV per nucleon and then collide with one another, producing a plasma at 2×10^{12} K [66]. The resultant plasma is then released and exhibits very similar hydrodynamics, to the elliptic flow behavior observed in a unitary ^{6}Li Fermi gas produced in our lab, despite 19 orders of magnitude difference in temperature and 25 orders of magnitude difference in density. More interestingly, a quark-gluon plasma is believed to be a nearly perfect fluid, which is also predicted to be the case for a unitary Fermi gas. As a result, our unitary Fermi gas, which is easier to produce, manipulate and detect, can help us understand the properties of quark-gluon plasmas.

Another example is a high temperature superconductor. An ordinary metal has finite resistance due to the frequent collisions between electrons, resulting in dissipative heating when an electric current flows through. Normally, the resistance of a metal varies with its temperature. Below a certain critical temperature

T_c, however, the resistance of a metal can disappear and electric current can be transmitted through the metal with nearly 100% efficiency. This is known as a superconductor.

A superfluid flow was first discovered in 1911 by Onnes by cooling liquid ^{4}He down to $T_c = 4.2K$. Since then, tremendous efforts have been made to search for superconducting materials with higher critical temperatures. An experimental breakthrough was made in 1986 by Bednorz and Muller, who discovered superconductivity at 35 K in the compound $La_{2-x}Ba_xCuO_4$. The current record high critical temperature is around 180 K, still far from the room temperature. On the theory side, the first phenomenological theory of superconductivity was put forth by Fritz London and Heinz London, named London equations. In 1956, Cooper realized that fermions can form pairs via an arbitrary attractive interaction on top of a filled Fermi sea and then Bardeen, Cooper and Schrieffer (BCS) developed a full theory of superconductivity based on a new, stable ground state, for which pair formation was included in a self-consistent way. However, the exact mechanism for high temperature superconductivity still remains unclear.

An interacting Fermi gas can turn into a fermionic superfluid when cooled below a certain temperature. Unlike bosonic superfluidity, which allows all the atoms to collapse into their ground state, the Pauli exclusion principle prevents two identical fermions from occupying the same quantum state. However, as predicted by the BCS theory, fermions with a weak attractive interaction can form Cooper pairs on top of a filled Fermi sea due to many-body effects, resulting in a fermionic superfluid as an analogue to a superconductor in the solid state physics. BCS theory also predicts that the critical temperature and the pair binding energy in units of Fermi energy scale $\propto \exp\left[-1/(k_F|a|)\right]$, where a is the

scattering length. As a result, it is crucial to enhance the interatomic interactions in order to make the superfluid transition temperature experimentally accessible and observable. With the strongest possible interactions, a unitary Fermi gas provides a great opportunity to achieve fermionic superfluidity with the highest critical temperate, which may greatly facilitate the study of the high temperature superconductors.

The Cooper pairs formed in a unitary Fermi gas have its size comparable to the interparticle spacing, which is in a good analogue to the correlation size on order of the electron spacing for high temperature superconductors. More interestingly, both of these two systems have a pseudo-gap regime in their phase diagram. In this pseudo-gap regime, uncondensed pairs can be formed above the critical temperature and have their great impact on the microscopic properties of the system. For example, paired fermions do not obey Fermi statistics and therefore may suppress the Pauli blocking. If we scale the critical temperature T_c by its density dependent characteristic temperature T_F, the value of T_c/T_F is about 0.05 for the high temperature superconductor and 0.15 for the unitary Fermi gases. By scaling the Fermi temperature for a unitary Fermi gas to a condensed matter system where $T_F \sim 10^4\,\mathrm{K}$, the critical temperature T_c is $1500\,\mathrm{K}$, which is above the room temperature. As a result, it is hoped that studying the unitary Fermi gases can help physicist better understand the high temperature superconductor.

1.1.2 Recent experimental progress in studying unitary Fermi gases

The first degenerate Fermi gas was created in ^{40}K using double RF knife evaporative cooling in a magnetic trap [8]. A degenerate sample of ^{6}Li was created using

^{7}Li sympathetic cooling in a magnetic trap [9–11] and using evaporative cooling in an optical dipole trap [12, 13].

After the realization of a unitary Fermi gas in 2002 [7], both the thermodynamic and hydrodynamic properties have been intensely explored. As was envisioned for quite a long time, the demonstration superfluidity in a Fermi gas was a top priority once a unitary Fermi gas was realized. The observed anisotropic expansion for ^{6}Li atoms after release from an optical dipole trap in 2002 [7] unveiled the existing superfluid hydrodynamics. In 2004, evidence of superfluidity continued to emerge from different experiments, such as fast magnetic field sweep experiments [14,15], radial breathing mode experiments [16,17] and radio frequency spectroscopy [18]. In early 2005, thermodynamic measurements of the heat capacity showed a possible phase transition between normal and superfluid [28]. The experiment providing the most direct demonstration of superfluidity was the observation of quantized vortices in a rotating strongly interacting Fermi gas [19]. Quantized vortices were also observed on both BEC and BCS sides [19]. After that, superfluidity was also explored for spin imbalanced two-component unitary Fermi gases through the observation of normal and superfluid phase separation experiments [20, 21].

The thermodynamic variables, such as energy, pressure and entropy, have been measured for unitary Fermi gases using different experimental methods. The heat capacity measurements [28] involved a precise energy input technique based on changing the potential energy of the cloud using the release and recapture for a breathing mode. An empirical temperature was developed based on the similarities between the density profile of an ideal Fermi gas and a strongly interacting Fermi gas. As the first model-independent thermodynamic measurements for a

strongly interacting Fermi gas, the energy per particle was calculated from the measured cloud size by exploiting the virial theorem and the trap-averaged entropy per particle was determined by adiabatically sweeping the magnetic field from unitarity to a weakly interacting regime, for which the entropy can be calculated from the measured cloud size [29]. The measurements on the equation of state and the local thermodynamic variables are obtained from the direct density profile of the cloud [33, 34]. The global and local thermodynamic measurements are found to be in good agreement with the theory [31].

While the thermodynamic variables have been intensely explored, the transport properties present new challenges. Transport coefficients, including mass transport, heat transport and spin transport, are useful for understanding the hydrodynamics and unveiling the quasi-particle excitation and pair formation in a unitary Fermi gas. Experiments including collective modes [38] and rotating gas techniques [22], were designed to measure the shear viscosity for a unitary Fermi gas. However, none of them demonstrated the predicted high temperature scaling so that it was unclear whether viscosity was accurately measured. Hence, demonstrating the universal temperature scaling and observing the correct magnitude of viscosity at high temperatures were primary motivations for this thesis.

1.2 Quantum viscosity

The central topic of this dissertation is the measurement of quantum shear viscosity for a unitary Fermi gas. As discussed below, the viscosity of a unitary Fermi gas has natural units of $\eta \sim \hbar n$, where n is the number density. $\eta \sim 6000\hbar n$ for air and $\eta \sim 300\hbar n$ for water. For our unitary Fermi gas at low temperatures,

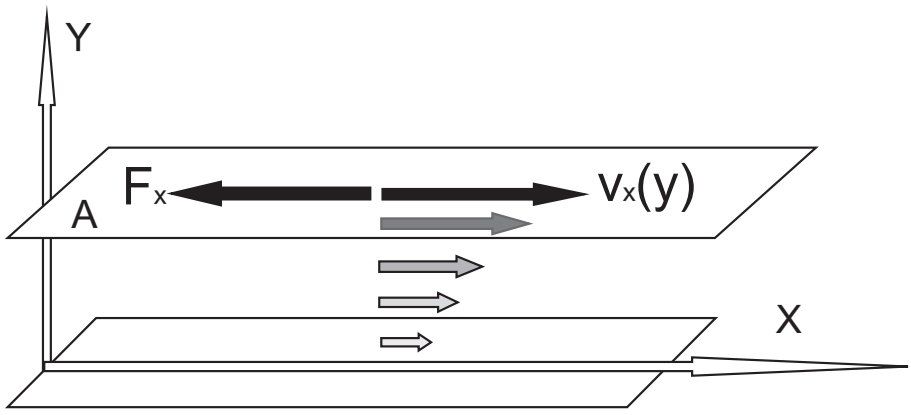

Figure 1.1: The definition of the shear viscosity [72]. A shear force per area in the x-direction F_x/A is related to the velocity gradient in the y-direction $\nabla_y v_x$ as $\frac{F_x}{A} = \eta \nabla_y v_x$. The proportionality parameter η is defined as the shear viscosity.

$\eta \sim 0.2\hbar\, n$. This is why it is referred to as quantum shear viscosity. Second, in classical fluid mechanics, viscosity can be decomposed into two different components: shear viscosity and bulk viscosity. This dissertation primarily focuses on shear viscosity, referred to as simply viscosity. Bulk viscosity is predicted to vanish at normal fluid phase for a unitary Fermi gas [45, 46] and it will also be briefly discussed at the end of this thesis.

1.2.1 Definition of viscosity

Viscosity exists everywhere in our daily life. Intuitively, viscosity characterizes the "stickiness" or "thickness" of a fluid. For example, oil has larger viscosity than water, as oil is stickier than water and therefore oil is harder to move than water. Physically, viscosity measures the reaction of a fluid to the applied stress. The shear viscosity determines the forces when a shear stress is applied. The bulk viscosity is related to the changing of the volume and vanishes for an incompressible flow.

Quantitatively, as shown in Fig. 1.1, shear viscosity is defined as the friction force F_x per unit area A created by a flow with a velocity gradient $\nabla_y v_x$

$$\frac{F_x}{A} = \eta \nabla_y v_x. \tag{1.1}$$

where η is the so-called shear viscosity coefficient or shear viscosity for abbreviation. The inverse of shear viscosity, $\phi = 1/\eta$, is called fluidity. Dimensional analysis shows that shear viscosity has dimensions of momentum per area. The CGS unit for viscosity is Poise ($1\,\text{Poise} = 1\text{g} \cdot \text{cm}^{-1} \cdot \text{s}^{-1}$).

The study of viscosity and transport phenomena can be dated back to Maxwell, who pointed out that the shear viscosity for a dilute gas is essentially the momentum transport of individual molecules. He also conducted experiments to show that the viscosity of an ideal gas is independent of density and depends only on temperature [81]. Viscosity can be estimated as [76]

$$\eta = \frac{1}{3} n\, p\, l_{mfp}. \tag{1.2}$$

where n is the density, p is the average thermal momentum of a molecule and l_{mfp} is the mean free path. The mean free path can be written as $l_{mfp} = 1/(n\sigma)$ where σ is some suitable transport cross section (For our unitary Fermi gas, it is the s-wave cross section). This implies that the viscosity $\eta \sim p/\sigma$ only depends on the temperature and is independent of density.

Below some critical temperature, gases condense into liquids or solids. For a liquid, the transport cannot be explained simply using the molecule picture. In this case, the temperature dependence of viscosity at low temperature is very complicated, which falls out of the scope of this thesis.

For a unitary Fermi gas characterized by a divergent s-wave scattering length at low temperatures [26] and a zero-range interacting potential, the only two natural length scales are the interparticle spacing L and the thermal wavelength λ_T as mentioned above. All the local thermodynamic and transport properties, including the shear viscosity, are universal functions of the density n and temperature T [27]. As discussed above, shear viscosity has units of momentum per area. For a unitary Fermi gas, the natural momentum is of order $\hbar/l$ and the natural area is l^2, yielding $\eta \propto \hbar/l^3$. The viscosity contains $\hbar$, which is the reason we define it as "quantum" viscosity. At temperatures well below the Fermi temperature where degeneracy occurs, the Fermi momentum sets the scale so $l \simeq L$, yielding $\eta \propto \hbar/L^3 \propto \hbar n$. At higher temperatures, above the degeneracy temperature, one expects that $l \simeq \lambda_T \propto \hbar T^{-1/2}$, so that the shear viscosity scales as $\eta \propto \hbar/\lambda_T^3 \propto T^{3/2}/\hbar^2$. This $T^{3/2}$ scaling is consistent with the well-known fact that the viscosity for a classical fluid depends only on temperature, but this result still depends on $\hbar$.

For a unitary Fermi gas in an equal mixture of two spin states, a variational calculation using the Boltzmann equation yields [36]

$$\eta = \frac{15 m^{3/2} k_B^{3/2}}{32\sqrt{\pi}\hbar^2} T^{3/2}, \tag{1.3}$$

where m is the atomic mass and k_B is the Boltzmann constant. More explicitly, Eq. 1.3 can be written as [36]

$$\frac{\eta}{\hbar\, n} = 2.77 \left(\frac{T}{T_F(n)}\right)^{3/2}, \tag{1.4}$$

where $T_F(n) = (\hbar^2(3\pi^2 n)^{2/3})/(2mk_B)$ is the local Fermi temperature. This im-

portant temperature scaling is experimentally demonstrated in this thesis for the first time. The derivation of this $T^{3/2}$ scaling is shown in Appendix using the Boltzmann equation following the method discussed in Ref. [101].

1.2.2 String theory conjecture

The measurement of the shear viscosity is currently of particular interest, not only as an important transport coefficient to characterize fluid properties of a unitary Fermi gas, but also in the context of a recent conjecture, derived using string theory methods. The conjecture states that for a broad class of strongly interacting quantum fluids, the ratio of the shear viscosity η to the entropy density s has a universal minimum [4]

$$\frac{\eta}{s} \geq \frac{1}{4\pi}\frac{\hbar}{k_B}, \tag{1.5}$$

where $\hbar$ is the Planck's constant h divided by 2π and k_B is the Boltzmann constant. Any fluid that saturates this string theory bound is defined as a perfect fluid [4]. Fluids that have η/s very close to this limit are called nearly perfect fluids. One good example of a nearly perfect fluid is a quark-gluon plasma produced in gold ion collisions at a temperature of 2×10^{12} K, which exhibits almost perfect frictionless flow and is thought to be a good approximation to the state of matter that exists microseconds after the Big Bang [66]. Another example is our two-component unitary Fermi gas at a temperature of 10^{-7} K, which is on totally the opposite side in terms of temperature and density as compared to a quark-gluon plasma. Despite of the huge differences in temperature and density, both systems exhibit nearly frictionless hydrodynamics and have a similar ratio

of η/s.

The scale of the ratio η/s can be understood using simple dimensional analysis. At temperatures well below the Fermi temperature where degeneracy occurs, $\eta \propto \hbar n$ as discussed above. For a normal fluid above the critical temperature, the scale of the entropy density $s \simeq n\,k_B$, yielding $\eta/s \simeq \hbar/k_B$. This η/s ratio also can be understood in terms of Heisenberg uncertainty principle. The shear viscosity is of order $\eta \propto n\,p\,l_{mfp}$, where n is the density, p is the average momentum and l_{mfp} is the mean free path. The Heisenberg uncertainty principle requires $p\,l_{mfp} \geq \hbar$, which yields $\eta \geq n\hbar$. In high energy physics, the total particle number is not always conversed. Hence, the ratio of the viscosity η to the entropy density $s \simeq n\,k_B$ is often used instead, yielding $\eta/s \simeq \hbar/k_B$.

For a unitary Fermi gas, the η/s ratio is experimentally accessible using hydrodynamic and thermodynamic experiments. The entropy and other thermodynamic properties have been measured both globally [28–32] and most recently, locally [33, 34]. Hence, by measuring the shear viscosity from hydrodynamic experiments [35–39] as reported in this thesis, the ratio of η/s can be estimated for a unitary Fermi gas and then compared to the string theory limit [37–39].

1.2.3 Significance of the current work

This dissertation presents a full measurement of the shear viscosity from nearly the ground state to the two-body Boltzmann regime in a unitary Fermi gas. This work is the first measurement of a transport coefficient in a unitary Fermi gas [39], which not only develops a variety of universal hydrodynamic equations and thermodynamic calibrations, but also enables experimental tests of theoretical predictions.

In order to extract viscosity from experiments, two hydrodynamic equations are derived from first principles, based on the universal properties of a unitary Fermi gas [39]. These two hydrodynamic equations, properly including the friction force and dissipative heating, are universal and therefore can be used for other hydrodynamic experiments at untairty.

Consistent and accurate methods of energy and temperature calibrations for a unitary Fermi gas are developed in this thesis. While the energy measurements consistently make use of the virial theorem, temperature determinations are based on the second virial approximation at high temperatures and the previous entropy-energy measurements at low temperatures. All these methods are universal and model-independent, and therefore can also be used to calibrate energy and temperature for experiments on universal fermi gases.

The predicted high temperature scaling of a transport coefficient is demonstrated for the first time in a unitary Fermi gas [39], which is in a good agreement with the theoretical predictions using Boltzmann equation and kinetic theory [36]. Similar high temperature scaling was also observed later in spin transport measurements [92]. Using the measured viscosity and the previously measured entropy density, the ratio of these two quantities are calculated and found to be approximately 5 times the string theory limit [39], which is consistent with theoretical predictions [65]. This shows that our unitary Fermi gas exhibits nearly perfect fluidity at low temperatures.

1.3 Dissertation organization

Chapter 2 studies the collisonal properties of cold ^{6}Li atoms, which lays out the experimental and theoretical foundations of studying a unitary ^{6}Li Fermi gas.

Chapter 3 summaries the general procedures for making and probing a unitary ^{6}Li Fermi gas, using all-optical methods that have been developed in our laboratory. In Chapter 3, the basic cooling and trapping techniques are introduced step by step along with the experimental setup that is used to realize these techniques in our lab. Towards the end of this chapter, the two hydrodynamic experiments are introduced aimed to measure quantum viscosity for a unitary Fermi gas at different temperatures: anisotropic expansion for the high temperature regime and radial breathing mode for the low temperature regime.

Basic hydrodynamic theory is covered in Chapter 4. This chapter derives both ideal hydrodynamics and dissipative hydrodynamic equations from first principles. Universal dissipative hydrodynamic equations are simplified and solved by considering the universal properties of unitary Fermi gases and the specific conditions for each hydrodynamic experiment. These equations are used to fit the data with the shear viscosity as the only free parameter.

Chapter 5 accurately calibrates the energy as well as the temperature for a unitary Fermi gas for different temperature regimes. The energy is consistently calculated for a harmonically trapped unitary Fermi gas from its cloud dimensions by exploiting the virial theorem. At high temperatures, the second virial coefficient approximation is used to determine the temperature also from the cloud dimensions. At low temperatures, the previous measured entropy and energy are used to generate a E-S curve and the temperature T is then determined by $T = \partial E/\partial S$. The calibrations developed in this chapter are universal and hence

can be used for other excitements at unitarity.

Chapter 6 reports the results of the two set hydrodynamic experiments. The predicted high temperature viscosity scaling is demonstrated using the anisotropic expansion experiment. The high temperature and low temperature data joins smoothly, which yields the full measurement of the shear viscosity from nearly the ground state to the two-body Boltzmann regime. The possible effect of bulk viscosity is also discussed. At the end of this chapter, the ratio of shear viscosity to the entropy density is estimated and compared to the string theory limit.

Finally, Chapter 7 offers a brief summary to this dissertation and provides an outlook for the future study on viscosity.

Chapter 2

Ultracold ^{6}Li Interactions

First observed in 2002 [7], strongly interacting degenerate Fermi gases have been produced with different atomic species using different techniques, all of which share a common procedure of tuning the atomic interaction through a collisonal Feshbach resonance. Achieving this Feshbach resonance requires a thorough understanding of the hyperfine structure and the collisonal properties of the atomic source. In our lab, we use ^{6}Li alkali atoms, which are the most commonly used source for making an ultra-cold Fermi gas. Section 2.1 provides a detailed study of the hyperfine structure of the ground state ^{6}Li atoms. The first excited state is also briefly mentioned in order to understand the optical transitions for the cooling process. After that, Section 2.2 discusses the collsional properties of the ultracold ^{6}Li atoms using basic scattering theory. Based on the results of the first two sections of this chapter, Section 2.3 introduces the collisonal Feshbach resonance for ^{6}Li atoms using a simple two channel explanation. When tuned in the vicinity of the Feshbach resonance, the so-called unitary regime is attained and the resultant Fermi gas exhibits universal behavior. At the end of this chapter, Section 2.4 derives a variety of basic properties for a unitary Fermi gas, including the density profile and the ground state energy.

2.1 Hyperfine States of ^{6}Li

Understanding the electronic structure of ^{6}Li atoms is of great importance for our experiments. In our lab, all the experiments are conducted using different hyperfine ground states of ^{6}Li in different external magnetic fields. Hence, understanding the Zeeman tuning of ^{6}Li energy levels is a prerequisite for us to do experiments on ^{6}Li atoms. Section 2.1.1 provides the details of the ground hyperfine states of ^{6}Li atoms. Section 2.1.2 briefly covers the hyperfine structure of the first excited state, which facilities our understanding of the optical transitions that can be used for the cooling process.

2.1.1 ^{6}Li ground state

A ^{6}Li atom has three protons, three neutrons and three electrons, which makes it a composite fermion. For a ground state ^{6}Li atom, the electronic structure is $1s^2 2s^1$ so that only one valence electron is in the 2s state. Hence, the total electron angular momentum, a sum of the orbital angular momentum L and the electron spin S, is $J = L + S = 1/2$ as $L = 0$ and $S = 1/2$ for a ^{6}Li atom in its ground state. The electrons create a magnetic field which interacts with the nuclear spin. As a result, the total electron angular momentum J is coupled to the nuclear spin I by the hyperfine interaction $\propto \mathbf{I} \cdot \mathbf{J}$ so that the total angular momentum of a ^{6}Li atom $F = J + I$. Since the nuclear spin is $I = 1$, the ground state presented in the absence of a magnetic field has a total angular momentum of $F = 3/2$ or $F = 1/2$.

In the presence of a magnetic field, these hyperfine states split. The interaction Hamiltonian that is used to describe these different hyperfine states can be written

as

$$H_{hf} = \frac{a_{hf}}{\hbar^2}\mathbf{S}\cdot\mathbf{I} - \frac{\mu_B}{\hbar}\left(g_s\,\mathbf{S} + g_I\,\mathbf{I}\right)\cdot\mathbf{B}, \tag{2.1}$$

where $a_{af}/\hbar = 152.14M\text{Hz}$ is the hyperfine constant for ^{6}Li and $\mu_B/h \approx 1.4M\text{Hz/G}$ is the Bohr magneton. $g_s = -2.002$ and $g_I = -0.000448$ are the total electron and nuclear g-factor [69], respectively. B is the external magnetic field applied on the atoms. Note that for this Hamiltonian, the good quantum numbers are determined by the magnetic field. For low field $a_{hf} \gg \mu_B B$, the first term in Eq. 2.1 dominates and the good quantum numbers are the total angular momentum F and its z-component projection m_Z. For the high field $a_{hf} \ll \mu_B B$, the second term dominates and the good quantum numbers are the z-component projections of electronic and nuclear spins, m_s and m_I.

Diagonalizing the interaction Hamiltonian Eq. 2.1 in the $|m_S\, m_I\rangle$ basis, we obtain the six orthogonal eigenstates

$$\begin{aligned}
|1\rangle &= \sin\Theta_+\,|1/2,\,0\rangle - \cos\Theta_+\,|-1/2,\,1\rangle && (2.2)\\
|2\rangle &= \sin\Theta_-\,|1/2,\,-1\rangle - \cos\Theta_-\,|-1/2,\,0\rangle && (2.3)\\
|3\rangle &= |-1/2,\,-1\rangle && (2.4)\\
|4\rangle &= \cos\Theta_-\,|1/2,\,-1\rangle + \sin\Theta_-\,|-1/2,\,0\rangle && (2.5)\\
|5\rangle &= \cos\Theta_+\,|1/2,\,0\rangle + \sin\Theta_+\,|-1/2,\,1\rangle && (2.6)\\
|6\rangle &= |1/2,\,1\rangle\,. && (2.7)
\end{aligned}$$

The six magnetic field dependent energy eigenvalues associated with these six

eigenstates are

$$E_1 = -\frac{1}{4}a_{hf} - \frac{1}{2}\,g_I\,\mu_B\,B - \frac{1}{2}\,a_{hf}\,R^+ \tag{2.8}$$

$$E_2 = -\frac{1}{4}a_{hf} + \frac{1}{2}\,g_I\,\mu_B\,B - \frac{1}{2}\,a_{hf}\,R^- \tag{2.9}$$

$$E_3 = \frac{a_{hf}}{2} + \frac{\mu_B\,B}{2}(2\,g_I + g_s) \tag{2.10}$$

$$E_4 = -\frac{1}{4}a_{hf} + \frac{1}{2}\,g_I\,\mu_B\,B + \frac{1}{2}\,a_{hf}\,R^- \tag{2.11}$$

$$E_5 = -\frac{1}{4}a_{hf} - \frac{1}{2}\,g_I\,\mu_B\,B + \frac{1}{2}\,a_{hf}\,R^+ \tag{2.12}$$

$$E_6 = \frac{a_{hf}}{2} - \frac{\mu_B\,B}{2}(2\,g_I + g_s). \tag{2.13}$$

The coefficients in Eq 2.2 through Eq 2.13 are defined as

$$\sin\,\Theta_\pm = \frac{1}{\sqrt{1 + \left(Z^\pm + R^\pm\right)^2/2}} \tag{2.14}$$

$$\cos\,\Theta_\pm = \sqrt{1 - \sin^2\Theta_\pm} \tag{2.15}$$

$$Z^\pm = \frac{\mu_B\,B}{a_{hf}}(-g_s + g_I) \pm \frac{1}{2} \tag{2.16}$$

$$R^\pm = \sqrt{\left(Z^\pm\right)^2 + 2}. \tag{2.17}$$

The energy tuning of these six eigenstates as a function of the magnetic field is shown in Fig 2.1. At zero magnetic field, the two ground state hyperfine levels of ^{6}Li atoms have an energy splitting $\hbar \times 228.2\,\mathrm{MHz}$. When a magnetic field is applied, states $|1\rangle$ through $|3\rangle$ decrease in energy as magnetic field increases. This behaviors is due to the fact that the total electronic magnetic moment is much larger than the total nuclear magnetic moment and therefore the energy eigenvalues for states $|1\rangle$ through $|3\rangle$ are dominated by $-a_{hf}R^+/2$, $-a_{hf}R^-/2$ and $-\mu_B B g_s/2$, all of which have a negative dependence on the magnetic field.

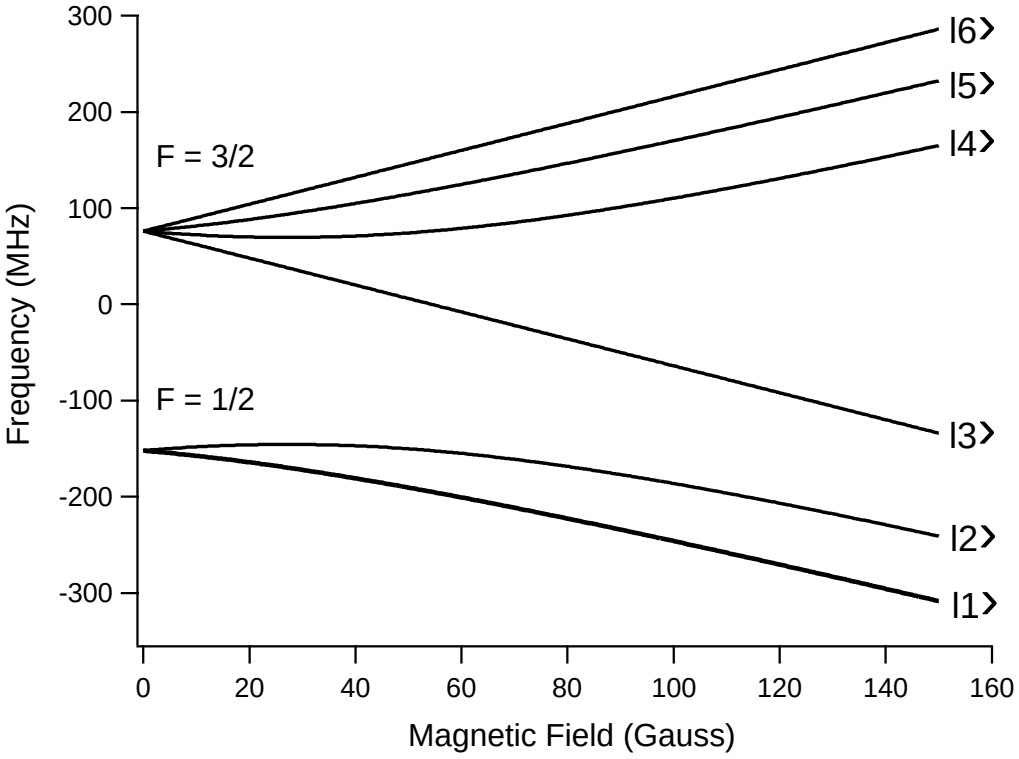

Figure 2.1: The hyperfine ground state energy levels as a function of the magnetic field for ^{6}Li [71]. The states are denoted as $|1\rangle$ through $|6\rangle$. We use an equal mix of the two lowest hyperfine states $|1\rangle$ and $|2\rangle$ for making a unitary Fermi gas.

As a result, their energies decrease as the magnetic field increases. For states $|4\rangle$ through $|6\rangle$, the situation is opposite, which makes their energies increase as the magnetic fields increases. The states $|1\rangle$ through $|3\rangle$, which have low energy at high magnetic field, are referred to as the high magnetic field seeking states and the states $|4\rangle$ through $|6\rangle$ are called the low magnetic field seeking states.

As well known, fermions obey the Pauli exclusive principle, which requires the total wave function to be anti-symmetric. In the low temperature regime, p-wave collision is suppressed because the the barrier height for ^{6}Li is approximately 8 mK, which is much higher than the temperatures we use [39]. As a result, s-wave collisions dominate at low temperatures. Since the wave function for s-wave collision is symmetric, an anti-symmetric spin wave function is required to make the total wave function anti-symmetric. We know that it is impossible to make an anti-symmetric spin wave function out of two fermions in the same states. Therefore, we need two different spin states.

In most of experiments in our laboratory, we use an equal mixture of the two lowest hyperfine states $|1\rangle$ and $|2\rangle$, which are both high magnetic seeking states and can be trapped using all-optical methods. There are two major reasons for us to choose there two states over other combinations. First of all, the two collisonal Feshbach resonances and a zero-crossing are experimentally accessible for a mixture of these two spin states. The broad Feshbach centered at 834 G is the primary one we use for our experiments. This broad Feshbach resonance, as indicted by the name itself, has a large width of 300 G and can be located easily. There is another Feshbach resonance located at approximately at 543 G with a much narrower width $\sim$ 0.1 G for the $|1\rangle$ and $|2\rangle$ mixture. These two Feshbach resonances will be discussed in Section 2.3. Besides these two Feshbach

resonances, a zero-crossing point located at 528 G is also available for these two spin states. When tuned at this zero-crossing, the atoms are non-interacting and the atomic gas is essentially ideal. Second, the mixture of states $|1\rangle$ and $|2\rangle$ is robust against inelastic collisions. In an s-wave collision, the z-component of the total angular momentum $m_F = m_I + m_s$ is conserved. If states $|1\rangle$ and $|4\rangle$ are chosen, collisions can make them decay into states $|1\rangle$ and $|2\rangle$, resulting in a large amount of releasing energy that is even larger than the temperature of the atoms. However, a system that starts with a mixture of the two lowest hyperfine states $|1\rangle$ and $|2\rangle$ can only end up in states $|1\rangle$ and $|4\rangle$, $|2\rangle$ and $|5\rangle$, $|4\rangle$ and $|5\rangle$ or $|3\rangle$ and $|6\rangle$, all of which are energetically forbidden because the starting temperature of the mixture (around 200 μK) is much less than the binding energy. As a result, the $|1\rangle$ and $|2\rangle$ mixture is more stable than other combinations of hyperfine states.

2.1.2 ^{6}Li first excited states

Having discussed the hyperfine structure of the ground state ^{6}Li atoms, the first excited state of ^{6}Li also needs to be briefly explored to understand the optical transitions for the cooling and trapping techniques.

A first excited state of ^{6}Li atom has a valence electron in the $2p$ orbit, which makes the orbital angular momentum $L = 1$. As a result, the total angular momentum of the electron can be either $J = L - S = 1/2$ or $J = L + S = 3/2$, resulting in a doublet $^2P_{1/2}$ and $^2P_{3/2}$. As shown in Fig. 2.2, the transition from the ground state $^2S_{1/2}$ to these two states are then refereed to as the D_1 line and the D_2 line, respectively. The frequency splitting between these two lines is 10.06 GHz, which is larger than any hyperfine transition frequencies. In our experiment, the D_2 line, with a linewidth 5.9 MHz, is used for cooling and imaging

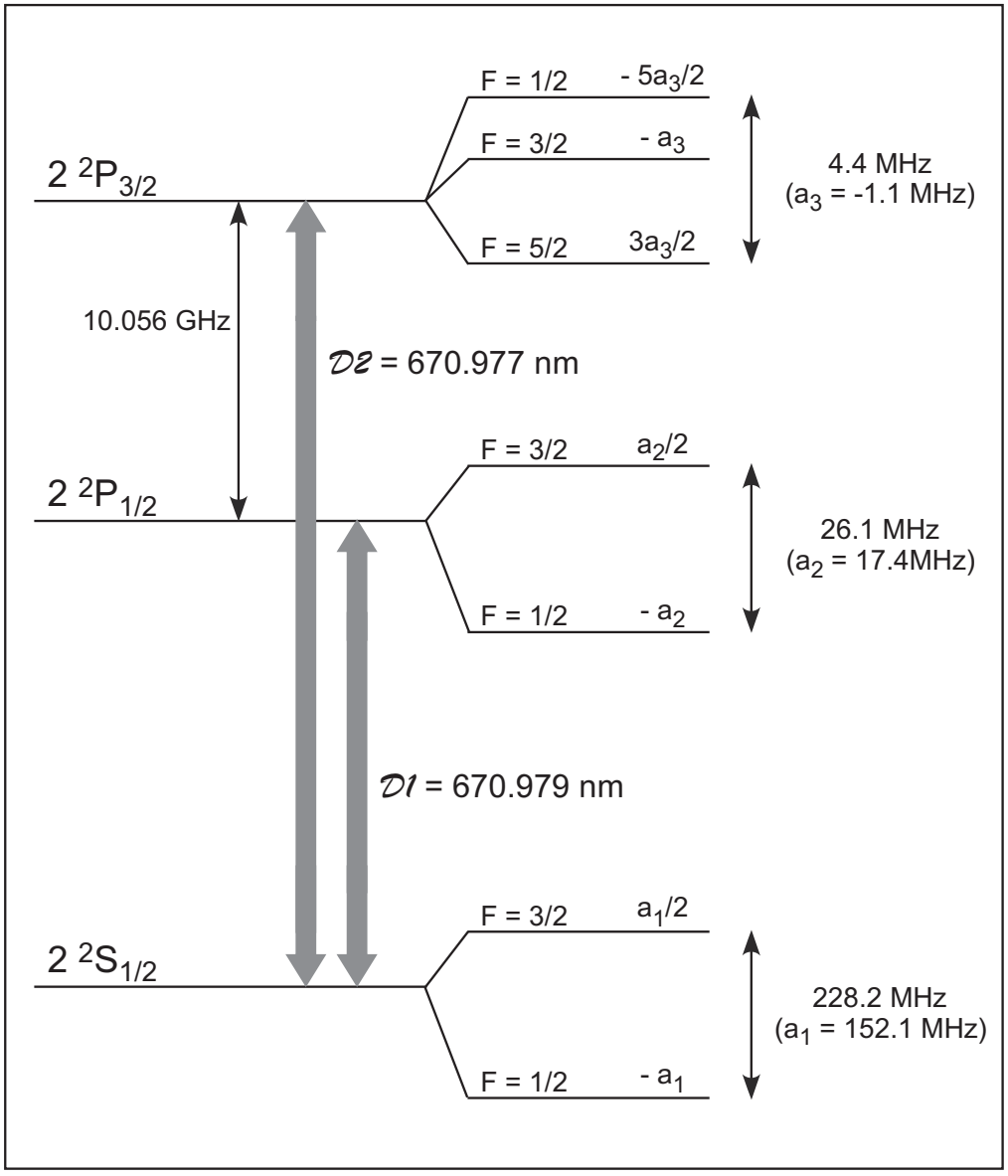

Figure 2.2: Energy level diagram of the ground and the first excited states of ^{6}Li at zero magnetic field [69]. The frequency gap between the D_2 and D_1 lines is 10.056 GHz. The D_2 line with its linewidth 5.9 MHz is used for cooling and imaging processes. This diagram is not to scale.

processes, which will be introduced in Chapter 3.

2.2 Collisional Properties of Ultracold ^{6}Li Atoms

Before delving into the origin of the collisional Feshbach resonance, we need some knowledge of the collisional properties for ^{6}Li atoms at low temperatures. Section 2.2.1 begins by introducing the fundamental scattering theory. Section 2.2.2 describes the partial wave expansion, which is crucial for us to understand the low temperature collisional properties. Using this s-wave scattering amplitude, the collisional cross section for a untiary Fermi gas is derived. Section 2.2.3 discusses the impact of the particle statistics on the collsional process. Section 2.2.4 defines the scattering length, which quantifies the interaction strength.

2.2.1 Basic Scattering Theory

In classical mechanics, the process of scattering involves individual incoming particles hitting the target with some impact parameter. The trajectory of the incoming particle will be affected by the interaction between the incoming particle and the target. The trajectory of every particle is well determined by Newton's law. For an ensemble of particles, the so-called differential cross section $d\sigma/d\Omega$ is defined as the scattering rate into an arbitrary solid angle $d\Omega$ divided by the incident particle flux. In the following discussion, we focus on finding the differential cross section for our ultracold ^{6}Li atoms.

For a dilute ensemble of ultracold atoms, atomic interactions are dominated by the van der Waals potential and the interparticle spacing $L = n^{-1/3}$ is much larger than the characteristic range of the van der Waals potential r_0. Under this

circumstance, the electrostatic interactions between atoms can be written as

$$V(r) = -\frac{C_6}{r^6}. \tag{2.18}$$

At large distances, the van der Waals potential is attractive as C_6 is positive. Note that the interaction potential is well described by Eq. 2.18 only when the interparticle spacing L is much bigger than the potential effective range r_0. Otherwise, electronic exchange dominates the atomic interactions, resulting in a strong short-ranged repulsive potential.

Let's now consider two colliding particles of equal mass m interacting through a potential $V(r)$, depending only on the distance between two particles as given in Eq. 2.18. The scattering of the two particles can be treated as the scattering of one particle of reduced mass $\mu = m/2$ by the potential $V(r)$ in the center of mass coordinate system.

For low temperature scattering, we write the wave function of the incoming particle as a plane wave $\psi_i = e^{ikz}$, where the $k = \sqrt{2\mu E}/\hbar$ is the incoming wave vector. The total wave function of the atom can be written as

$$\psi_{\mathbf{k}} = e^{ikz} + \psi_{sc}(r, \theta, \phi), \tag{2.19}$$

where e^{ikz} is the incoming wave and $\psi_{sc}(r, \theta, \phi)$ is the scattered wave. The incoming wave function can be expanded in terms of the the spherical harmonic functions as [89]

$$e^{ikz} = \sum_{l=0}^{\infty} i^l (2l+1) P_l(\cos\theta) j_l(kr), \tag{2.20}$$

where $P_l(\cos\theta)$ is the l^{th} Legendre polynomial

$$P_l(\cos\theta) = \left(\frac{4\pi}{2l+1}\right)^{1/2} Y_l^0, \tag{2.21}$$

and $j_i(kr)$ is the spherical Bessel function. In the limit $r \to \infty$, Eq. 2.20 has an asymptotic form as

$$e^{ikz} = \sum_{l=0}^{\infty} i^l (2l+1) P_l(\cos\theta) \frac{(\sin kr - l\pi/2)}{r}, \tag{2.22}$$

and the scattered part approaches a wave packet with some angular dependence. Hence, the total wave function Eq 2.19 takes the form

$$\lim_{r\to\infty} \psi_{\mathbf{k}} = e^{ikz} + f_k(\theta,\phi)\frac{e^{ikr}}{r}, \tag{2.23}$$

where $f_k(\theta,\phi)$ is called the scattering amplitude that should contain all the information about the scattering potential $V(r)$ and e^{ikz} is given by Eq. 2.22. Since the potential $V(r)$ is spherically symmetric, the scattering amplitude f should be independent of ϕ so that $f_k(\theta,\phi) = f_k(\theta)$.

The differential cross section $d\sigma/d\Omega$ for an elastic collision is given by

$$\frac{d\sigma}{d\Omega} = |f_k(\theta)|^2 . \tag{2.24}$$

The total cross section is then

$$\sigma = \int d\Omega \frac{d\sigma}{d\Omega} = 2\pi \int_0^{\pi} |f_k(\theta)|^2 \sin\theta d\theta. \tag{2.25}$$

This cross section are in units of area. The incident flux multiplied by this cross

section gives the total scattering rate.

2.2.2 The partial wave expansion

In order to calculate this scattering amplitude $f_k(\theta)$ for low-energy scattering, we make use of the partial wave expansion. First, we write down the Schrödinger equation with a spherically symmetric potential $V(r)$

$$\left[-\frac{\hbar^2}{2\mu}\nabla^2 + V(r)\right]\psi = E\psi. \tag{2.26}$$

For the central potential problem, we choose spherical coordinates and use the fact that the total relative angular momentum $\mathbf{L}$ is conserved. Hence, Eq. 2.26 can be written as

$$[-\frac{\hbar^2}{2\mu}\frac{1}{r}\frac{\partial^2}{\partial r^2}r + \frac{\mathbf{L}^2}{2\mu r^2} + V(r)]\psi(r,\theta) = E\psi(r,\theta). \tag{2.27}$$

As $V(r)$ is spherically symmetric, we can expand the wave function $\psi(r,\theta)$ in terms of Legendre polynomials

$$\psi(r,\theta,\varphi) = \sum_{l=0}^{\infty} A_l P_l(\cos\theta) R_l(r), \tag{2.28}$$

where $P_l(\cos\theta)$ is the l^{th} Legendre polynomial defined in Eq. 2.21.

Eq. 2.27 then yields

$$\left[\frac{1}{r}\frac{d^2}{dr^2}r + \frac{2\mu}{\hbar^2}(E - V(r)) - \frac{l(l+1)}{r^2}\right] R_l = 0. \tag{2.29}$$

If we let

$$R_l(r) = \chi_l(r)/r, \tag{2.30}$$

Eq. 2.29 yields

$$\chi_l'' + \left[\frac{2\mu}{\hbar^2}(E - V(r)) - \frac{l(l+1)}{r^2}\right]\chi_l = 0. \tag{2.31}$$

Asymptotically far away from the potential $r \to \infty$, $\chi_l(r)$ has the form

$$\chi_l(r) \underset{r\to\infty}{\to} \sin(kr - l\pi/2 + \delta_l(k)). \tag{2.32}$$

Therefore,, the radial wave function $R_l(r)$ has the form

$$R_l(r) \underset{r\to\infty}{\to} \frac{\sin(kr - l\pi/2 + \delta_l(k))}{r}. \tag{2.33}$$

Here δ_l is called the partial wave phase shift, which is caused by the scattering potential. By inserting Eq. 2.33 into Eq. 2.28 and then comparing it to Eq. 2.23, we can express the scattering amplitude $f_k(\theta)$ in terms of this δ_l by virtue of the partial wave expansion

$$\begin{aligned} f_k(\theta) &= \sum_{l=0}^{\infty} P_l(\cos\theta)\frac{2l+1}{2ik}(e^{2i\delta_l} - 1) \\ &= \sum_{l=0}^{\infty}(2l+1)P_l(\cos\theta)f_l(k), \end{aligned} \tag{2.34}$$

where the l^{th} partial wave scattering amplitude $f_l(k) = (e^{2i\delta_l} - 1)/2ik$. If the potential is absent, $\delta_l = 0$ for all l and therefore $f_l = 0$ for all l.

In general, l can take any value between 0 and ∞. However, for the ultra-cold atoms, high l partial wave scattering is suppressed at low temperatures, which

leaves only the lowest s-wave contributing to the scattering process. Atoms in our trap are typically cooled down to around the order of μK, which gives the thermal de Broglie wavelength $\lambda = h/(\sqrt{2\pi m k_B T})$ around 0.7μ m. If we use $hr_0/\lambda = \hbar l_{max}$ to estimate the maximum angular momentum that can possibly contribute to the scattering, we obtain $l_{max} \sim r_0/\lambda$. Note that the effective potential range r_0 is roughly tens of Bohr radii, which leads to $l_{max} \sim 0.001 \ll 1$. As a result, only the s wave $l = 0$ needs to be taken into account. Another way to prove the suppression of the p-wave scattering is to compare the relevant threshold energy for p-wave scattering to the barrier height. The total energy of ultracold atoms consists of the kinetic energy and the interaction energy. With the help of Eq. 2.18, the effective potential includes the centrifugal potential is

$$V_{eff}(r) = \frac{l(l+1)\hbar^2}{2\mu r^2} - \frac{C_6}{r^6}. \tag{2.35}$$

For p-wave scattering, $l = 1$. To estimate the threshold energy, we set $V'_{eff}(r_0) = 0$ to find the location of the peak r_0, yielding

$$r_0 = \sqrt{\frac{3C_6\mu}{\hbar^2}}. \tag{2.36}$$

Inserting Eq. 2.36 back into Eq. 2.35, we obtain the threshold energy for the p-wave scattering as

$$E_{TH} = \psi(r_0) = \frac{2}{3\sqrt{3}} \frac{\hbar^3}{\sqrt{C_6}\mu^{3/2}}. \tag{2.37}$$

In cgs units, $C_6 = \tilde{C}_6 a_0^5 e^2$, where $\tilde{C}_6 = 1390$ for ^{6}Li and the electron charge is $e = 4.8 \times 10^{-10}$ and the Bohr radius is $a_0 = 5.29 \times 10^{-9} cm$. The mass of ^{6}Li is $10^{-23} g$. Using these numbers, we can obtain the $E_{TH} = 1.106 \times 10^{-18} erg$, yielding

a threshold energy $E_{TH} = k_B \times 8\,\mathrm{mK}$. This threshold energy is much higher than the typical energy of our ultracold ^{6}Li atoms, which is of the order of $\mu\mathrm{K}\times k_B$.

If only the s-wave scattering is considering in Eq 2.34, the scattering amplitude can be simplifieds to

$$f_0 = e^{i\delta_0}\frac{\sin\delta_0}{k}. \tag{2.38}$$

Using Eq 2.25, we obtain the total s-wave scattering cross section as

$$\sigma = 4\pi\frac{\sin^2\delta_0}{k^2}. \tag{2.39}$$

Note that for a collision between two atoms with relative momentum $\hbar k$, the total s-wave cross section has a limit of $4\pi/k^2$ when $\sin^2\delta_0 = 1$. This limit is known as the unitary limit and arises when $\delta_0 = \pi/2$ for resonant scattering.

2.2.3 Particle statistics

So far we have assumed that all the colliding particles are distinguishable. To extend our approach to identical particles that are indistinguishable, we need to modify the spatial wave function Eq 2.23 as

$$\lim_{r\to\infty}\psi_{\mathbf{k}}(r) = \frac{e^{ikz}+\gamma e^{-ikz}}{\sqrt{2}} + \left(\frac{f_k(\theta)+\gamma f_k(\pi+\theta)}{\sqrt{2}}\right)\frac{e^{ikr}}{r}. \tag{2.40}$$

Note that this spatial wave function multiplied by the spin wave function gives the total wave function. For two identical particles, the spin wave function is symmetric. Hence, $\gamma = 1$ for bosons to make the symmetric total wave function and $\gamma = -1$ for fermions to make the anti-symmetric total wave function.

The differential cross section for fermions can be written as

$$\frac{d\sigma}{d\Omega} = \frac{|f_k(\theta) - f_k(\pi + \theta)|^2}{2}. \tag{2.41}$$

At low temperature where s-wave scattering dominates, the two amplitudes cancel with each other, which means that two identical fermions cannot interact through s-wave scattering. This is exactly why we need two components of fermion atoms to study their interacting properties at low temperature, as explained before.

2.2.4 S-wave scattering length

At low energy s-wave scattering, it is very useful to define a parameter called the s-wave scattering length as

$$a = \lim_{k \to 0} -\frac{\tan \delta_0(k)}{k}. \tag{2.42}$$

Using this definition, the s-wave scattering amplitude f_0 in Eq 2.38 reduces to

$$f_0 = -\frac{a}{1 + ika}. \tag{2.43}$$

Therefore, the total s-wave cross section can be written as

$$\sigma = \frac{4\pi a^2}{1 + k^2 a^2}. \tag{2.44}$$

For the weakly interacting case when $ka \ll 1$, Eq 2.44 reduces to $\sigma = 4\pi a^2$, which is independent of the energy of the two colliding atoms. For the case when the s-wave scattering length a diverges, the s-wave cross section σ reaches the unitary

limit $\sigma = 4\pi/k^2$, where $\sigma \propto \lambda_T^2$.

2.3 Feshbach resonances

Feshbach resonances are crucial for the study of strongly-interacting Fermi gases, especially for producing unitary Fermi gases and achieving fermionic superfluidity. For ^{6}Li atoms, there exist two Feshbach resonances that can be potentially used to reach unitarity. The Feshbach resonances can be explained using a simple two-channel physical picture.

Two colliding ^{6}Li atoms can interact with one another through either a triplet or a singlet potential. For the triplet potential, two valence electrons form a triplet spin state with the total electron spin $S = s_1 + s_2 = 1$ and z-component projection $m_s = -1, 0, 1$. While for the singlet potential, the two valence electrons form a singlet spin state with the total electron spin $S = s_1 + s_2 = 0$ and z-component projection $m_s = 0$. The singlet and triplet potentials are plotted as for different magnetic fields in Fig 2.3. Note that the singlet potential is much deeper than the triplet one. The reason is that for a singlet potential, the spatial wave function is symmetric due to the anti-symmetric spin wave function. This spatially symmetric wave function allows electrons to sit between the nuclei, resulting in a deep potential. Conversely, the spatial wave function for a triplet potential is anti-symmetric, which prohibits electrons from sitting between the nuclei. This leads to a shallow potential.

For an antisymmetric combination of two lowest hyperfine states $|1\rangle$ and $|2\rangle$, the electron spin state is most triplet at high magnetic field with a magnetic field dependent energy of $-2\mu_B B$ and $m_{s1} + m_{s_2} = -1$. Conversely, the singlet state

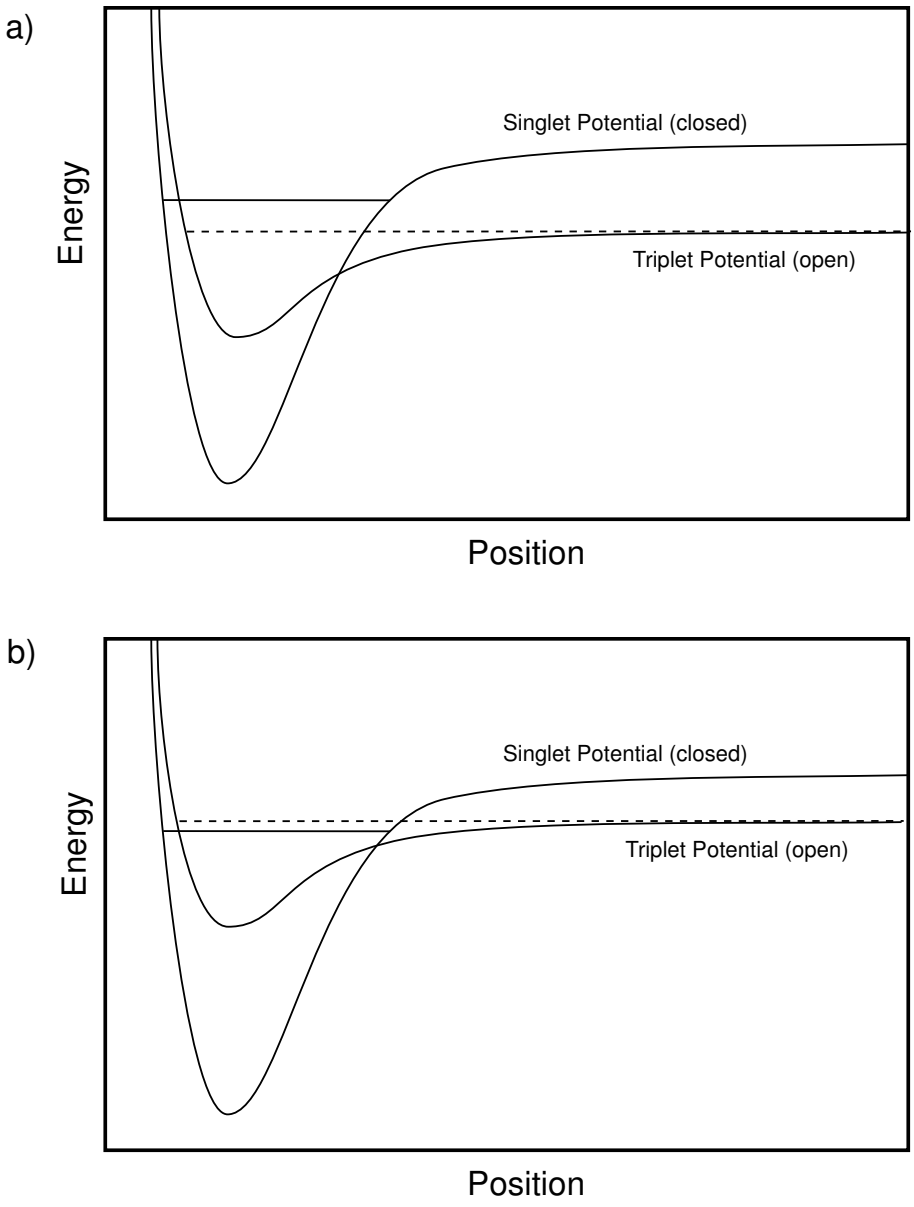

Figure 2.3: Illustration of the singlet and triplet molecular potentials for different magnetic fields. The molecular bound state in the singlet potential is indicated by the horizontal solid line. The dashed line denotes the total energy of two colliding atoms with vanishing kinetic energy with respect to the triplet potential. Through tuning an external magnetic field, the collisional energy in the triplet potential can be tuned below (a) or above (b) the molecular bound state in the singlet potential. The Feshbach resonance occurs when the total collisional energy equals to that of a molecular bound state. This figure is taken from [71].

has a negligible nuclear magnetic moment as g_I is very small and therefore the singlet energy cannot be tuned with the magnetic field to the first order. As the atoms collide at low energy in the triplet potential, the singlet potential is energetically inaccessible. Hence, the triplet is referred to as an open channel and the singlet is referred to as a closed channel. Resonant scattering occurs when an open channel is tuned into a closed channel. This tuning can be realized via an external magnetic field since the magnetic momentum of the open channel $\mu = 2\mu_B$ differs from that of the closed channel $\mu = 0$. If the resonance takes place at magnetic field B_0, the scattering length a_s can be expressed as [84]

$$a_s = a_b \left(1 - \frac{\Delta}{B - B_0}\right) \tag{2.45}$$

where a_b is the background scattering length, Δ is the width of the resonance and B is the magnetic field applied. For a mixture of $|1\rangle$ and $|2\rangle$ ^{6}Li atoms, the broad Feshbach resonance is located at $B_0 = 834.42\,\mathrm{G}$ with a width of $\Delta = 300\,\mathrm{G}$ [84], as is shown in Fig 2.4. The background scattering length is $a_B = -1405\,a_0$, where a_0 is the Bohr radius. At high field, this background scattering length approaches $-2240\,a_0$, which is unusually large. This is due to the fact that the triplet potential, if it were a little deeper, would be in resonance with a bound state. This is why ^{6}Li was considered as an excellent candidate to achieve the fermionic superfluidity before the realization of the Feshbach resonance for ultracold Fermi gases.

The broad Feshbach resonance allows an easy experimental access to the strongly interacting regime. When tuned on resonance, atoms are strongly interacting and the s-wave scattering length diverges. Therefore the cross section

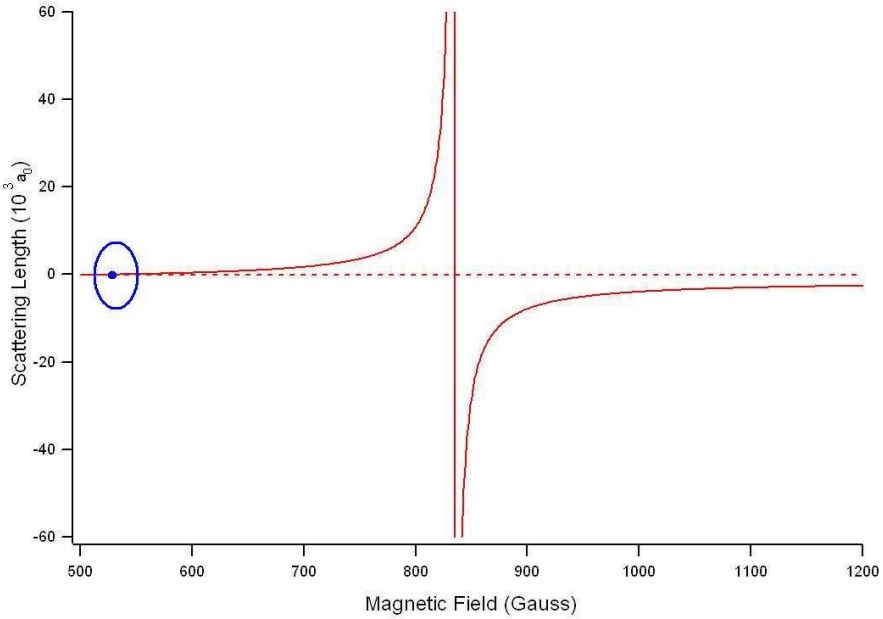

Figure 2.4: The ^{6}Li s-wave scattering length between states $|1\rangle$ and $|2\rangle$ as a function of the magnetic field, generated using the formula from Ref. [84]. The scattering length diverges in the vicinity of the broad Feshbach resonance located around 834.42G. The red dashed line, showing the location of zero scattering length, intersects with the red solid line at 528G indicated by the blue circle, giving rise to a zero-crossing point where the ^{6}Li atoms are non-interacting.

reaches its unitary limit $4\pi/k^2$, where $k = 2\pi/\lambda_T$ is the relative wave number of two colliding atoms. This is the so-called unitary regime, where a rich variety of interesting physics arises.

There also exists a narrow Feshbach at roughly 543G [85], which is not displayed in Fig 2.4. This narrow resonance, as indicted by the name, has a small width of 0.1 G. This narrow Feshbach resonance, found to be energy dependent over the scale of the Fermi energy E_F, can be used to study strongly correlated Fermi gases with a sizable effective range and a large scattering length [95].

As discussed before, the broad and narrow Fehsbach resonances can be reached using a bias magnetic field to tune the open channel resonant with a bound state in a closed channel. However, limited by the coil inductance, this magnetic tuning is not fast enough if one wants to study the non-equilibrium physics for a unitary Fermi gas. A method of optically tuning the open channel into the closed one has been proposed recently [93]. In this method, inelastic loss arising from spontaneous emission is greatly suppressed by destructive quantum interference, making it very promising to control the Feshbach resonance through optical methods and therefore study interesting non-equilibrium physics.

2.4 The unitary regime

As discussed before, the unitary regime is achieved by tuning a bias magnetic field to the board Feshbach resonance located at 834G for ^{6}Li. At unitarity, the atoms are strongly interacting and the s-wave scattering length diverges, making the inter-particle spacing L the only length scale at zero temperature. In this section, we will step by step discuss the properties of unitary Fermi gases. In

Section 2.4.1, we begin by deriving some basic thermodynamic parameters for non-interacting Fermi gases, including the density of states, the Fermi energy and the ground state energy. Section 2.4.2 introduces the local density approximation and then the spatial distribution of the density profile for a harmonically trapped Fermi gas at different temperatures. After that, a universal energy parameter $(1+\beta)$ is introduced in Section 2.4.3, which scales the ground state energy of an ideal Fermi gas to that of a unitary Fermi gas. Finally, the virial theorem is derived in Section 2.4.4. This viiral theorem allows us to rigorously calculate the energy of a trapped Fermi gas based on its cloud dimensions.

2.4.1 Ideal gas thermodynamic quantities

^{6}Li atoms are fermions, which obey the Fermi-Dirac statistics. Considering a large number of atoms with single particle states well occupied, a semi-classical approximation called the local density approximation (LDA) can be applied. The LDA deals with the case when a large number of atoms are confined in a small volume element and the trapping potential $V(\mathbf{r})$ varies slowly within this small volume element. A detailed description that discusses the validity of LDA can be found in [64]. By virtue of the LDA, the Hamiltonian can be written as $H(\mathbf{r},\mathbf{p}) = \mathbf{p}^2/2m + V(\mathbf{r})$ and therefore the Fermi occupation function is

$$f(\mathbf{r},\mathbf{p}) = \frac{1}{\exp\left(\frac{\frac{\mathbf{p}^2}{2m}+V(\mathbf{r})-\mu}{k_B T}\right)+1}, \tag{2.46}$$

where T is the temperature and μ is the chemical potential fixed by the total atom number N as

$$N = \frac{1}{(2\pi\hbar)^3} \int d\mathbf{r}\, d\mathbf{p}\, f(\mathbf{r}, \mathbf{p}). \tag{2.47}$$

Writing the Hamiltonian in terms of the energy ϵ, we obtain

$$N = \int_0^\infty g(\epsilon) f(\epsilon) d\epsilon, \tag{2.48}$$

where the occupation number is

$$f(\epsilon) = \frac{1}{\exp\left(\frac{\epsilon-\mu}{k_B T}\right) + 1}, \tag{2.49}$$

and the parameter $g(\epsilon)$ is the density of states

$$g(\epsilon) = \frac{1}{(2\pi\hbar)^3} \int d\mathbf{r}\, d\mathbf{p}\, \delta(\epsilon - \mathbf{p}^2/2m - V(\mathbf{r})). \tag{2.50}$$

Obviously, this density of states $g(\epsilon)$ depends on the dimensionality of the trapping potential $V(r)$. For a three-dimensional harmonic trapping potential

$$V(\mathbf{r}) = \frac{1}{2} m\omega_x^2 x^2 + \frac{1}{2} m\omega_y^2 y^2 + \frac{1}{2} m\omega_z^2 z^2 \tag{2.51}$$

with its energy levels $\epsilon = \hbar(\omega_x n_x + \omega_y n_y + \omega_z n_z + 3/2)$, the density of states is found to be

$$g(\epsilon) = \frac{\epsilon^2}{2(\hbar\bar{\omega})^3} \tag{2.52}$$

where $\bar{\omega} = (\omega_x \omega_y \omega_z)^{1/3}$ is the geometrical average of the three trapping frequencies.

In terms of the density of states, we can readily calculate the relevant thermodynamic quantities for non-interacting Fermi gases. Inserting Eq 2.52 in Eq 2.48 yields

$$N = \frac{1}{2(\hbar\bar{\omega})^3}\int_0^\infty \frac{\epsilon^2}{\exp(\frac{\epsilon-\mu}{k_BT})+1}d\epsilon. \tag{2.53}$$

This equation can be greatly simplified by considering a zero-temperature Fermi gas, for which the Fermi occupation number becomes unity for energy levels from the ground state up to the Fermi energy E_F and zero for energy levels above E_F. For an equal mixture of two spin states single with total atom number N, Eq 2.53 reads

$$\frac{N}{2} = \frac{1}{2(\hbar\bar{\omega})^3}\int_0^{E_F} \epsilon^2 d\epsilon \tag{2.54}$$

A simply calculation yields the Fermi energy E_F for N atoms equally distributed in two spin states

$$E_F = (3N)^{1/3}\hbar\bar{\omega} \tag{2.55}$$

This Fermi energy is usually referred to as the global Fermi energy for a ground state non-interacting Fermi gas. The Fermi energy for non-interacting Fermi gases is of great importance as it sets the only energy scale for the unitary Fermi gases in a harmonic trap. The corresponding Fermi temperature is naturally defined as

$$T_F = \frac{E_F}{k_B} \tag{2.56}$$

At zero temperature, the global chemical potential defines the Fermi energy so that $\mu_G(T=0) = E_F$.

Having derived the density of states and Fermi energy for a harmonically trapped Fermi gas, we can determine the energy per particle for a harmonically

confined Fermi gas

$$E(T) = \frac{1}{(\hbar\bar{\omega})^3} \int_0^\infty \frac{\epsilon^3}{\exp\left(\frac{\epsilon-\mu}{k_B T}\right) + 1} d\epsilon \tag{2.57}$$

Zero temperature yields the simplest case with $E(T = 0)$ as

$$E(T = 0) = \frac{3}{4} E_F \tag{2.58}$$

As a result, for a non-interacting ground state Fermi gas, the energy per particle E normalized by the Fermi energy E_F is $E_0/E_F = 0.75$.

2.4.2 Density profiles for harmonically trapped Fermi gases

So far, we have derived several global quantities that describe the macroscopic behavior of an atomic cloud confined in a harmonic trap. To extend our discussion to the local quantities, we need to determine the density profile for a harmonically trapped Fermi gas at different temperatures. With the assumption of the local density approximation, by integrating the Fermi occupation function Eq 2.46 over momentum space, we obtain the three dimensional spatial density distribution $n(x, y, z)$

$$n(x, y, z) = \frac{1}{(2\pi\hbar)^3} \int d\mathbf{p} f(\mathbf{r}, \mathbf{p}). \tag{2.59}$$

Inserting Eq. 2.50 into Eq. 2.59 yields

$$n(x, y, z) = \frac{1}{(2\pi\hbar)^3} \int d\epsilon f(\epsilon) \int d\mathbf{p}\, \delta[\epsilon - \mathbf{p}^2/2m - V(x, y, z)]. \tag{2.60}$$

Performing the integral of the δ function over the whole momentum space leads to

$$n(x,y,z) = \frac{m^{3/2}}{\sqrt{2}\pi^2\hbar^3}\int d\epsilon f(\epsilon)[\epsilon - V(x,y,z)]\mathbf{\Theta}[\epsilon - V(x,y,z)] \tag{2.61}$$

where $\mathbf{\Theta}(\epsilon - V(x,y,z))$ is a step function which becomes unity for $\epsilon > V(x,y,z)$ and vanishes otherwise.

The Fermi occupation function $f(\epsilon)$ changes as the temperature T varies. As a result, Eq 2.61 yields different results for different temperature regimes. Here we consider the two simplest limits: zero temperature and high temperature.

For an balanced two-component non-interacting Fermi gas with $N/2$ atoms in a single spin state at zero temperature, the Fermi occupation number is unity for energy levels below the Fermi energy and zero otherwise. Eq 2.52 becomes

$$n(x,y,z) = \frac{\sqrt{2}m^{3/2}}{3\pi^2\hbar^3}E_F^{3/2}\left(1 - \frac{V(x,y,z)}{E_F}\right)^{3/2}\mathbf{\Theta}(\epsilon - V(x,y,z)). \tag{2.62}$$

Note that $n(x,y,z)$ is the number density for a single spin state. If we define the Fermi radii as

$$\begin{aligned}
\sigma_{Fx} &= \left(\frac{2E_F}{m}\right)^{1/2}\frac{1}{\omega_x};\\
\sigma_{Fy} &= \left(\frac{2E_F}{m}\right)^{1/2}\frac{1}{\omega_y};\\
\sigma_{Fz} &= \left(\frac{2E_F}{m}\right)^{1/2}\frac{1}{\omega_z},
\end{aligned} \tag{2.63}$$

the harmonic trapping potential can be written as

$$V(x,y,z) = E_F\left(\frac{x^2}{\sigma_x^2} + \frac{y^2}{\sigma_y^2} + \frac{z^2}{\sigma_z^2}\right). \tag{2.64}$$

Inserting Eq 2.64 into Eq 2.62 yields a zero-temperature Thomas-Fermi density profile for a single spin state

$$n(x,y,z) = \frac{4N}{\pi^2 \sigma_{Fx}\sigma_{Fy}\sigma_{Fz}} \left(1 - \frac{x^2}{\sigma_{Fx}^2} - \frac{y^2}{\sigma_{Fy}^2} - \frac{z^2}{\sigma_{Fz}^2}\right)^{3/2} \mathbf{\Theta}\left(1 - \frac{x^2}{\sigma_{Fx}^2} - \frac{y^2}{\sigma_{Fy}^2} - \frac{z^2}{\sigma_{Fz}^2}\right) \tag{2.65}$$

For the high temperature limit, the Fermi occupation function approaches a Maxwell-Boltzmann distribution $f(\epsilon) = \exp^{-\frac{\epsilon-\mu}{k_B T}}$. Therefore, Eq 2.61 results in a Gaussian distribution in the high temperature limit

$$n(x,y,z) = \frac{N}{2\pi^{3/2}\sigma_x\sigma_y\sigma_z} \exp\left(-\frac{x^2}{\sigma_x^2} - \frac{y^2}{\sigma_y^2} - \frac{z^2}{\sigma_z^2}\right) \tag{2.66}$$

where σ_x, σ_y and σ_z are the Gaussian widths for the three directions.

Both Eq 2.65 and Eq 2.66 are three dimensional density profiles for a single spin state. If we integrate them along one radial direction, we can obtain two-dimensional density distributions, which can be used to fit to the two-dimensional density profile extracted from the experimental images discussed in the next chapter. By assuming that we integrate along the y-axis, Eq 2.65 yields

$$n(x,z) = \frac{3N}{2\pi\sigma_{Fx}\sigma_{Fz}} \left(1 - \frac{x^2}{\sigma_{Fx}^2} - \frac{z^2}{\sigma_{Fz}^2}\right)^{2} \mathbf{\Theta}\left(1 - \frac{x^2}{\sigma_{Fx}^2} - \frac{z^2}{\sigma_{Fz}^2}\right), \tag{2.67}$$

and Eq 2.66 leads to

$$n(x,z) = \frac{N}{2\pi\sigma_x\sigma_z} \exp\left(-\frac{x^2}{\sigma_x^2} - \frac{z^2}{\sigma_z^2}\right) \tag{2.68}$$

2.4.3 Ground state energy of a unitary Fermi gas

Eq 2.65 and Eq 2.66 discussed above are applicable for both an ideal Fermi gas and a unitary Fermi gas. However, the global and local Fermi energies are expected to be different for an ideal Fermi gas and a unitary Fermi gas because interactions should be taken into account for a unitary Fermi gas. In the local density approximation, we have

$$\mu_L(\mathbf{r}) + V(\mathbf{r}) = \mu_G \tag{2.69}$$

where $\mu_L(\mathbf{r})$ and μ_G are the local and global chemical potentials, respectively. $V(\mathbf{r})$ is the harmonic trapping potential, as shown in Eq 2.51. For a zero temperature ideal Fermi gas, we have $\mu_L(\mathbf{r}) = \epsilon_F(\mathbf{r})$ and $\mu_G = E_F$, where $\epsilon_F(\mathbf{r}) = \hbar^2(3\pi^2 n)^{2/3}/2m$ and $E_F = \hbar\bar{\omega}(3N)^{1/3}$ are the local and global Fermi energies for an ideal Fermi gas, respectively, with n is the total number density and N is the total atom number. Hence, Eq 2.69 yields

$$\epsilon_F(\mathbf{r}) + V(\mathbf{r}) = E_F \tag{2.70}$$

The total energy of a unitary Fermi gas includes interaction energy, which is not taken into account for a non-interacting Fermi gas. As a result, the Eq 2.70 is modified to be

$$\epsilon_F(\mathbf{r}) + V(\mathbf{r}) + U_{int}(\mathbf{r}) = \gamma E_F \tag{2.71}$$

where U_{int} is the interaction energy and γ is a scale factor for the global Fermi energy. For a unitary Fermi gas, the local Fermi energy $\epsilon_F(\mathbf{r})$ sets the only energy scale for the local quantities. Hence, the interaction energy must be of the form

as $U_{int}(\mathbf{r}) = \beta\epsilon_F(\mathbf{r})$, where β is a universal energy parameter. By introducing this β, Eq 2.71 yields,

$$\begin{aligned} \epsilon_F(\mathbf{r}) + V(\mathbf{r}) + \beta\epsilon_F(\mathbf{r}) &= \gamma E_F \\ (1+\beta)\epsilon_F(\mathbf{r}) + V(\mathbf{r}) &= \gamma E_F, \end{aligned} \tag{2.72}$$

which shows that we need to rescale the local Fermi energy by a factor of $1+\beta$ if we want to map a non-interacting Fermi gas to a unitary Fermi gas. Note that the global Fermi energy also needs to be rescaled by a factor of γ, which arises from the interaction energy. In a fixed harmonic potential, the local Fermi energy $\epsilon_F \propto 1/m$ and the global Fermi energy $E_F \propto \sqrt{1/m}$. If we rescale the local Fermi energy ϵ_F by a factor of $1+\beta$ for the added interaction energy, we are essentially rescaling the mass m to an effective mass m^* as $m^* = m/(1+\beta)$. Hence, the global Fermi energy needs to be rescaled by a factor of $\sqrt{1+\beta}$ for the same reason. Hence, $\gamma = \sqrt{1+\beta}$ and Eq 2.72 reduces to

$$(1+\beta)\epsilon_F(\mathbf{r}) + V(\mathbf{r}) = \sqrt{1+\beta}E_F \tag{2.73}$$

To summarize, Eq 2.69 holds for both non-interacting Fermi gas and unitary Fermi gas. For a zero temperature ideal Fermi gas, $\mu_L(\mathbf{r}) = \epsilon_F(\mathbf{r})$ and $\mu_G = E_F$, while for a zero temperature unitary Fermi gas, $\mu_L(\mathbf{r}) = (1+\beta)\epsilon_F(\mathbf{r})$ and $\mu_G = \sqrt{1+\beta}E_F$. $\epsilon_F(\mathbf{r}) = (\hbar^2(3\pi^2 n)^{2/3})/(2m)$ is the local Fermi energy for an ideal Fermi gas and $E_F = \hbar\bar{\omega}(3N)^{1/3}$ is the global Fermi energy for an ideal Fermi gas.

The universal parameter β was first proposed in nuclear physics in 1999 and introduced to the unitary Fermi gas in 2002. Since then, β has been measured in a variety of experiments: $\beta = -0.56$ [50], $\beta = 0.54$ [82], $\beta = 0.62$ [32] and

most recently $\beta = 0.62$ [83], which are all in reasonably good agreement with the Monte Carlo simulations $\beta = 0.58$ [59, 74, 75] and $\beta = 0.56$ [86].

2.4.4 Virial Theorem

As one of the most important thermodynamic quantities, energy needs to be accurately determined before we study thermodynamic properties of a unitary Fermi gas. For a trapped unitary Fermi gas, the totally energy has three components: the kinetic energy, the interaction energy and the trapping potential. It is very useful to find a simple method to determine the energy for a trapped unitary Fermi gas by using only one or two experimentally measurable parameters.

In order to determine the energy, we exploit the virial theorem [42], which we prove is true for a unitary fermi gas, despite strong interactions. Let's first consider a small volume ΔV centered at position $\mathbf{r}$ containing ΔN atoms. According to the universal hypothesis [27], for a unitary Fermi gas, all the local thermodynamic quantities depend only on the local density n and temperature T. As a result, the local energy ΔE has to be of the general form

$$\Delta E = \Delta N \epsilon_F f_E \left(\frac{T}{T_F(n)} \right), \tag{2.74}$$

where $\epsilon_F = \hbar^2 (3\pi^2 n)^{2/3}/2m$ is the local Fermi energy and $T_F = \epsilon_F / k_B$ is the corresponding local Fermi temperature. The universal function f_E depends only on the local reduced temperature $T/T_F(n)$, which is the local temperature T normalized by the local Fermi temperature $T_F(n)$. f_E becomes $3/5$ for a zero-temperature non-interacting Fermi gas, while f_E is $3(1+\beta)/5$ for a zero-temperature unitary Fermi gas, where β is the aforementioned universal energy parameter. For an

ideal Fermi gas, we expect $E = 3k_BT/2$, yielding $f_E = (3T)/(2T_F(n))$.

To obtain the local pressure, we use the relation

$$P = -\left(\frac{\partial \Delta E}{\partial \Delta V}\right)_{\Delta N, \Delta S}. \tag{2.75}$$

Note that we need to hold the local reduced temperature $T/T_F(n)$ constant to perform this calculation. As a result, Eq 2.75 leads to

$$\begin{aligned} P &= -\Delta N f_E \frac{\partial \epsilon_F}{\partial \Delta V} \\ &= -\Delta N f_E \frac{\hbar^2 (3\pi^2)^{2/3}}{2m} \frac{\partial n^{2/3}}{\partial \Delta V} \\ &= \frac{2}{3} \Delta N f_E \frac{\hbar^2 (3\pi^2 n)^{2/3}}{2m} \frac{1}{\Delta V} \\ &= \frac{2}{3} n \epsilon_F f_E. \end{aligned} \tag{2.76}$$

Using the total energy density $\mathcal{E}(n,T) = n\epsilon_F f_E$, Eq. 2.76 yields a very important relation between the pressure and energy density

$$P = \frac{2}{3}\mathcal{E}(n,T). \tag{2.77}$$

Note that Eq 2.77 holds for both non-interacting and unitary Fermi gases.

Now let's consider an atomic cloud confined in a trap. Force balance requires that the pressure P equals to the force arising from the trapping potential at any position $\mathbf{r}$

$$\boldsymbol{\nabla} P(\mathbf{r}) + n(\mathbf{r}) \boldsymbol{\nabla} V(r) = 0 \tag{2.78}$$

If we take an inner product $\mathbf{r} \cdot \boldsymbol{\nabla} P(\mathbf{r})$ and $n(\mathbf{r})\, \mathbf{r} \cdot \boldsymbol{\nabla} V(r)$ and then integrate over

the volume of the cloud, Eq 2.78 yields

$$\int d\mathbf{r}\, \mathbf{r} \cdot \boldsymbol{\nabla} P(\mathbf{r}) + \int d\mathbf{r}\, n(\mathbf{r})\, \mathbf{r} \cdot \boldsymbol{\nabla} V(r) = 0 \tag{2.79}$$

Consider the first integral on the left side

$$\int d\mathbf{r}\mathbf{r} \cdot \boldsymbol{\nabla} P(\mathbf{r}) = \int d\mathbf{r} \boldsymbol{\nabla} \cdot (\mathbf{r} P(\mathbf{r})) - \int d\mathbf{r} P(\mathbf{r}) \boldsymbol{\nabla} \cdot \mathbf{r} \tag{2.80}$$

The first term vanishes as the local density approaches zero as the surface of the cloud. Hence,

$$\begin{aligned} \int \mathbf{r} \cdot \boldsymbol{\nabla} P(\mathbf{r}) &= -\int d\mathbf{r} P(\mathbf{r}) \boldsymbol{\nabla} \cdot \mathbf{r} \\ &= -3 \int d\mathbf{r} P(\mathbf{r}) \end{aligned} \tag{2.81}$$

Using Eq 2.81 in Eq 2.79, we obtain

$$\begin{aligned} -3 \int d\mathbf{r} P(\mathbf{r}) + \int d\mathbf{r}\, n(\mathbf{r})\, \mathbf{r} \cdot \boldsymbol{\nabla} V(r) &= 0 \\ -2 \int d\mathbf{r} \mathcal{E}(\mathbf{r}) + \int d\mathbf{r}\, n(\mathbf{r})\, \mathbf{r} \cdot \boldsymbol{\nabla} V(\mathbf{r}) &= 0 \end{aligned} \tag{2.82}$$

where we use the universal relation $P = 2\mathcal{E}/3$, as derived above. Since the total energy of a unitary Fermi gas consists of its internal energy (kinetic and interaction) and the trapping potential, we have $\int d\mathbf{r} \mathcal{E}(\mathbf{r}) + N\langle V \rangle = NE$ and Eq 2.82 leads to

$$\begin{aligned} 2NE - 2N\langle V \rangle - N\langle \mathbf{r} \cdot V(\mathbf{r}) \rangle &= 0 \\ \langle V \rangle + \frac{1}{2} \langle \mathbf{r} \cdot V(\mathbf{r}) \rangle &= E \end{aligned} \tag{2.83}$$

where E is the total energy per particle and $\langle V \rangle$ is the average potential energy per particle. This general and important result gives the total energy for any trap potential.

Eq 2.83 is the general form for the virial theorem for an arbitrary trapping potential. For the aforementioned harmonic potential Eq 2.51, $\langle \mathbf{r} \cdot V(\mathbf{r}) \rangle = 2\langle V \rangle$ and therefore Eq 2.83 yields

$$E = 2\langle V \rangle \tag{2.84}$$

Note that the pressure in all three directions equals to each other and the trapping potential are the same in all three directions $\langle V_x \rangle = \langle V_y \rangle = \langle V_z \rangle$. Hence, Eq 2.84 has a more experimentally accessible form as

$$\begin{aligned} E &= 2\langle V \rangle \\ &= 2(\frac{1}{2}m\omega_x^2 x^2 + \frac{1}{2}m\omega_y^2 y^2 + \frac{1}{2}m\omega_z^2 z^2) \\ &= 3m\omega_z^2 z^2 \end{aligned} \tag{2.85}$$

This theorem provides us with a very powerful method to measure the initial energy of a harmonically trapped cloud by measuring the mean square size of the cloud density profile and the trap frequencies. Although this result is derived by assuming a specific harmonic trap case, it can be generalized for any trapping potential without assuming either the local density approximation or harmonic confinement, using the Hellman-Feynman theorem [90].

Realistically, the trap we deal with in our lab is Gaussian,which is not perfectly harmonic. As a result, an anharmonic correction needs to be included in the virial

theorem Eq 2.85. Let's start with the Gaussian trap

$$V = V_0 \left[1 - \exp\left(-\frac{m\bar{\omega}^2\bar{r}^2}{2V_0}\right)\right] \tag{2.86}$$

where we denote $\bar{r}^2 = \omega_x^2 x^2/\bar{\omega}^2 + \omega_y^2 y^2/\bar{\omega}^2 + \omega_z^2 z^2/\bar{\omega}^2$ and $\bar{\omega} = (\omega_x\omega_y\omega_z)^{1/3}$. To get the anharmonicity correction term, we need to Taylor expand this Gaussian potential up to the second order, yielding

$$\begin{aligned} V &= V_0 \left[1 - \exp\left(-\frac{m\bar{\omega}^2\bar{r}^2}{2V_0}\right)\right] \\ &= \frac{m\bar{\omega}^2\bar{r}^2}{2} - \frac{V_0}{2}\left(\frac{m\bar{\omega}^2\bar{r}^2}{2V_0}\right) \\ &= \frac{m\bar{\omega}^2\bar{r}^2}{2} - \frac{V_0}{2}\left(\frac{m\bar{\omega}^2\bar{r}^2}{2V_0}\right) \\ &= \frac{m\bar{\omega}^2\bar{r}^2}{2} - \frac{m^2\bar{\omega}^4\bar{r}^4}{8V_0} \end{aligned} \tag{2.87}$$

Note that the second term on the right side is the anharmonicity correction term, which is the first order correction to the harmonic trap approximation.

Eq. 2.83 yields

$$E = \int nV d^3\bar{\mathbf{r}} + \int \frac{1}{2} n\bar{r} \cdot \nabla V d^3\bar{\mathbf{r}} \tag{2.88}$$

Using Eq. 2.87 in Eq. 2.88, the first integral on the right side of Eq. 2.88 leads to

$$\begin{aligned} \int nV d^3\bar{\mathbf{r}} &= \int n\left(\frac{m\bar{\omega}^2\bar{r}^2}{2} - \frac{m^2\bar{\omega}^4\bar{r}^4}{8V_0}\right) d^3\bar{\mathbf{r}} \\ &= \frac{m\bar{\omega}^2}{2}\langle\bar{r}^2\rangle - \frac{m^2\bar{\omega}^4}{8V_0}\langle\bar{r}^4\rangle \\ &= \frac{m\bar{\omega}^2}{2}\langle\bar{r}^2\rangle\left(1 - \frac{m\bar{\omega}^2\langle\bar{r}^2\rangle}{4V_0}\frac{\langle\bar{r}^4\rangle}{\langle\bar{r}^2\rangle^2}\right) \end{aligned} \tag{2.89}$$

Evaluating the second integral on the right side of Eq. 2.88 yields

$$\int \frac{1}{2} n\bar{r} \cdot \nabla V d^3\bar{\mathbf{r}} = \frac{m\bar{\omega}^2}{2}\langle \bar{r}^2 \rangle \left(1 - \frac{m\bar{\omega}^2\langle \bar{r}^2 \rangle}{2V_0}\frac{\langle \bar{r}^4 \rangle}{\langle \bar{r}^2 \rangle^2}\right) \tag{2.90}$$

Adding Eq. 2.89 and Eq. 2.90, we obtain

$$E = \frac{m\bar{\omega}^2}{2}\langle \bar{r}^2 \rangle \left(1 - \frac{3m\bar{\omega}^2\langle \bar{r}^2 \rangle}{4V_0}\frac{\langle \bar{r}^4 \rangle}{\langle \bar{r}^2 \rangle^2}\right) \tag{2.91}$$

For a symmetric Gaussian trap, $\langle \bar{x}^2 \rangle = \langle \bar{y}^2 \rangle = \langle \bar{z}^2 \rangle = \langle \bar{r}^2 \rangle/3$ and $\langle \bar{r}^4 \rangle/\langle \bar{r}^2 \rangle^2 = 5/3$. Therefore, Eq. 2.91 reads as

$$E = 3m\omega_z^2\langle z^2 \rangle \left(1 - \frac{15}{8}\frac{m\omega_z^2\langle z^2 \rangle}{V_0}\right) \tag{2.92}$$

Eq. 2.92 allows us to calculate the total energy per particle of the atoms confined in an nearly harmonic trap with a small anharmonicity.

The virial theorem derived in this section holds for unitarity. When tuned off resonance, the scattering length finite a provides another length scale. Therefore virial theorem is of a more general form [91], which for a harmonic trap is given by

$$E = 2\langle V \rangle - \frac{a}{2}\frac{\partial E}{\partial a} \tag{2.93}$$

Chapter 3

Experimental Procedures

To measure quantum shear viscosity for a unitary Fermi gas, we need to prepare a Fermi gas near a Feshbach resonance. Section 3.1 covers the the general procedures of making and probing a unitary ^{6}Li Fermi gas by following a few well-developed cooling and trapping stages. This section focuses on the basic physics of these stages. The experimental setup that is used to realize each stage will be briefly discussed in Section 3.2. After making a unitary Fermi gas, we conduct two hydrodynamic experiments aimed to measure quantum viscosity for a unitary Fermi gas at different temperature regimes: anisotropic expansion for high temperatures and a radial breathing mode for low temperatures. Section 3.3 reports the details of these two experiments, which will be used to extract viscosity in the following chapters.

3.1 Procedures for making and probing a unitary Fermi gas

To generate an atomic beam, ^{6}Li is heated to $\simeq 700\,\mathrm{K}$. Then the atomic beam passes through a Zeeman-slower, where atoms are slowed by a red-detuned laser beam using the Doppler cooling as discussed in Section 3.1.1. After reducing the

speed to roughly tens of meters per second, atoms are captured by a magneto-optical trap (MOT) formed by three sets of counter-propagating laser beams and two magnetic coils in an anti-Helmholtz configuration. The basic physics of a one dimensional MOT is studied in Section 3.1.2, which can be readily generalized to the three dimensional case. Limited by the Doppler-cooling mechanism, atoms are cooled down to $\simeq 140\mu$K in the MOT, which is not cold enough to reach quantum degeneracy. Section 3.1.3 introduces a dipole optical trap formed by a focused CO_2 laser beam, where atoms are trapped through a quasi-electrostatic dipole force. A broad-band radio frequency field is then applied through radio frequency antenna to ensure an equal mixture of the two lowest hyperfine states, as discussed in Section 3.1.4. The intensity of the CO_2 laser is then lowered to perform evaporative cooling through which atoms in the tail of the Boltzmann distribution escape, leaving atoms colder in trap after thermalization. A collisonal Feshbach resonance is reached by tuning bias magnetic field to 834 G for ^{6}Li to maximize the cooling and re-thermalization process. The mechanism of the evaporative cooling is discussed in details in Section 3.1.5. Section 3.1.6 summarizes the general experimental sequence of making a unitary Fermi gas as well as a weakly interacting Fermi gas, which share the same procedures except for the magnetic field where the force evaporation is conducted. After making a unitary Fermi gas, we switch off the CO_2 trap and probe the atoms using destructive absorption images. This imaging technique is covered in Section 3.1.7. Towards the end of this section, Section 3.1.8 discusses the parametric resonance experiment, which is used to calibrate the trapping frequencies of the optical dipole trap.

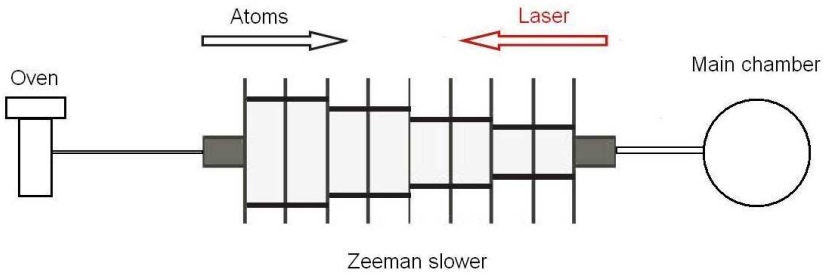

Figure 3.1: A Zeeman slower is connected to an oven where atoms get vaporized. The Zeeman slower consists of a few separate coil site through which constant current flows to ensure that atoms (black arrow) will substantially absorb photons from a counter-propagating red-detuned laser beam (red arrow). Closer the site to the oven, more coils it has. After slowed down to proper velocity, atoms are sent to an ultra high vacuum chamber, where further cooling and trapping processes are performed.

3.1.1 Zeeman slower

At room temperature, ^{6}Li is a soft, shiny metal that can be easily cut into pieces. The melting point for ^{6}Li is roughly 450K. In order to make a unitary ^{6}Li gas, we heat the ^{6}Li metal up to 700 K to generate an atomic beam. After heated up to 700 K, ^{6}Li atoms are traveling at 1300 m/s, which is too fast to be captured by the magneto-optical trap (MOT) that favors a capture velocity ~ 50 m/s. As a result, we utilize a Zeeman slower to slow down the atoms before they enter the MOT. The schematics of a Zeeman slower is shown in Fig. 3.1. If we use a resonant counter-propagating laser beam to hit an atom with an ideal two level energy structure, the atom jumps from the ground state to the excited state by absorbing a photon and then receives a momentum kick $\Delta p = \hbar\, k$, where $k = 2\pi/\lambda$ is the wave number of the laser beam. This momentum kick gives the atom a velocity change $\Delta v = \hbar\, k/m \sim 0.1$ m/s. In order to slow the atom with velocity

$\sim 1300\,\mathrm{m/s}$ down to $\sim 50\,\mathrm{m/s}$, the atom needs to absorb $\sim 1.3 \times 10^4$ photons. The atom can fall back to the ground state through the spontaneous emission. Since the randomness of the direction of the emitted photon, the average effect on the atom over a large number of absorptions and emissions is deceleration.

However, as the atom slows down, it sees a different laser frequency due to the Doppler shift. For the case when the laser beam is moving towards the atom, the Doppler shift can be written as

$$\Delta\nu = \frac{v_{atom}}{c}\nu_0, \tag{3.1}$$

where ν_0 is the laser frequency perceived by an atom at rest and v_{atom} is the speed of the atom and c is the speed of light. Eq. 3.1 yields an upward Doppler shift, which shows that the atom perceives a larger frequency for the counter-propagating laser beam. Therefore, the laser frequency needs to be red-detuned in order to be resonant with the atom. Since this Doppler shift is also velocity dependent, the laser beam, initially resonant with the atom, will no longer be in resonance as the atom slows down. Hence, to continuously slow down the atom, the laser frequency needs to be adjusted accordingly to prevent the laser beam from falling out of resonance with the atom. Practically, it is much easier to Zeeman-tune the energy level of the atom than to adjust the frequency of the laser beam. A spatially varying Zeeman filed is employed to ensure the laser beams remain resonant as the atom slows down. As shown in Fig. 3.1, a Zeeman slower consists of several coil sites, which have progressively fewer coils with respect to the oven. This construction yields larger magnetic field near the oven for larger Doppler shift because atoms travel fast near the oven. Constant current

flows through all the coil sites except the last one to generate a spatially varying magnetic field by construction. This spatially varying magnetic field causes a velocity dependent Zeeman split, which compensates the decrease of the Doppler shift as the atoms slow down. This is referred to as the Doppler cooling. The last coil site uses a reversed current to end the acceleration.

Using the Doppler cooling, the atoms always remain resonant with the laser beam, resulting in a continuous deceleration due to the radiation pressure. We can roughly estimate the acceleration of an ^{6}Li atom shined by a single laser beam. The force can be approximated as $F = R(h/\lambda)$, where $R \simeq 1/(2\tau_{spont})$ is the optical rate. For ^{6}Li atoms, τ_{spont} is 27ns and therefore $R \simeq 2 \times 10^7/s$. Hence, the acceleration a is $2 \times 10^6 m/s^2$ [87]. Therefore, by providing these coils with a certain amount of current, we are able to slow the atoms from 1300 m/s down to approximately 50 m/s.

3.1.2 Magneto-Optical Trap

After being slowed down to roughly 50 m/s, the atoms are able to be captured by a magneto-optical trap (MOT). The MOT is formed by three sets of counter-propagating laser beams with the same frequencies and two magnetic coils in an anti-Helmholtz configuration. The physics of MOT can be decomposed into two parts: an optical part and a magnetic part.

The optical part of a MOT produces a velocity dependent force that damps the motion of the atoms, which can be understood through the picture of optical molasses. Without losing generality, the three dimensional optical beams can be reduced to a one-dimensional representation for simplification, because all the three directions are identical. The basic physics of the one-dimensional MOT is

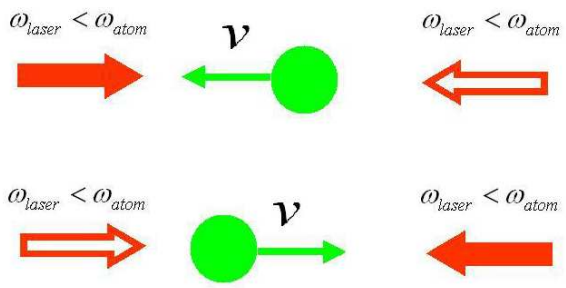

Figure 3.2: One dimensional schematic representation of optical molasses. An green solid circle represents an atom with its velocity denoted as a green solid arrow. The red arrows (solid an hollow) stand for red-detuned laser beams. The upper one: the atom moving to the left becomes closer in resonance with the red-detuned laser beam propagating to the right(solid red arrow), resulting in a preferential net force pointing opposite to the motion of the atom. The lower one: the atom moving to the right becomes closer in resonance with the red-detuned laser beam propagating to the left(solid red arrow), resulting in a preferential net force also pointing opposite to the motion of the atom.

the similar to that of the Zeeman slower, both of which are based on the Doppler cooling. However, for the one-dimensional MOT, instead of one laser beam, we use a pair of counter-propagating red-detuned laser beams, as shown in Fig. 3.2. If the atom is moving to the left direction, it will absorb more photons moving to the right as it sees the right-propagating laser beam closer to resonance due to the Doppler shift. If the atom is traveling to the right, it will absorb more photons moving to the left as it sees the left propagating laser beam closer to resonance. Hence, the atom will be slowed down by preferentially interacting with the red-detuned laser beam that are opposite to their motions. This explanation can be generalized to the three-dimensional case and therefore atoms will be continuously slowed down in all the three directions.

Essentially, Doppler cooling is a random walk in the momentum space, which introduces a heating rate due to the recoil energy. The balance of the cooling rate and heating rate gives rise to the Doppler limit, which determines how cold atoms can become. The Doppler limit temperature is given by

$$k_B T_{Doppler} = \frac{\hbar \gamma_s}{2}, \tag{3.2}$$

where the natural linewidth γ_s is $2\pi \times 5.9\,\mathrm{MHz}$ for ^{6}Li atoms. Therefore, $T_{Doppler} = 140\,\mu\mathrm{K}$. In practice, we do not usually go as low as the Doppler limit in MOT in order to have an optimal loading into the optical dipole trap.

While the optical part of the MOT provides the cooling in the velocity space, atoms are not confined in the spatial coordinates, which may cause a big unwanted loss from the trap. The magnetic part establishes a spatial confinement that are necessary for us to physically trap the atoms in a certain volume. The physics of

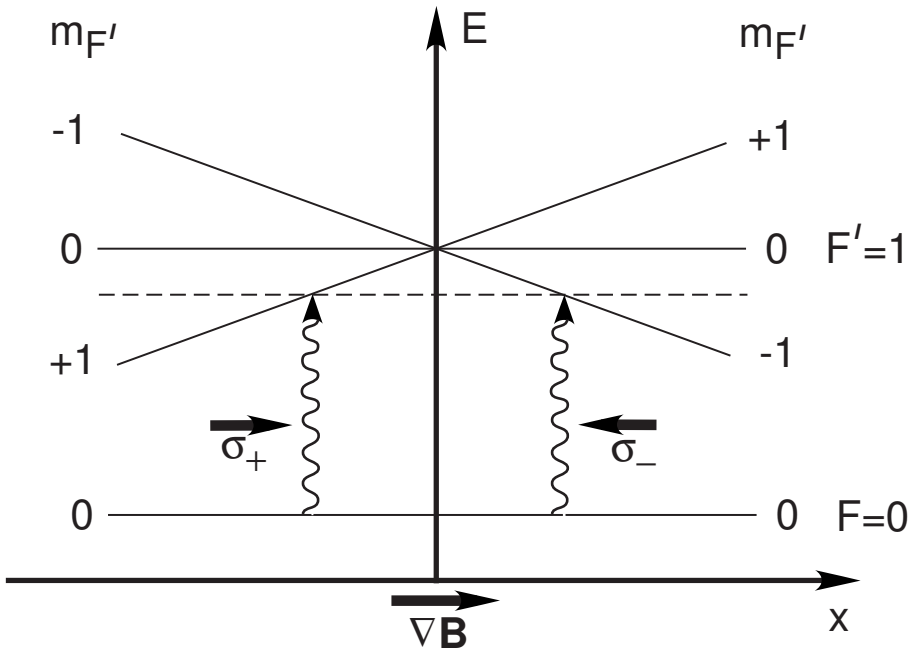

Figure 3.3: One dimensional schematic representation of the Zeeman splitting of a hypothetical two-level system due to an external magnetic field gradient [71], which can be approximated linear in space. The total angular momentum in the ground and first excited states is $F = 0$ and $F' = 1$. The vertical axis denotes the energy while the horizontal axis represents the position. The spatial restoring force arises from the preferential absorption of a photon with a particular polarization based on the atom's position. If an atom is positioned at $x > 0$, it is more likely to absorb a σ_- photon as this transition is Zeeman shifted toward resonance, resulting in a spatially restoring force pointing at origin. Conversely, an atom located at $x < 0$ can preferentially absorb a σ_+ photon, giving rise to a resorting force also pointing at origin.

this spatial confinement can be understood using the following simple picture in one dimension. For an ideal two level atom system, the total angular momentum are $F = 0$ and $F^{'} = 1$ for the ground state and first excited state, respectively. The angular momentum projection in the z direction for the ground state is $m_F = 0$ and for the excited state are $m_{F'} = -1, 0, 1$. In the presence of a magnetic field created by two magnetic coils in an anti-Helmholtz configuration, the Zeeman shift is shown as in Fig. 3.3. The two counter-propagating laser beams are set to be σ_+ and σ_-, respectively. If atoms are sitting on the right side of origin, they will preferentially interact with the σ_- beam that propagates opposite to the atoms due to the Zeeman split in that area. This causes a restoring force which brings atoms back to the origin. If atoms are positioned on the left side of origin, they will preferentially interact with the σ_+ beam that propagates opposite to the atoms, yielding a restoring force pointing to the origin as well. As a result, by applying some proper magnetic field, due to the Zeeman split, a spatially restoring force can be created. Using a combination of optical molasses and proper magnetic field, a large number of cold atoms can be trapped in a magneto-optical trap.

The previous discussion gives quite a simple theoretical explanation of the MOT, which is based on the model of ideal two level atoms. However, as discussed before, the ^{6}Li atoms have more complicated hyperfine structure than an ideal two level system. The ground state of ^{6}Li has $F = 1/2$ and $F = 3/2$ levels, which are split by 228 MHz. Atoms in the excited state can fall into either hyperfine state by emitting a photon. Hence, we need an extra beam to pump the atoms that fall to the wrong hyperfine state back to the right one. This is accomplished by using a repump beam that co-propagates with the MOT beam.

3.1.3 Far-Off-Resonance Trap

The MOT traps millions of atoms with temperature limited by the Doppler limit $T_{Doppler} = 140\mu K$ for ^{6}Li. This is not cold enough to reach quantum degeneracy, which requires the phase-space density $n\lambda_T^3 \sim 1$. Therefore, we need to use new cooling methods to bring atoms down to even lower temperature to realize quantum degeneracy, where rich physics appears.

Since the magneto-optical trap is limited by the Doppler cooling limit, new cooling methods should not use the same cooling mechanism as that of the Doppler cooling, which is based on the momentum exchange between atoms and laser field. An effective way to achieve this goal is the use of a Far-Off-Resonance-Trap (FORT). This type of trap depends on the electric dipole force arising from the interaction between atoms and an oscillating electric field. This electric field can be provided by an ultra-stable CO_2 laser operated at high power $\simeq 100\,\mathrm{W}$. The wavelength of the CO_2 laser is $10.6\,\mu\mathrm{m}$, which is far from the atomic transition frequency. The heating rate due to the Larmor scattering is negligibly small since the scattering rate scales as $1/\lambda^3$ and heating rate as $1/\lambda^5$ [77]. For our CO_2 trap, the optical scattering rate is 2 photons/hour per atom and the heating rate is 18pK/second.

Physically, the CO_2 laser generates an oscillating electric field. If we position an atom in it, a dipole moment is induced, depending on the polarizability of the atom α_d. The interaction potential between the atom and the electric field is

$$U_{dipole} = -\frac{1}{2}\overline{\mathbf{d}\cdot\mathbf{E}}, \tag{3.3}$$

where $d = \alpha_d E$ is the induced dipole moment and E is the electric field created

by the CO_2 trap. Note that the factor of 1/2 is due to the fact that the dipole moment is induced rather than permanent. If the amplitude of the slowly varying electric field is $\mathcal{E}$, the time-averaged interaction potential in SI units is

$$U_{dipole} = -\frac{1}{4}\alpha_d \mathcal{E}^2 = -\frac{1}{2\epsilon_0 c}\alpha_d I, \tag{3.4}$$

where ϵ_0 is the permittivity of free space, c is the speed of light and I is the laser intensity. Depending on the sign of the polarizability α_d, this potential can be either attractive (positive α_d) or repulsive (negative α_d).

The polarizability of the atom α can be understood using a simply model of an electron harmonically bound to the nucleus. The equation of motion for an harmonically electron bound in an optical field is

$$\ddot{\mathbf{x}} + {\omega_0}^2 \mathbf{x} = \frac{-eE}{m_e}, \tag{3.5}$$

where $-e$ is the electron charge, ω_0 is the natural oscillation frequency and m_e is the electron mass. If $\alpha_d E = d = -e\mathbf{x}$, one obtains

$$\alpha_d = \frac{e^2}{m_e}\frac{1}{\omega_0^2 - \omega^2}. \tag{3.6}$$

If we use the dipole matrix element $\mu \equiv e l_0$ with $l_0 = \sqrt{\hbar/2m_e\omega_0}$ the intrinsic length scale for a quantized harmonic oscillator, Eq. 3.6 can be written as

$$\alpha_d = \frac{2\omega_0 \mu^2}{\hbar}\left(\frac{1}{\omega_0^2 - \omega^2}\right), \tag{3.7}$$

Note that in Eq. 3.7, the sign of $\omega_0^2 - \omega^2$ determines the sign of the polarizability

α_d. If the laser field is blue-detuned from the resonance, $\omega > \omega_0$, the electric field is out of phase with the induced dipole and the atoms are repelled from the highest intensity of the trap. If the laser field is red-detuned form the resonance, which is the case for our CO_2 trap, $\omega < \omega_0$ and the electric field is in phase with the induced dipole and the atoms are attracted to the highest intensity of the trap.

For a positive α, as is discussed, the atoms are trapped at the highest intensity region, which is the center of the CO_2 trap. The intensity profile of a focused Gaussian leaser beam can be written as

$$I(r, z, \phi) = \frac{I_0}{1 + (z/z_0)^2} \exp\left(-\frac{2r^2}{w^2}\right), \tag{3.8}$$

where I_0 is the peak intensity at the trap center, w is the $1/e^2$ intensity radius and $z_0 = \pi w^2/\lambda$ is the Rayleigh length. For the CO_2 beam we use, $I_0 \simeq 2\,\mathrm{MW/cm^2}$ and $\lambda = 10.6\,\mu m$ and waist radius $w \simeq 50\,\mu m$, which gives Rayleigh length $z_0 \simeq 0.75\,\mathrm{mm}$.

Thus, the trapping potential is

$$U(r, z, \phi) = -\frac{U_0}{1 + (z/z_0)^2} \exp\left(-\frac{2r^2}{w^2}\right), \tag{3.9}$$

where $U_0 = \alpha\, I_0/(2\epsilon_0 c)$ is the full depth of our optical trap.

By Taylor expanding the potential Eq. 3.9 about the trap center, on obtains

$$U\,(r, z) \simeq -U_0 + \frac{U_0}{z_0^2} z^2 + 2\frac{U_0}{w_0^2} r^2. \tag{3.10}$$

The standard harmonic trap potential with mass m and frequencies ω_i $(i = x, y, z)$

is

$$U(r,z) = \frac{1}{2}m\omega_z^2 z^2 + \frac{1}{2}m\omega_x^2 x^2 + \frac{1}{2}\omega_y^2 y^2 = \frac{1}{2}m\omega_z^2 z^2 + \frac{1}{2}m\omega_r^2 r^2 \tag{3.11}$$

Comparing Eq. 3.10 and Eq. 3.11 yields,

$$\omega_r = \sqrt{\frac{4U_0}{mw_0^2}} \tag{3.12}$$

$$\omega_z = \sqrt{\frac{2U_0}{mz_0^2}}. \tag{3.13}$$

Note that z-direction is the longitudinal direction along which the CO_2 beam propagates, which is also referred to as the axial direction. The x and y directions are the two transverse directions, which are usually referred to as the two radial directions.

The frequencies in the two radial directions are very close to each other $\omega_x \simeq \omega_y$ for the CO_2 trap we normally use and $\omega_r \simeq \sqrt{\omega_x \omega_y}$. As pointed out before, the Rayleigh length is much bigger than the waist radius, so the radial trapping frequency ω_r is much bigger than ω_z, resulting in a much tighter confinement in the radial direction than the axial direction. This has a great physical impact on the initial shape of the atomic cloud and the expansion dynamics of the cloud after release form the trap. This will be discussed in detail later.

The full depth of our CO_2 trap can be estimated using

$$U_0 = \frac{4\alpha_s P_0}{c\nu_x\nu_y}, \tag{3.14}$$

where $\alpha_s = 24.3 \times 10^{-30}\mathrm{m}^3$ [78] is the static polarizability of ^{6}Li atoms, P_0 is the power that can be read from the power meter and $c = 3 \times 10^8\mathrm{m}$. ν_x and

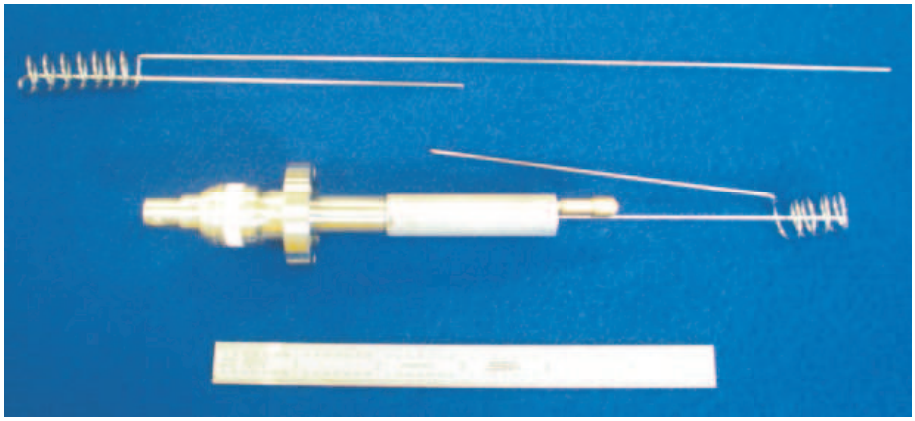

Figure 3.4: Radio frequency antenna installed on a radio frequency power feed-through. The topic is the radio frequency antenna made from the stainless steel. The middle is the antenna installed on a power feed-through. The bottom is a regular ruler to show the scale.

ν_y are the beam waist radii in the x and y directions, respectively. ν_x and ν_y are determined from the laser power P_0 and two radial trapping frequencies ω_x and ω_y, using $\nu_x^4 = 16(\omega_y/\omega_x^3)\alpha_s P_0/(mc)$ and $\nu_y^4 = 16(\omega_x/\omega_y^3)\alpha_s P_0/(mc)$, where $m = 1.0 \times 10^{-26}$kg is the atom mass of ^{6}Li.

3.1.4 Radio-Frequency Antenna

Most of our experiments are conducted with an equal mixture of the two lowest hyperfine states of ^{6}Li atoms. After the MOT, atoms are roughly equally distributed in the two hyperfine states. To ensure an equal population mixture, a radio-frequency antenna is installed, through which a radio frequency signal can be applied on the atoms. This antenna is shown in Fig. 3.4. In experiment, we apply a 8 G bias magnetic field accompanied by a wide band radio-frequency pulse centered at $\sim$ 7.4 MHz with a bandwidth 2 MHz. This central frequency is specifically chosen to match with the hyperfine splitting at 8 G between the

two hyperfine states we use. We apply this radio-frequency field for 0.1 second to allow rate equation pumping in a magnetic field gradient of the MOT coils. The populations are equalized between the two spin states, which optimizes the evaporative cooling efficiency for our two-component ^{6}Li fermions.

Actually, this radio-frequency technique can be used to manipulate the populations between different hyperfine states, which permits spin imbalanced mixtures.

3.1.5 Evaporative Cooling

After the radio-frequency signal to ensure the equal mixture, the magnetic field is ramped up to the broad Feshbach resonance located around 834G, where atoms are rapidly cooled by evaporation. As indicated by the name, evaporative cooling is the process which allows the "hot" atoms to escape from the trap, resulting in colder atoms in trap after rethermalization due to the collision between atoms. This evaporation process can occur actively and passively. The passive evaporative cooling, also known as free evaporative cooling, takes place spontaneously by allowing atoms with enough energy to escape from the trap. This passive evaporative cooling can cool atoms to $\sim 50\mu$K. However, this temperature is not low enough to achieve quantum degeneracy as the thermal de Broglie wavelength is still small compared to the interparticle spacing. Next, we employ forced evaporative cooling, where the trapping potential is slowly lowered so that atoms with larger energy leave the trap. This can be utilized by manipulating the CO_2 laser power. The forced evaporative cooling can be conducted at either unitary or in the weakly-interacting regime using different methods due to different collisional properties.

To reach the ultra-low temperature regime, it is necessary to have $e^{-U_0/(k_BT)} \rightarrow$

0. Hence, efficient evaporative cooling for an optical trap is realized by keeping a large ratio of the trap depth U_0 to the thermal energy k_BT, which assures that a large number of atoms remain in the trap after evaporation. After free evaporation, this ratio U_0/k_BT is found be be stagnated around 10 [53]. Through the whole evaporation, this ratio can vary if an arbitrary trap lowering curve is used. Our group carefully studied this process and derived the number scaling law as a function of trap depth for both the unitary case and weakly-interacting case, which assures holding the U/k_BT constant as the temperature is lowered to reach quantum degeneracy [53].

At unitarity, the s-wave cross section reaches the unitary limit $\sigma = 4\pi/k^2$, where k is the relative wave number of two colliding atoms. As the evaporative cooling is performed, this s-wave cross section becomes larger as the temperature and hence k drop, which will compensate the decrease of the atomic density. This produces run-away evaporative cooling. When cooled below the Fermi temperature where the degeneracy occurs, Pauli blocking severely suppresses the collisions, resulting in a decrease of thermalization rate. However, as temperature approaches the ground state, the heat capacity drops faster than the thermalization rate, which increases the efficiency for the temperature decreasing.

Experimentally, after loading into FORT, atoms are allowed to experience free evaporation for roughly 1 second with the magnetic field is tuned at 834G. After that, a lowering curve is applied to the CO_2 beam to perform forced evaporation. This lowering curve normally consists of four stages, as is shown in Fig. 3.5. First, starting at $t = t_0$, the laser power is lowered for certain amount of time until t_1. After it reaches the lowest point, the trap sits there for a short period of time until t_2. Then the trap depth is brought up to the final trap depth at t_3 and stays

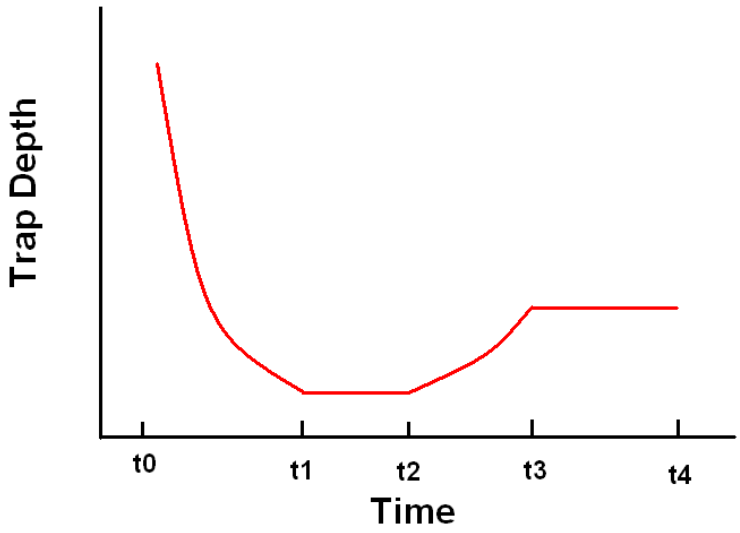

Figure 3.5: Lowering curve used for force evaporation.

there for experiments to be conducted. At t_4, the CO_2 trap is turned off, allowing the gas to expand before imaging. In order to keep constant U/k_BT, the tested best curve for this lowering part is found to be

$$U_0(t) = \gamma\, U_0(t_0)(1 + \frac{t}{\tau})^{-1.45}, \tag{3.15}$$

where γ is a parameter which offsets the trap depth.

The lowering constant τ can be set at different values. For experiments at unitarity, the tested optimal value is $\tau = 0.08\,\mathrm{s}$ and the corresponding values of t_i $(i = 0, 1, 2, 3, 4)$ are shown in Table. 3.1. With $\gamma = 1$, this lowering curve allows us to lower the trap depth down to 0.34% of the full trap depth. We can further lower the trap by setting $\gamma = 20\%$ in Eq. 3.15, which gives the lowest trap depth roughly 0.068% of the full trap depth. By doing this, we can obtain nearly the

Table 3.1: Values for parameters defined in the lowering curve at unitarity in Fig. 3.5.

	$TimePoint$	$Value(s)$
1	t_0	0
2	t_1	4
3	t_2	4.5
4	t_3	5
5	t_4	6

Table 3.2: Values for parameters defined in the lowering curve for a weakly interacting regime.

	$TimePoint$	$Value(s)$
1	t_0	0
2	t_1	10
3	t_2	10.5
4	t_3	11
5	t_4	14.5

ground state with a good number of atoms remaining in the trap.

In the weakly-interacting regime, the s-wave cross section is energy-independent $\sigma = 4\pi a^2$, where a is the s-wave scampering length. This means that the collisional rate as well as the evaporative cool rate deceases as the temperature drops, resulting in a set of parameter different from the unitary case. For experiments at 300 G, τ in Eq. 3.15 is normally set at $1s$ and the values for t_i $(i = 0, 1, 2, 3, 4)$ are shown in Table. 3.2.

3.1.6 Experimental Sequence for making a unitary Fermi gas

Using the all-optical trapping and cooling techniques discussed before, we can make a ^{6}Li unitary Fermi gas at controllable temperatures within tens of seconds. The sequence begins by loading atoms into a magneto-optical trap, which consists of three sets counter-propagating laser beams and two magnetic coils in an anti-Helmholtz configuration. The MOT has three phases: loading, cooling and optical pumping phases. In the loading phase, the MOT laser beams are detuned away from resonance to load atoms from the Zeeman slower. Then the laser beams are shifted closer to the atomic resonance and lowered in intensity to optimize the Doppler cooling efficiency in the cooling phase. After 50 ms cooling phase, an optical pumping phase follows to pump atoms from the $F = 3/2$ to $F = 1/2$ of the ^{6}Li ground state. After the optical pumping phase, MOT beams are extinguished and the MOT magnets are also switched off. Approximately 2 million atoms are then loaded into the FORT at a temperature of 140 μK and the population of the two lowest hyperfine states is balanced by a radio frequency pumping.

The FORT beam is always present throughout the whole MOT stage because the CO_2 laser beam has little effect on the MOT loading due to its far detuning from the atomic resonance. As a result, we actually need to do nothing to load atoms from MOT into FORT.

After the completion of the rf pumping, the magnetic field is ramped up to 834G within 1s. Atoms are confined in a standing wave trap formed by an incoming and retro-reflected CO_2 beams. This double pass CO_2 beam can normally triple the number of the trapped atom compared to that of the single beam case.

However, it also adds some unwanted laser noise to the trap. Hence, we slowly extinguish this retro-reflected beam before we perform evaporation. After free evaporation for 1 s at 834 G, roughly one million atoms remain in the trap with temperature down to $\sim 50\,\mu$K.

Forced evaporation at 834G is conducted after the free evaporation. As discussed above, we apply a lowering curve with parameters listed in Table. 3.1 to the CO_2 trap to bring the temperature down to quantum degeneracy. After cooling to nearly the ground state, we obtain ~ 200 thousands of atoms in trap. Controlling the lowering curve parameters enables us to cool atoms to higher temperatures. At this time, the unitary Fermi gas is ready for further experiments.

Besides making unitary Fermi gases, we also need to make non-interacting Fermi gas at 528 G for comparison. The procedure of making an ideal ^{6}Li Fermi gas is quite similar to that of a unitary Fermi gas except for the evaporative cooling because ^{6}Li atoms cannot re-thermalize at 528 G, where the gas is non-interacting. Hence, after the loading of the equal mixture of two spin states into FORT, the magnetic field is first ramped to 300 G and forced evaporation is performed using a lowering curve with different parameters as shown in Table. 3.2. Following the evaporation, the magnetic field is ramped to 528 G, where the ^{6}Li atoms are non-interacting. Evaporation is not conducted at 834 G because ramping the magnetic field from 834 G to 528 G for ^{6}Li will result in a large atom loss due to the formation of molecules on the BEC side.

3.1.7 Imaging System

Once a two component unitary Fermi gas is produced, it is crucial to correctly record the atomic cloud images for further data analysis. To achieve this goal, we

utilize a destructive process called the resonant absorption imaging. To image the clouds, the CO_2 trap is switched off to let the atoms expand for certain amount of time, which is referred to as the time-of-flight. We then apply a resonant laser beam pulse and record the shadow cast on a CCD (charge coupled device) camera positioned behind the atoms. This shadow image reveals the two-dimensional density profile of the atomic cloud.

The CCD camera is an Andor Technology DV434-BV, which consists of a 1024×1024 array of high resolution pixels measuring $13\,\mu$m on each side. A thermoelectric reduces the temperature of the camera to -40°C, to minimize the dark current for data acquisition. Before taking the images for the atomic cloud, we take a background shot, for which no atoms or imaging beam are present and the shutter to the camera is closed. This background shot will be subtracted from all of the following images we acquire. On a daily basis, this background shot can also be used to check the imaging system.

Software used for this CCD camera enables us to realize data acquisition in a variety of modes. In the so-called Fast Kinetics mode, two imaging shots are acquired. The first one is the signal shot with atoms at present. The subsequent one, normally taken 30 ms after the signal shot, is the reference shot with atoms eliminated. The time duration 30 ms between these two shots are too short for the CCD camera to read out 1024×1024 pixels, which usually takes more than 1s. To solve this problem, a razor blade is used to cover the bottom 2/3 CCD camera from the imaging beam. The signal shot can be shifted to the covered area in about 6 ms to preserve the data taken by the CCD camera. Then the reference shot can also be taken and shifted to the same covered area. If we denote the background pixel counts at position (x, z) as $I_B(x, z)$ and the total counts in the

signal and reference shots at (x, z) as I_{sig} and I_{ref}, respectively. Then we obtain,

$$I_{sig}(x,z) = I'_{sig}(x,z) + I_B(x,z)$$
$$I_{ref}(x,z) = I'_{ref}(x,z) + I_B(x,z), \tag{3.16}$$

where $I'_{sig}(x,z)$ and $I'_{ref}(x,z)$ are the pixel counts at position (x,z) with the background counts subtracted. Hence, we can obtain the absorption image

$$abs(x,z) = 100\left[1 - \frac{I'_{sig}(x,z)}{I'_{ref}(x,z)}\right], \tag{3.17}$$

where $abs(x,z)$ gives the percentage absorption for a pixel located at position (x,z)

A typical false-color absorption image with time-of-flight $300\mu s$ is shown in Fig. 3.6

The column density of this absorption image can be extracted by considering a nearly resonant light interacting with a closed two-level atomic system. This approach has been reviewed numerous times in many different sources. I will briefly introduce this approach by following Ref. [70] and Ref. [73].

We begin by considering a two level atomic cloud. If a resonant probing beam is shined on the atomic cloud, the intensity of this laser beam I can be written as

$$\frac{dI}{dy} = -n(x,y,z)\alpha(I)I, \tag{3.18}$$

where $n(x,y,z)$ is the three dimensional column density and y-axis is the direction along which the probing beam propagates. $\alpha(I)$ is the intensity dependent cross

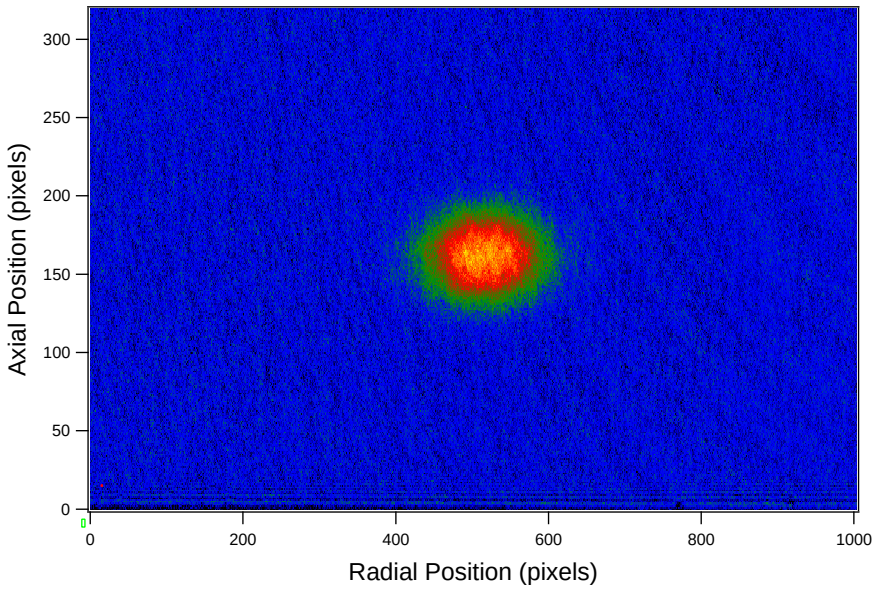

Figure 3.6: A false color absorption image showing the calculated absorptions from the measured signal and reference shot using Eq. 3.17. The time-of-flight is 300μs. The vertical and horizontal axis are the axial and radial positions in units of pixels.

section, which can be expressed as

$$\alpha(I) = \frac{\sigma_R}{1 + I/I_{sat} + \delta^2}. \tag{3.19}$$

Here $\sigma_R = 3\lambda^2/2\pi$ is the resonant optical cross section for a two-level optical transition at wavelength λ. I_{sat} is the saturation intensity and $\delta = \Delta\omega/(\Gamma_s/2)$ is the detuning of the probing beam from resonance $\Delta\omega$ in units of the half linewidth $\Gamma_s/2$.

Since the incident probe beam travels along the y-axis, we obtain the two-dimensional column density profile $n(x, z)$ from

$$n(x, z) = \int_{-\infty}^{\infty} n(x, y, z)\, dy \tag{3.20}$$

Combining Eq 3.18 through Eq 3.20, we obtain

$$n(x, z) = -\frac{1}{\sigma_R}\left(\left(1 + \delta^2\right)\ln\left[\frac{I(x, z)}{I_0(x, z)}\right] + \frac{I(x, z) - I_0(x, z)}{I_{sat}}\right), \tag{3.21}$$

where $I(x, z)$ is a measure of the beam intensity at position (x, z) after it hits the atoms and $I_0(x, z)$ is the beam intensity before hitting the atoms.

A few camera parameters need to be incorported into Eq. 3.21 to finalize this formula for the density profile. These parameters include the camera efficiency η_{cam}, camera gain g_{cam}. If we denote the maximum absorption percentage of the probing beam by the atomic cloud as ϕ. Eq. 3.21yields,

$$n(x, z) = -\frac{1}{\sigma_R}\left(\left(1 + \delta^2\right)\ln\left[\frac{I(x, z) + (\phi - 1)I_0(x, z)}{\phi I_0(x, z)}\right] + \frac{I(x, z) - I_0(x, z)}{\eta_{cam} g_{cam} I_{sat}}\right). \tag{3.22}$$

For our experiment, $\phi = 0.97$ is the fraction of the probe beaming that can be absorbed by the atoms. $g_{cam} = 1/1.4 = 0.71$ is the camera gain and $\eta_{cam} = 0.5$ is the camera efficiency. The saturation intensity I_{sat} is 2660 photons/pixels.

Once we obtain the two-dimensional density profile as shown in Eq. 3.22, we can integrate over the whole area to obtain the total atom number N. We can also fit a specific density distributionto the cloud density profile, depending on the temperature of the cloud as discussed in Chapter 2 and therefore extract the useful information from the cloud dimensions.

3.1.8 Parametric resonance

For most of the experiments, as a prerequisite, the oscillation frequencies of the atoms in trap need to be accurately measured to characterize the CO_2 laser trap potential, because they set the scale for the size and energy of the trapped gas and also determine the expansion dynamics of the atomic cloud after release. The trap frequencies can be measured through a number of methods including parametric resonance, breathing mode and radial sloshing mode. As a relatively straightforward experiment, parametric resonance is often used to measure the trap oscillation frequencies.

A parametric resonance experiment is conducted by modulating the amplitude of the CO_2 at a particular driving frequency. As the result of this modulation, energy can be coupled into the cloud, resulting in a change of the cloud size. By measuring the cloud size as a function of the modulation frequency, the trap frequencies in all directions can be accurately determined.

To perform this parametric resonance experiment, we prepare an equal mixture of the two lowest hyperfine states of ^{6}Li atoms at 300 G, at which the ^{6}Li

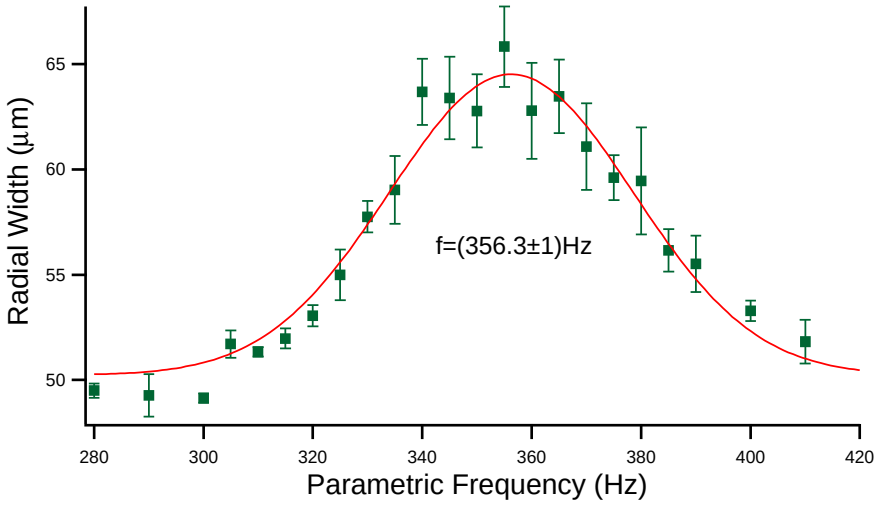

Figure 3.7: Radial cloud width versus parametric driving frequency for an axial parametric experiment. The solid circles are the experimental data and the bars denote statistical errors from the measurement. The red curve is a gaussian fit to the data. This data set provides the parametric frequency for the axial direction of the CO_2 trap. The data was taken for an optical trap at 80% of the maximum trap depth.

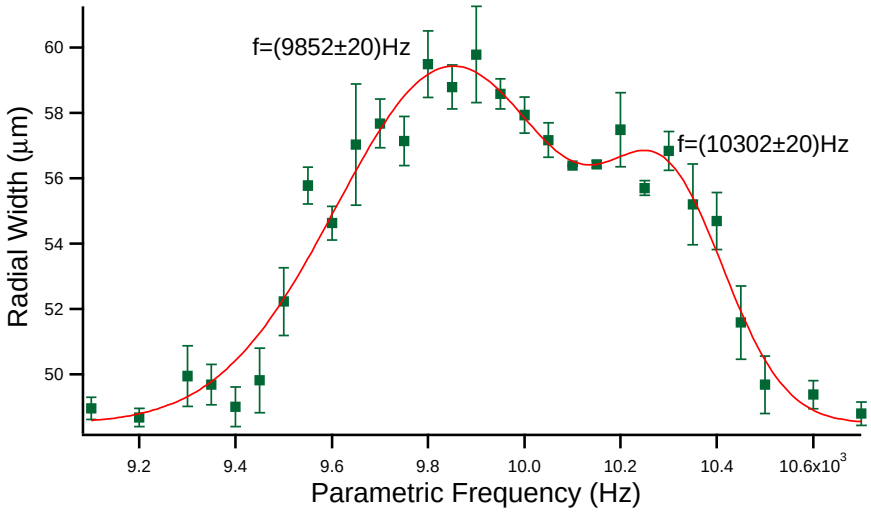

Figure 3.8: Radial cloud width versus parametric driving frequency for a radial parametric experiment. The solid circles are the experimental data and the bars denote statistical errors from the measurement. The red curve is a double gaussian fit to the data. This data set provides the parametric frequencies for the two radial directions of the CO_2 trap. The data was taken for an optical trap at 80% of the maximum trap depth.

atoms are weakly-interacted. We cool the atoms down to degeneracy in order to minimize the impact of the trap anharmonicity on the parametric measurement. We then recompress to the desired trap depth at which the actual experiment is conducted. We modulate the trap amplitude by modulating the CO_2 power though an acousto-optic modulator. After the modulation, we ramp the magnetic field up to the zero-crossing at 528G and then image the cloud. We repeat this procedure at different modulation frequencies and then plot the cloud size as a function of modulation frequencies, as shown in Fig. 3.7 and Fig. 3.8. Fig. 3.7 is a parametric resonance measurement for the axial direction and Fig. 3.8 is a parametric resonance measurement for the radial direction. Here, we use an 8 mV peak-to-peak sine wave with a duration of 1s for the amplitude modulation for the radial parametric resonance. A 70 mV peak-to-peak signal with a duration of 2s is used for the axial parametric resonance. For both cases, these amplitude modulation signals are sent through a 15 dB attenuator before being added to the DC signal which provides the CO_2 depth. This ensures less than 1% amplitude modulation of the original size of the cloud.

A parametric resonance is observed when the driving frequency is twice as its natural oscillation frequency. In other words, the largest amount of energy is coupled into the system when it is driven at twice of its natural frequency. Therefore, we can locate the peak driving frequency, at which the cloud has the largest size. The oscillation frequency of the trap is determined by dividing the resonant driving frequency by 2. As mentioned before, the axial and radial trap frequencies differ by a factor of ~ 30. As a result, it is quite easy to excite the parametric resonance for axial and radial directions independently without affecting one another.

Since our trap is not perfectly harmonic, the frequencies obtained from the measurements need to be corrected for anharmonicity to determine the harmonic oscillation frequencies for energies small compared to the trap depth. We take advantage of the following equation [70]

$$\omega_{HO}^2 = \omega_{meas}^2/[1 - E/U_0], \tag{3.23}$$

where ω_{meas} is the measured trap frequency and ω_{HO} is the corrected harmonic trap frequency for energies small compare to the trap depth. U_0 is the full trap depth and E is the initial energy per particle, both of which can be estimated using the measured cloud dimensions and the trapping frequencies (without anharmonicity correction).

3.2 Experimental setup

To experimentally realize the general procedures of making an ultra-cold Fermi gas discussed above, we need a substantial apparatus, which mainly consists of an ultra high vacuum chamber, two laser systems and a great many optics that control the path and geometry of the laser beams. This apparatus is actually replicated from the one built by former graduate students Bason Clancy and Le Luo. In this section, I will briefly introduce the layout of the high vacuum chamber and the two laser systems. A detailed discussion of this apparatus can be found in Ref. [71, 72]. Section 3.2.1 introduces the layout of a high vacuum chamber, which provides a critical work site for trapping and cooling ^{6}Li atoms. Section 3.2.2 and Section 3.2.3 discuss the two laser systems used for cooling and trapping processes: Section 3.2.2 for the dye laser system that produces

the red laser beam at frequency very close to the wanted atomic transition and Section 3.2.3 for the CO_2 laser system that creates the dipole optical trap.

3.2.1 Ultra high vacuum chamber

Our main high vacuum chamber is fabricated by MDC Vacuum Products. As shown in Fig. 3.9, the chamber has seventeen ports, one of which located at the bottom of the chamber is omitted. The main chamber is connected to the Zeeman slower, as shown in Fig. 3.1. Atoms are sent into the chamber through one port (indicated by the green arrow in Fig. 3.9) after existing the Zeeman slower, where they are slowed down by a counter propagating red-detuned laser beam. The slowing beam meets the atoms in the Zeeman slower after traveling through port S and the whole chamber. Atoms are trapped by three sets of counter-propagating MOT beams at roughly the center of the vacuum chamber. The three incoming MOT beams are sent into the chamber through ports $M1$, $M3$ and $M5$ and their corresponding counter-propagating beams are through port $M2$, $M4$ and the omitted port that is located right underneath port $M5$. The CO_2 beam travels through port $C1$ and is reflected back through port $C2$ to form a standing wave trap. R is the port for the radio-frequency power feed-through and V is the viewing port from which we can physically observe the MOT cloud by eye. The camera beam goes through the port $P1$ for imaging process and the resultant image beam travels through $P2$ and a lens that adjusts the beam size, before collected by the CCD camera installed in front of $P2$.

This main chamber maintains a vacuum around 10^{-11} Torr, making the life-time of the trapped atoms several hundred seconds [73]. This ultra high vacuum is produced and maintained by using an ion pump and a sublimation pump. The

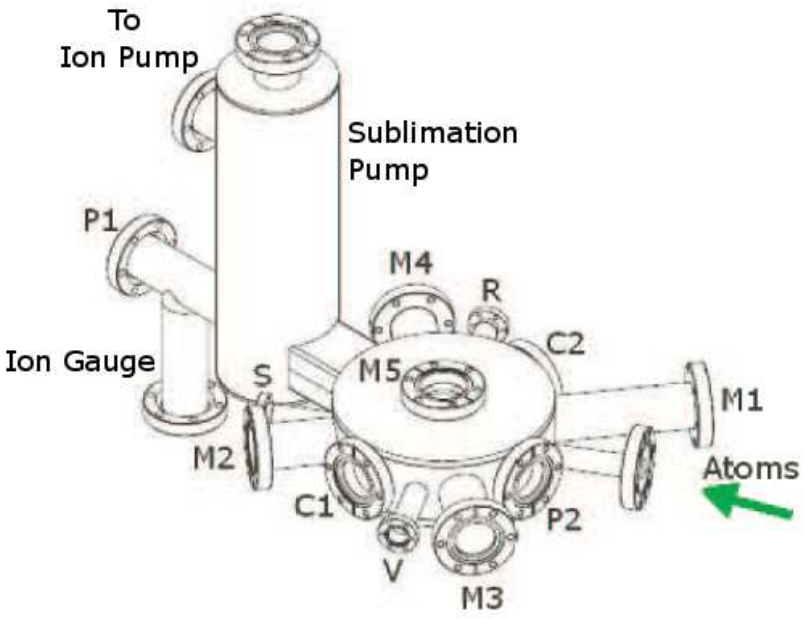

Figure 3.9: Ultra high vacuum chamber. Atoms (indicated by the green arrow) enter the chamber after existing the Zeeman slower. The slowing beam travels through port S and the whole chamber to meet the atoms in the Zeeman slower. Ports $M1$ through $M5$ are for the incoming and reflected MOT beams. Port $C1$ and $C2$ are for the CO_2 beam. R is for the radio frequency power feed-through and V is the viewing port. $P1$ and $P2$ are the two ports for the probing beam. An ion pump is attached to the chamber as shown in this figure.

ion pump ionizes and therefore pumps out the noble gases such as Helium and Argon that can slowly leak into the chamber. The sublimation pump works by creating a monolayer of titanium, which removes unwanted gas molecules from the vacuum system by sticking. Note that the ion pump and sublimation pump have some requirement on the vacuum that they can tolerate. The ion pump should be used continuously below $\leq 10^{-6}$ Torr and the sublimation pump can only be used below10^{-10} Torr.

3.2.2 Dye laser system

To conduct laser cooling and trapping, we utilize two laser systems. One is a dye laser system that produces the a number of laser beams at frequency close to the D_2 line as shown in Fig. 2.2. The dye laser beam is generated using a Coherent 899 dye laser pumped by a Coherent Verdi V-10 solid state laser, which outputs 5.5 Watts of power at 532 nm. The gain medium used in the dye laser is created using LD688 dye dissolved in 2-phenoxyethanol. The power of the dye laser needs to be optimized on a daily basis, which usually outputs a power around 700 mW.

The dye laser frequency needs to be stabilized to the resonant atomic transition. This is implemented in the lock-in region, as shown in the right most part of Fig. 3.10. A small amount of pick-off from the dye laser double-passes an acousto-optic modulator(AOM), which blue-detunes the laser beam by 220 MHz. After that, the laser beam is sent through a lock-in oven, where the atomic reference of ^{6}Li are produced. The beam is adjusted perpendicular to the atomic flux in the oven in order to avoid the Doppler boardening. A photo-multiplier tube (PMT) collects the scattered light from the oven and sends it to an electronic control box, which is connected to a lock-in amplifier. The lock-in amplifier takes

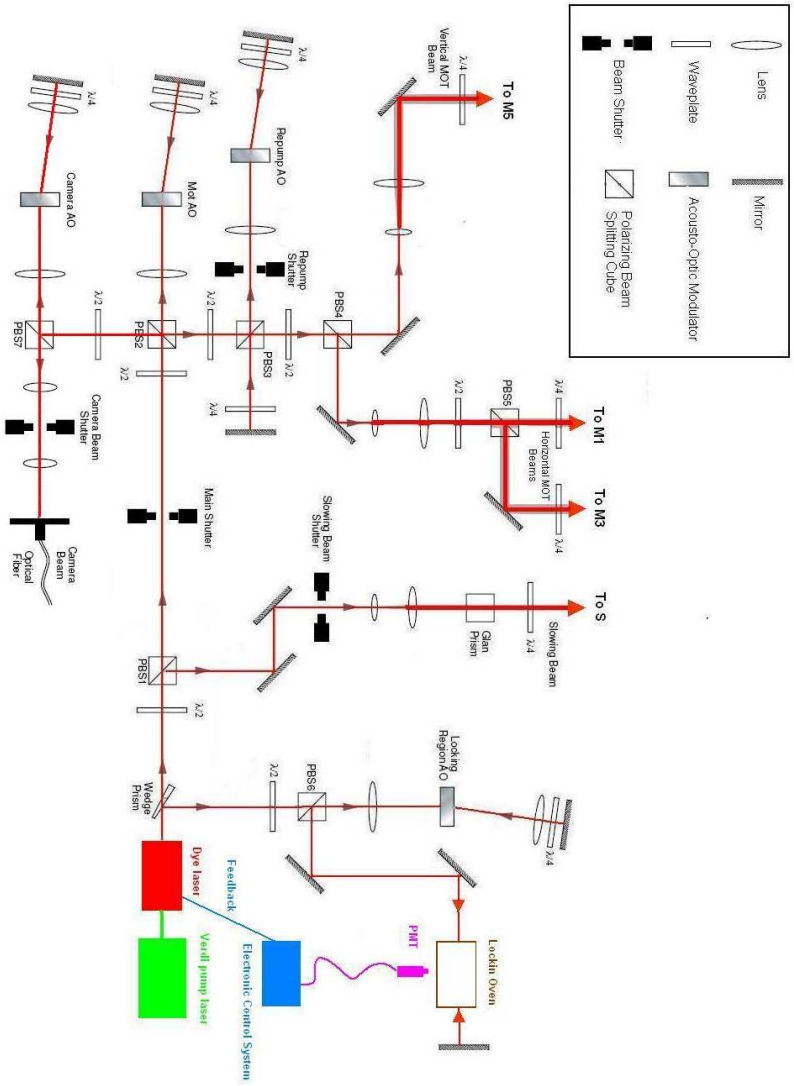

Figure 3.10: Optical layout for generating the locking region, MOT, slowing, and camera probing beams. $M1$, $M3$, $M5$ and S are the four incoming port for the slowing and three MOT beams as shown in Fig. 3.9. This figure is modified from the one published in [71].

the signal from PMT and performs the derivative of the desired atomic resonance with respect to the current frequency of the laser beam, producing a correction signal. This signal is sent to the dye laser to ensure that it is on the resonance with the desired atomic resonance. Here, the desired atomic resonance is the D_2 line transition as discussed in Fig. 2.2.

After the laser is locked to the D_2 line, a roughly 100 mW pick-off is used as the slowing light for the Zeeman slower, as shown in Fig. 3.10. Before it reaches the slowing beam port S as in Fig. 3.9, the slowing beam passes through a telescope to adjust the beam size and a quarter wave plate to produce the σ^+ polarization. The frequency of the slowing beam is the same as that of the main dye laser, which are both 220 MHz red-detuned from the D_2 transition.

After being picked off, the remaining dye laser beam is used as the MOT beams and the repump beams, as shown in Fig. 3.10. The laser beam firstly double-passes a MOT AOM to have its frequency upshifted about 185 MHz. After that, a polarizing beam splitter (PBS) breaks off the beam into two branches. A few amount of the laser power double-passes another AOM to form the repump beam. The ratio of the MOT and repump beam power is set as $3 : 1$ to optimize the loading. The frequency of the MOT beam is ~ 35 MHz below resonance, as a consequence of 220 MHz downshift from the lock-in AOM and 185 MHz upshift from the MOT AOM. This 35 MHz detuing, roughly 5 natural linewidths of the D_2 line, is chosen to optimize the MOT loading process. The repump beam is approximately 20-25 MHZ detuned below resonance. The MOT beams and repump beams are combined together and then get split by polarizing beam splitters (PBS) to form the three branches of beams. Two of the horizontal beams go into the chamber through ports $M1$ and $M3$. The rest one travels into

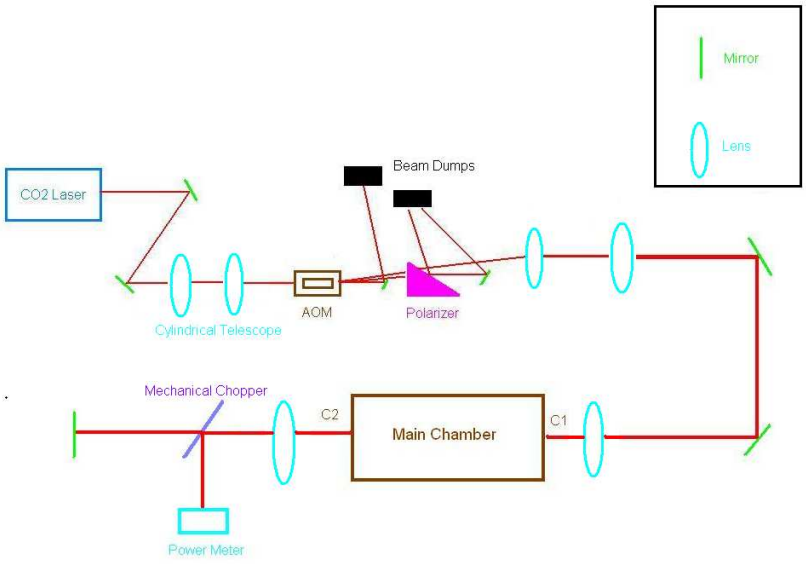

Figure 3.11: CO_2 beam layout. The CO_2 passes through a few optics before it enters the main chamber to form an optical dipole trap.

the chamber through port $M5$.

Additionally, the camera probe beam is also created from the dye laser beam, as shown in the very left part of Fig. 3.10. A small amount of the main dye laser beam is picked off before it hits the MOT AOM. This small pick-off is sent to a camera AOM to bring the beam frequency back on resonance. After traveling through a mechanical shutter and a few lens that reduce the beam size, the camera probing beam is coupled into an optical fiber. The efficiency of the fiber is usually around 40%, yielding about 3mW camera beam coming into the chamber for imaging.

3.2.3 CO_2 laser system

The dye laser beam is relatively easy to adjust as it is visible and relatively low power. However, CO_2 laser is invisible and extremely high power, which requires much more careful handling. Fig. 3.11 shows the setup for the CO_2 beam. Approximately 140 Watts of power is produced from a Coherent GEM-100 CO_2 laser and passes through a cylindrical telescope, which adjusts the beam curvature. Then the laser pass through a high power germanium AOM. When aligned properly, about 70% of the total power passes through the AOM in the first order mode, which will be used to form the dipole optical trap. The zero order passes through the AOM and then ends up going to a beam dump. The AOM is very sensitive to the temperature so that any temperature change can alter the index of refraction, causing an unwanted change in the beam path. The AOM is cooled using a mixture of distilled water and DowFrost. After the AOM, the CO_2 beam hits a polarizer, which prevents any retroreflected beam going back to the laser head. Then the CO_2 beam goes through a telescope to expand its size before it enters the main chamber. Note that all the lenses for the CO_2 beam are made out of zinc-selenide. After the main chamber, the beam gets reflected by a mechanical chopper and then goes into a powermeter. Power loss in the CO_2 optics reducces the power to around 60W at the chamber, as read by a power meter. As discussed before, to load more atoms into the CO_2 trap, the mechanical chopper is raised and a roof-top mirror is positioned behind it to reflect the CO_2 beam back into the chamber. If the beam is aligned properly, we nominally triple the number of trapped atoms, as compared to that for a single CO_2 beam. Once the loading is finished, the chopper is lowered to terminate the retroreflected beam. All the experiments presented in this thesis are conducted

in a single CO_2 beam trap.

3.3 Quantum viscosity experiments

Having made a unitary ^{6}Li Fermi gas by following the all optical methods discussed above, we are set to measure quantum shear viscosity for a unitary Fermi gas. Since the viscosity is a hydrodynamic quantity, we employ two hydrodynamic experiments, each of which focuses on a different temperature regime. At high temperatures, we perform the anisotropic expansion experiment, for which we monitor the expansion dynamics of the atomic cloud after release from the trap. For the low temperature, we use the radial breathing mode experiment, for which we study the damping of the oscillating cloud. Section 3.3.1 and Section 3.3.2 cover the experimental details of the anisotropic expansion and radial breathing mode, respectively. The experimental data from these two measurements will be analyzed to extract the shear viscosity for a unitary Fermi gas in the following chapters.

3.3.1 Anisotropic expansion

As a typical hydrodynamic experiment, anisotropic expansion has been used as an effective tool to study the hydrodynamic properties of unitary Fermi gases [7, 39]. As indicted by the name, an anisotropic optical trap is employed to confine the atoms with two tightly confined directions and one loosely confined direction. After the trap is switched off, atoms expand much faster in the two strongly confined directions than the weakly confined direction, exhibiting elliptical flow behavior, as shown in Fig. 3.12. This elliptical flow behavior is a hallmark shared by other

strongly interacting hydrodynamic systems including quark-gluon plasma [62,63]. With the presence of viscosity, the expansion in the two strongly confined directions is hindered, since the viscosity tends to transfer momentum from the two fast expanding directions to the slowly expanding one, which leads to observable slowdown as compared to ideal hydrodynamics. As a result, the anisotropic expansion experiment provides us with a good method to measure viscosity through studying the expansion dynamics of the atomic cloud.

Following the experimental sequence for making a unitary fermi gas discussed above, the CO_2 trap is recompressed to a very deep trap depth, for which the anisotropic expansion is conducted. This deep trap depth can permit to increase the energy of the atomic cloud without causing a large anharmonicity. To conduct this anisotropic expansion, we switch off the CO_2 trap and let the atoms freely expand for a certain amount of time, denoted as the time-of-flight. A destructive absorption image is then recorded by a CCD camera. One cycle of this experiment takes about 40 seconds and can be stably repeated and reproduced over hundreds of times for different time-of-light. After enough data points are gathered, they are sent to specific software to perform the data analysis.

3.3.2 Radial breathing mode

The breathing mode is a collective excitation of atoms in a trap where the atoms expand or contract at certain frequencies. It can be excited in either radial or axial directions. We use radial breathing mode to measure viscosity for the low temperature regime, as it is relatively easy to excite experimentally. The radial breathing mode is excited by release and recapture technique, as discussed in detail in [70]. The gas is initially cooled to nearly the ground state following the

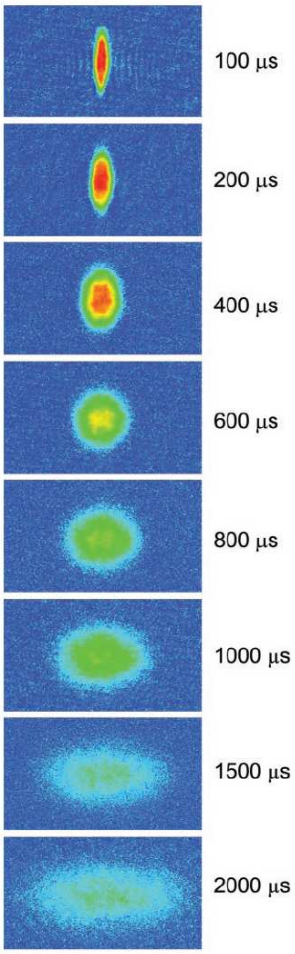

Figure 3.12: Cloud absorption images of a unitary Fermi gas after release for 0.1 to 2.0 ms. The cloud expands much faster in the transverse direction than the longitudinal direction, exhibiting elliptical flow behavior. This figure is taken from Ref. [7].

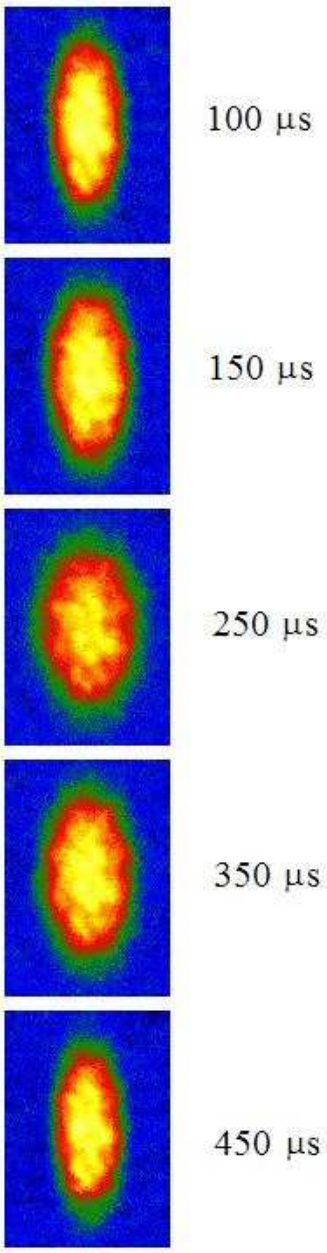

Figure 3.13: Two dimensional absorption images showing the time evolution for a radial breathing mode of a strongly interacting cloud of ^{6}Li. This strip shows roughly one complete period of oscillation. This figure is taken from Ref. [70].

general procedures discussed above. Then the trap is recompressed to the desired depth. For the radial breathing conducted at the low premature regime, we use a shallow trap in order to achieve low temperature efficiently in contrast to the deep trap used for the anisotropic expansion. We quickly turn off the optical trap (release) and turn it back on (recapture). This process is precisely controlled by an acousto-optic modulator. After we turn off the trap, the gas begins to expand for a certain amount of time t_{excite}, and then we restore the trap. We carefully control the modulation amplitude to ensure that we do not dramatically heat atoms in the trap. The expanded atomic cloud finds itself no longer in equilibrium with the restored trapping potential and therefore starts to oscillate. The oscillation of the cloud will eventually damp to a new equilibrium size, which is nearly its original size assuming that little energy is added to the cloud during the release and recapture period if the t_{excite} is very small. After we wait a certain amount of time t_{hold}, we turn off the optical trap and image. One trial of this experiment takes about 30 s and we can reproduce it hundreds of times to obtain enough data points for different t_{hold}. A two-dimensional absorption image for a radial breathing mode is shown in Fig. 3.13. The data analysis will be presented in Chapter 6.

Chapter 4

Hydrodynamic Theory

Having discussed the hydrodynamic experiments designed to measure viscosity for low and high temperature regimes in Chapter 3, we need to delve into the basic hydrodynamic theory, which is necessary to quantitatively and consistently extract viscosity from these hydrodynamic experiments. Section 4.1 introduces the fundamental hydrodynamic equations derived from first principles and the universal properties of unitary Fermi gases. These equations are applicable to both of the hydrodynamic experiments. We simplify and solve these universal hydrodynamic equations by considering the specific conditions for each experiment: Section 4.2 for the anisotropic expansion and Section 4.3 for the radial breathing mode. The results of this chapter will be used to extract viscosity from the experimental data in Chapter 6.

4.1 Fundamental hydrodynamic theory

The foundations of a non-relativistic fluid are the conservation laws of mass, energy and momentum. These conserved quantities can be expressed as an expansion in derivatives of hydrodynamic and thermodynamic variables such as fluid velocity, pressure and density [76]. Section 4.1.1 presents the leading order,

denoted as ideal hydrodynamics, for which no dissipative effects are included. The next order is the dissipative hydrodynamics discussed in Section 4.1.2. For dissipative hydrodynamics, new parameters are incorporated to describe the dissipative effects. These parameters are referred to as transport coefficients, among which viscosity is the most important one. Section 4.1.3 introduces the definition of the Knudsen number and discusses the validity of using hydrodynamic theory.

4.1.1 Ideal hydrodynamic theory

The hydrodynamic theory for a non-relativistic fluid builds on the conservation laws for mass, energy and momentum. If we denote the mass density, the energy density and the momentum density as ρ, ϵ and $\mathbf{g}$ respectively, these conversation laws can be explicitly written as [76]

$$\frac{\partial \epsilon}{\partial t} + \nabla \cdot \mathbf{j}^{\epsilon} = 0; \tag{4.1}$$

$$\frac{\partial \rho}{\partial t} + \nabla \cdot \mathbf{g} = 0; \tag{4.2}$$

$$\frac{\partial g_i}{\partial t} + \nabla_j \mathbf{\Pi}_{ij} = 0, \tag{4.3}$$

where $\mathbf{j}^{\epsilon}$ represents the energy flux density vector and $\mathbf{\Pi}_{ij}$ is called the momentum flux density tensor or the stress tensor.

The study of the motion of fluids focuses on the velocity $\mathbf{v}$ and thermodynamic variables such as pressure P and density ρ. All the other thermodynamic quantities can be expressed in terms of these three variables, along with the equation of state. Hence, the energy density flux, momentum density and stress tensor that appear in Eq 4.1 through Eq 4.3 can be determined order by order in derivatives of velocity, pressure and density. The leading order is denoted as ideal hydro-

dynamics, for which no dissipative force is included. The energy density flux, momentum density and stress tensor for ideal hydrodynamics are written as [76]

$$\mathbf{j}^{\epsilon} = \mathbf{v}(\epsilon + P); \tag{4.4}$$

$$\mathbf{g} = \rho\mathbf{v}; \tag{4.5}$$

$$\mathbf{\Pi}_{ij} = P\delta_{ij} + \rho v_i v_j. \tag{4.6}$$

Note that $\epsilon = \epsilon_0 + \frac{1}{2}\rho v^2$, where ϵ_0 is the internal energy density and $\frac{1}{2}\rho v^2$ is the kinetic energy density. The energy density ϵ is related to the pressure P through the equation of state. Inserting Eq. 4.4 through Eq 4.6 back into Eq. 4.1 through Eq. 4.3 yields two familiar equations [88],

$$\frac{\partial \rho}{\partial t} + \nabla \cdot (\rho\mathbf{v}) = 0; \tag{4.7}$$

$$\frac{\partial \mathbf{v}}{\partial t} + (\mathbf{v} \cdot \nabla)\mathbf{v} = -\frac{1}{\rho}\nabla P. \tag{4.8}$$

The first equation is called the continuity equation, while the second one is known as the Euler equation. Note that for the Euler equation, we have taken no account of the gravitational force, which is negligible. For the ideal hydrodynamics, there is no heat exchange between different parts of the whole fluid because neither the internal friction nor the thermal conductivity is important. As a result, the motion of ideal fluids must be adiabatic. Hence, the conservation of energy can be written as the conservation of entropy for ideal hydrodynamics, which is also known as the continuity equation for the entropy [88]

$$\frac{\partial s}{\partial t} + \nabla \cdot (\mathbf{v}s) = 0, \tag{4.9}$$

where s is the entropy density.

Using the Euler equation, one obtains another interesting conservation equation for an isentropic process, which involves an integral of the velocity field taken along a closed fluid contour $\oint_C \mathbf{v} \cdot d\mathbf{l}$. This integral is referred to as the velocity circulation taken around the contour $\mathbf{C}$. With the help of the Stokes' theorem, this integral yields,

$$\oint_C \mathbf{v} \cdot d\mathbf{l} = \int_S (\nabla \times \mathbf{v}) \cdot d\mathbf{S}, \tag{4.10}$$

where $\mathbf{S}$ is an arbitrary fluid surface spanning the closed contour $\mathbf{C}$. By taking time derivative on both sides, we obtain

$$\begin{aligned} \frac{d}{dt} \oint_C \mathbf{v} \cdot d\mathbf{l} &= \frac{d}{dt} \int_S \nabla \times \mathbf{v} \cdot d\mathbf{S} \\ &= \int_S \nabla \times \left(\frac{d\mathbf{v}}{dt} \right) \cdot d\mathbf{S}. \end{aligned} \tag{4.11}$$

Using the Euler equation Eq. 4.8, Eq. 4.11 is simplified as

$$\frac{d}{dt} \oint_C \mathbf{v} \cdot d\mathbf{l} = \int_S \nabla \times (-\frac{1}{\rho} \nabla P) \cdot d\mathbf{S}. \tag{4.12}$$

For an isentropic process, $\nabla P(\rho)/\rho = \nabla H$, where H is the enthalpy. Using this, Eq. 4.12 yields

$$\frac{d}{dt} \oint_C \mathbf{v} \cdot d\mathbf{l} = - \int_S \nabla \times (\nabla H) \cdot d\mathbf{S}. \tag{4.13}$$

Since the curl of the gradient of any scalar field is zero $\nabla \times \nabla \phi = 0$, we obtain the conservation of velocity circulation [88]

$$\frac{d}{dt} \oint \mathbf{v} \cdot d\mathbf{l} = 0. \tag{4.14}$$

This conservation equation shows that, for an isentropic flow of an ideal fluid, the integral of the velocity field taken along a closed fluid contour is constant in time. Note that this result does not hold when dissipative effects are considered.

4.1.2 Dissipative hydrodynamic theory

Ideal hydrodynamic theory describes the case for which no dissipative terms are considered. However, more realistically, dissipative effects occur during the motion of fluids due to thermodynamic irreversibility. This process is described by dissipative hydrodynamics, which is the next to the leading order (ideal) hydrodynamics. For the dissipative hydrodynamics, new parameters have to be introduced to describe the energy dissipation. These new parameters, known as transport coefficients, are shear viscosity η, bulk viscosity ζ and thermal conductivity κ. For a unitary Fermi gas in the first order (dissipative) hydrodynamics, the thermal conductivity $\kappa \propto l_{mfp}$ and the temperature gradient $\nabla T \propto l_{mfp}$, yielding the heat flux arising from the thermal conductivity $-\kappa \nabla T \propto l_{mfp}^2$. However, the heating rate arising from the shear η and bulk viscosity ζ is first order in l_{mfp}. Hence, we only consider the shear viscosity η and bulk viscosity ζ. While the momentum density remains the same due to Galilean invariance, the stress tensor and the energy flux density are modified as [76],

$$\begin{aligned} \mathbf{\Pi}_{ij} &= P\delta_{ij} + \rho v_i v_j + \delta\mathbf{\Pi}_{ij} \\ j_i^{\epsilon} &= v_i(\epsilon + P) + v_j \delta\mathbf{\Pi}_{ij}. \end{aligned} \tag{4.15}$$

Here, the correction to the stress tensor $\delta\mathbf{\Pi}_{ij}$ depends on the spatial derivatives of the velocity field as

$$\delta\mathbf{\Pi}_{ij} = -\eta\left(\nabla_i v_j + \nabla_j v_i - \frac{2}{3}\delta_{ij}\nabla\cdot\mathbf{v}\right) - \zeta\delta_{ij}(\nabla\cdot\mathbf{v}). \tag{4.16}$$

This correction to the stress tensor arises from both shear η and bulk viscosity ζ. Using Eq. 4.16, we can modify the Euler equation as [88]

$$\rho(\partial_t + \mathbf{v}\cdot\nabla)v_i = -\frac{\partial P}{\partial x_i} - \sum_j \partial_j(\delta\mathbf{\Pi}_{ij}). \tag{4.17}$$

This equation is called the Navier-Stokes equation, which is essentially Newton's second law in fluid mechanics. If we define a force per particle due to the scalar pressure P as

$$f_i = -\partial_i P/n, \tag{4.18}$$

we can write Eq. 4.17 in terms of the force per particle in the i^{th} direction [39]

$$m(\partial_t + \mathbf{v}\cdot\nabla)v_i = f_i - \sum_j \frac{\partial_j(\delta\mathbf{\Pi}_{ij})}{n}, \tag{4.19}$$

where m is the atom mass.

Intuitively, viscous forces always generate energy dissipation in the form of heating. In order to deal with heating arising from the viscous force, we need to investigate the convective derivative of the energy density $\mathcal{E}$

$$\frac{\mathbf{D}\mathcal{E}}{\mathbf{D}t} = \left(\frac{\partial}{\partial t} + \mathbf{v}\cdot\nabla\right)\mathcal{E}. \tag{4.20}$$

For a unitary Fermi gas as discussed in Chapter 2, the energy density scales

as $\mathcal{E} = f(\theta)n^{5/3}$, where $f(\theta)$ is the universal function of the local reduced temperature $\theta = T/T_F$. By inserting this universal relation into Eq. 4.20, we obtain

$$\left(\frac{\partial}{\partial t} + \mathbf{v}\cdot\nabla\right)\mathcal{E} = \left(\frac{\partial}{\partial t} + \mathbf{v}\cdot\nabla\right)\left(f(\theta)n^{5/3}\right). \tag{4.21}$$

Evaluating the convective derivative on $f(\theta)$ and $n^{5/3}$ separately, Eq. 4.21 yields

$$\left(\frac{\partial}{\partial t} + \mathbf{v}\cdot\nabla\right)\mathcal{E} = n^{5/3}f^{'}(\theta)\left(\frac{\partial}{\partial t} + \mathbf{v}\cdot\nabla\right)\theta + \frac{5}{3}n^{2/3}f(\theta)\left(\frac{\partial}{\partial t} + \mathbf{v}\cdot\nabla\right)n, \tag{4.22}$$

where $f^{'}(\theta) = \partial_\theta f(\theta)$. To simplify this equation, we need to investigate the convective derivative of the local reduced temperature $(\partial_t + \mathbf{v}\cdot\nabla)\theta$. Let's consider ΔN atoms in a volume element ΔV with entropy per particle s_1. The total entropy is $\Delta N s_1$ and the local number density is $n = \Delta N/\Delta V$. The total atom number ΔN is conserved along a stream tube. If this volume element absorbs an infinitesimal amount of heat ΔQ at temperature T, the entropy change of this volume element is $\Delta s^{'} = \Delta Q/T$. Thus, we have

$$\Delta N(\partial_t + \mathbf{v}\cdot\nabla)s_1 = \frac{\Delta\dot{Q}}{T}, \tag{4.23}$$

where $\Delta\dot{Q}$ is the heating rate. For unitary Fermi gases, the entropy per particle $s_1(\theta)$ is a universal function of the local reduced temperature $\theta = T/T_F$. Hence,

Eq. 4.23 is

$$\begin{aligned} T\Delta N(\partial_t + \mathbf{v}\cdot\nabla)s_1(\theta) &= \dot{q}\Delta V \\ T\frac{\Delta N}{\Delta V}\left(\partial_t + \mathbf{v}\cdot\nabla\right)s_1(\theta) &= \dot{q} \\ Tn\frac{\partial s_1}{\partial\theta}\left(\partial_t + \mathbf{v}\cdot\nabla\right)\theta &= \dot{q}, \end{aligned} \tag{4.24}$$

where $\dot{q}$ is the heating rate per unit volume. Note that at constant density the entropy per particle s_1 and the heat capacity per particle C_1 are related as

$$C_1 = T\left(\frac{\partial s_1}{\partial T}\right)_n. \tag{4.25}$$

Since

$$\begin{aligned} \frac{\partial s_1}{\partial T} &= \frac{\partial s_1}{\partial\theta}\frac{\partial\theta}{\partial T} \\ &= \frac{1}{T_F}\frac{\partial s_1}{\partial\theta}, \end{aligned} \tag{4.26}$$

Eq. 4.24 hence reduces to be

$$T\,T_F\frac{\partial s_1}{\partial T}\left(\partial_t + \mathbf{v}\cdot\nabla\right)\theta = \frac{\dot{q}}{n}. \tag{4.27}$$

Using Eq. 4.25, Eq. 4.27 yields

$$\left(\partial_t + \mathbf{v}\cdot\nabla\right)\theta = \frac{\dot{q}}{nC_1T_F}. \tag{4.28}$$

Using Eq. 4.28, Eq. 4.22 is simplified to

$$\left(\frac{\partial}{\partial t}+\mathbf{v}\cdot\nabla\right)\mathcal{E}=n^{5/3}f^{'}(\theta)\frac{\dot{q}}{C_1T_F(n)n}-\frac{5}{3}n^{2/3}f(\theta)n\nabla\cdot\mathbf{v}. \tag{4.29}$$

Note that

$$\begin{aligned}\frac{\partial\mathcal{E}}{\partial T} &= nC_1\\ \frac{\partial\left(f(\theta)n^{5/3}\right)}{\partial T} &= nC_1\\ \frac{n^{5/3}f^{'}(\theta)}{T_F(n)} &= nC_1,\end{aligned} \tag{4.30}$$

where C_1 is the specific heat capacity per particle and $T_F(n)$ is the local Fermi temperature.

Using $\mathcal{E}=f(\theta)n^{5/3}$ and Eq. 4.37, Eq. 4.29 then reduces to be the energy conservation equation

$$\left(\frac{\partial}{\partial t}+\mathbf{v}\cdot\nabla+\frac{5}{3}\nabla\cdot\mathbf{v}\right)\mathcal{E}=\dot{q}. \tag{4.31}$$

Here $\dot{q}$ represents the heat rate per unit volume arising from both shear viscosity η and bulk viscosity ζ,

$$\dot{q}=-\sum_{ij}\nabla_i v_j\,\delta\mathbf{\Pi}_{ij}, \tag{4.32}$$

where $\delta\mathbf{\Pi}_{ij}$ is defined in Eq. 4.16. If we define σ_{ij} as

$$\sigma_{ij}=\nabla_i v_j+\nabla_j v_i-\frac{2}{3}\delta_{ij}\nabla\cdot\mathbf{v}. \tag{4.33}$$

Eq. 4.16 can be written as

$$\delta\mathbf{\Pi}_{ij} = -\eta\sigma_{ij} - \zeta\delta_{ij}(\nabla\cdot\mathbf{v}). \tag{4.34}$$

Note that the tensor σ_{ij} is traceless $\mathrm{tr}(\sigma) = 0$ and symmetric $\sigma_{ij} = \sigma_{ji}$. Hence, Eq. 4.32 yields

$$\begin{aligned}
\dot{q} &= \frac{1}{2}\sum_{ij}\left(\nabla_i v_j + \nabla_j v_i\right)\eta\sigma_{ij} + \zeta(\nabla\cdot\mathbf{v})^2 \\
&= \frac{1}{2}\sum_{ij}\left(\nabla_i v_j + \nabla_j v_i - \frac{2}{3}\delta_{ij}\nabla\cdot\mathbf{v}\right)\eta\sigma_{ij} + \zeta(\nabla\cdot\mathbf{v})^2 \\
&= \eta\sum_{ij}\sigma_{ij}^2/2 + \zeta(\nabla\cdot\mathbf{v})^2
\end{aligned} \tag{4.35}$$

Using the universal relation $P = 2\mathcal{E}/3$ as shown in Eq 2.77 for a unitary Fermi gas, we can write Eq. 4.31 in terms of the scalar pressure P as

$$\left(\frac{\partial}{\partial t} + \mathbf{v}\cdot\nabla + \frac{5}{3}\nabla\cdot\mathbf{v}\right)P = \frac{2}{3}\dot{q}. \tag{4.36}$$

Using the definition of the force per particle $f_i = -\partial_i P/n$, as shown in Eq. 4.18, we can determine the convective derivative of f_i

$$\begin{aligned}
\left(\frac{\partial}{\partial t} + \mathbf{v}\cdot\nabla\right)f_i &= \left(\frac{\partial}{\partial t} + \mathbf{v}\cdot\nabla\right)\left(-\frac{\partial_i P}{n}\right) \\
\left(\frac{\partial}{\partial t} + \mathbf{v}\cdot\nabla\right)f_i &= \frac{1}{n}\left(\frac{\partial}{\partial t} + \mathbf{v}\cdot\nabla\right)(-\partial_i P) - \partial_i P\left(\frac{\partial}{\partial t} + \mathbf{v}\cdot\nabla\right)\frac{1}{n} \\
\left(\frac{\partial}{\partial t} + \mathbf{v}\cdot\nabla\right)f_i &= \frac{1}{n}\left(\frac{\partial}{\partial t} + \mathbf{v}\cdot\nabla\right)(-\partial_i P) + \frac{\partial_i P}{n^2}\left(\frac{\partial}{\partial t} + \mathbf{v}\cdot\nabla\right)n.
\end{aligned} \tag{4.37}$$

Using the continuity equation Eq. 4.7, Eq. 4.37 reduces to be

$$\left(\frac{\partial}{\partial t}+\mathbf{v}\cdot\nabla\right)f_i=-\frac{1}{n}\left(\frac{\partial}{\partial t}+\mathbf{v}\cdot\nabla\right)(\partial_i P)-\frac{\partial_i P}{n}\nabla\cdot\mathbf{v}. \tag{4.38}$$

Taking the ∂_i operator to the left of the convective derivative operator, Eq. 4.38 is shown to be

$$\begin{aligned}\left(\frac{\partial}{\partial t}+\mathbf{v}\cdot\nabla\right)f_i = &- \frac{1}{n}\partial_i\left(\frac{\partial}{\partial t}+\mathbf{v}\cdot\nabla\right)P+\sum_j\frac{(\partial_i v_j)\partial_j P}{n}-\frac{\partial_i P}{n}\nabla\cdot\mathbf{v}\\ \left(\frac{\partial}{\partial t}+\mathbf{v}\cdot\nabla\right)f_i = &- \frac{1}{n}\partial_i\left(\frac{\partial}{\partial t}+\mathbf{v}\cdot\nabla+\frac{5}{3}\nabla\cdot\mathbf{v}\right)P+\frac{5}{3}\left(\partial_i\nabla\cdot\mathbf{v}\right)\frac{P}{n}\\ &+ \frac{5}{3}\nabla\cdot\mathbf{v}\left(\frac{\partial_i P}{n}\right)+\sum_j\frac{(\partial_i v_j)\partial_j P}{n}-\frac{\partial_i P}{n}\nabla\cdot\mathbf{v}.\end{aligned} \tag{4.39}$$

Using Eq 4.36, Eq. 4.39 can be simplified as

$$\left(\frac{\partial}{\partial t}+\mathbf{v}\cdot\nabla\right)f_i=-\frac{2}{3}\frac{\partial_i\dot{q}}{n}+\frac{5}{3}\left(\partial_i\nabla\cdot\mathbf{v}\right)\frac{P}{n}-\frac{2}{3}(\nabla\cdot\mathbf{v})f_i-\sum_j(\partial_i v_j)f_j. \tag{4.40}$$

Eq 4.40 can be written as

$$\left(\partial_t+\mathbf{v}\cdot\nabla+\frac{2}{3}\nabla\cdot\mathbf{v}\right)f_i+\sum_j(\partial_i v_j)f_j-\frac{5}{3}\left(\partial_i\nabla\cdot\mathbf{v}\right)\frac{P}{n}=-\frac{2}{3}\frac{\partial_i\dot{q}}{n}. \tag{4.41}$$

Combining Eq. 4.19 and Eq. 4.41 together,

$$m(\partial_t+\mathbf{v}\cdot\nabla)v_i=f_i-\sum_j\frac{\partial_j(\delta\mathbf{\Pi}_{ij})}{n} \tag{4.42}$$

$$\left(\partial_t+\mathbf{v}\cdot\nabla+\frac{2}{3}\nabla\cdot\mathbf{v}\right)f_i+\sum_j(\partial_i v_j)f_j-\frac{5}{3}\left(\partial_i\nabla\cdot\mathbf{v}\right)\frac{P}{n}=-\frac{2}{3}\frac{\partial_i\dot{q}}{n}. \tag{4.43}$$

These two universal hydrodynamic equations properly include both the friction force and the heating arising from shear and bulk viscosities. We will simplify these two equations by making reasonable assumptions in the next section, resulting in a set of equations that can be solved and then used to extract viscosity from experiments.

4.1.3 Validity of hydrodynamic theory

The universal hydrodynamic equations Eq. 4.42 and Eq. 4.43 derived in the previous sections provide a very detailed description of the hydrodynamics of unitary Fermi gases. As a prerequisite to use these equations, we need a brief discussion on the applicability of the hydrodynamic theory. Hydrodynamic theory is valid when the mean free path l_{mfp} is much smaller than the characteristic size R of the system that is studied. The so-called Knudsen number K_n is defined

$$K_n = \frac{l_{mfp}}{R}, \tag{4.44}$$

This Knudsen number is required to be small for the hydrodynamic description to be valid and applicable. Details of this Knudsen number applied on our specific experiments will be discussed in Chapter 6.

Before we finish up this section, it is worth mentioning the ballistic expansion dynamics that has been discussed in [70]. The ballistic theory describes the expansion dynamics of a noninteracting gas, for which the hydrodynamic theory breaks and viscosity approaches infinity. We take $\sigma_i(t) = b_i(t)\sigma_i(0)$, where $\sigma_i(t)$ and $\sigma_i(0)$ are the cloud widths in the i^{th} direction at time t and 0, respectively.

The expansion factor $b_i(t)$ obeys the following equation for the ballistic expansion

$$b_i(t) = \sqrt{1 + (\omega_i t)^2}. \tag{4.45}$$

where ω_i is the optical trap frequency in the i^{th} direction. Clearly, the time evolution of the width of the cloud in each direction depends only on the trap harmonic oscillation frequency ω_i in that direction.

4.2 Universal hydrodynamic equations for the anisotropic expansion

As discussed in the previous chapter, we employ an anisotropic expansion experiment to measure viscosity for the high temperature regime. In order to quantitatively extract viscosity from the experimental data, we need to solve Eq. 4.42 and Eq. 4.43. Unfortunately, these two equations cannot be solved analytically in closed form. However, they can be greatly simplified by considering the experimental conditions of the anisotropic expansion, for which the atoms are released from a deep, nearly harmonic trap(with very small E_F/U_0). Before the optical trap is switched off, the force per particle $f_i(0)$ equals to $\partial_i U_{trap}(\mathbf{x})$ as required by the force balance when the cloud is at rest in the trap. For a harmonic trap $\partial_i U_{trap}(\mathbf{x})$ is linear in the spatial coordinates, so $f_i(0)$ is linear in the spatial coordinates accordingly. After the cloud is released from the optical trap, the force per particle as well as the velocity field remain linear as the cloud expands. Through numerical integration [43], it is shown that the nonlinearities in the velocity field are negligibly small, even if the viscosity is not zero, because dissipative forces

tend to restore a linear flow profile [39]. By assuming that the velocity field is exactly linear in the spatial coordinates, the pressure term in Eq. 4.43 vanishes since $\partial_i(\nabla \cdot \mathbf{v}) = 0$, resulting in a much simpler equation.

We then take force per particle to be linear in the spatial coordinates

$$\mathbf{f} = -\nabla P/n = a_x(t)\mathbf{x} + a_y(t)\mathbf{y} + a_z(t)\mathbf{z}, \tag{4.46}$$

where $a_x(t), a_y(t), a_z(t)$ are the three time-dependent scale factors. If we also assume that the size of the cloud changes by a scale transformation [44], we can define three time-independent parameters $\tilde{x} = x/b_x(t)$, $\tilde{y} = y/b_y(t)$ and $\tilde{z} = z/b_z(t)$, where $b_x(t)$, $b_y(t)$ and $b_z(t)$ are the time-dependent scale factors that track the overall size of the cloud in the three directions. As a result, the density of the cloud is scaled as $n(\mathbf{x}, t) = n[x/b_x(t), y/b_y(t), z/b_z(t)]/\Gamma$, where $\Gamma = b_x(t)b_y(t)b_z(t)$ is the time-dependent volume scale factor. The density profile for a unitary Fermi gas, as discussed in Chapter 2, varies with the temperature. However, for the high temperature regime, the density profile is well fit by a Gaussian distribution Eq 2.66,

$$n(x, y, z, t) = n_0(t) \exp(-x^2/\sigma_x^2 - y^2/\sigma_y^2 - z^2/\sigma_z^2), \tag{4.47}$$

where the time dependent cloud widths $\sigma_i = b_i(t)\sigma_i(0)$ and $\sigma_i(0)$ is the trapped size for each direction. $n_0(t) = N/(\pi^{3/2}\sigma_x\sigma_y\sigma_z)$ is the central density and N is the total atom number. Current conservation then requires that the velocity field

take the form

$$\begin{aligned} \mathbf{v} &= \dot{\mathbf{x}} + \dot{\mathbf{y}} + \dot{\mathbf{z}} \\ &= \dot{b}_x \tilde{\mathbf{x}} + \dot{b}_y \tilde{\mathbf{y}} + \dot{b}_z \tilde{\mathbf{z}} \\ &= \frac{\dot{b}_x}{b_x}\mathbf{x} + \frac{\dot{b}_y}{b_y}\mathbf{y} + \frac{\dot{b}_z}{b_z}\mathbf{z} \end{aligned} \tag{4.48}$$

which is linear in the spatial coordinates.

Our universal hydrodynamic equations Eq. 4.42 and Eq. 4.43 include energy dissipation arising from both shear and bulk viscosities. Fortunately, the bulk viscosity is predicted to vanish in the normal fluid phase at unitarity [45, 46]. Thus, bulk viscosity can be excluded in Eq. 4.42 and Eq. 4.43 to extract shear viscosity. More details about the bulk viscosity will be discussed in Chapter 6.

Applying these assumptions to Eq. 4.43 yields three equations, each of which governs one of the three directions of the cloud. Without loosing generality, we only show the x-direction in detail,

$$n\, x \left(\dot{a}_x + 2\frac{\dot{b_x}}{b_x}\, a_x + \frac{2}{3}\sum_j \frac{\dot{b_j}}{b_j}\, a_x \right) = -\frac{2}{3}\, \partial_x \dot{q}. \tag{4.49}$$

For zero bulk viscosity ($\zeta = 0$), the heating rate is $\dot{q} = \eta \sum_{ij} \sigma_{ij}^2/2$. Here, σ_{ij} is evaluated using Eq. 4.33. If the velocity field is spatially linear, σ_{ij} is then spatially constant. Multiplying both sides of Eq. 4.49 by x and integrating over all space yields,

$$\int d^3\mathbf{r}\, n\, x^2 \left(\dot{a}_x + 2\frac{\dot{b_x}}{b_x}\, a_i + \frac{2}{3}\sum_j \frac{\dot{b_j}}{b_j}\, a_x \right) = -\frac{1}{3}\int d^3\mathbf{r}\, x \sum_{ij} \sigma_{ij}^2 \partial_x \eta. \tag{4.50}$$

Integrating by parts on the right side and noting that σ_{ij} is spatially constant for

a linear flow field, Eq. 4.50 leads to,

$$N\langle x^2\rangle\left(\dot{a}_x + 2\frac{\dot{b_x}}{b_x}\,a_i + \frac{2}{3}\sum_j \frac{\dot{b_j}}{b_j}\,a_x\right) = -\frac{1}{3}\sum_{ij}\sigma_{ij}^2\left(\int d\mathbf{y}d\mathbf{z}\,[x\,\eta]_{-\infty}^{+\infty} - \int d^3\mathbf{r}\,\eta\right), \tag{4.51}$$

where $\langle x^2\rangle = b_x^2(t)\langle x^2\rangle_0$ with $\langle x^2\rangle_0$ as the mean square size of the trapped cloud in the x-direction.

In general, the frequency-independent(static) shear viscosity takes the universal form

$$\eta(\mathbf{r},t) = \alpha(\theta)\,\hbar n, \tag{4.52}$$

where $\theta = T/T_F(n)$ is the local reduced temperature and $T_F(n) = \hbar^2(3\pi^2 n)^{2/3}/(2mk_B)$ is the local Fermi temperature. α here is a dimensionless viscosity coefficient that only depends on the local reduced temperature θ. Kinetic theory shows that $\eta \to 0$ in the low density region of the cloud [47], as required for energy conservation. Hence, by assuming $\eta \to 0$ as $n \to 0$, the first integral on the right side of Eq. 4.51 vanishes, yielding

$$\dot{a}_x + 2\frac{\dot{b_x}}{b_x}\,a_i + \frac{2}{3}\sum_j \frac{\dot{b_j}}{b_j}\,a_x = \frac{1}{3}\frac{\int d^3\mathbf{r}\,\eta(\mathbf{r},t)}{N\langle x^2\rangle_0 b_x^2(t)}\sum_{ij}\sigma_{ij}^2. \tag{4.53}$$

Now let's consider Eq. 4.42. After simplification, the equation in the x-

direction is

$$
\begin{aligned}
n\,m\left(\partial_t\left(\frac{\dot{b}_x}{b_x}\right)+\left(\frac{\dot{b}_x}{b_x}\right)^2\right)x &= n\,a_x x-\sigma_{xx}\partial_x\eta \\
n\,m\left(\frac{\ddot{b}_x b_x-\dot{b}_x^2}{b_x^2}+\left(\frac{\dot{b}_x}{b_x}\right)^2\right)x &= n\,a_x x-\sigma_{xx}\partial_x\eta \\
n\,m\,x\frac{\ddot{b}_x}{b_x} &= n\,a_x x-\sigma_{xx}\partial_x\eta. \qquad (4.54)
\end{aligned}
$$

Similarly, we can multiply both sides by x and integrating over all space. Eq. 4.54 reduces to

$$\frac{\ddot{b}_x}{b_x}=\frac{a_x}{m}-\frac{\int d^3\mathbf{r}\,\eta(\mathbf{r},t)}{m\,N\langle x^2\rangle_0\,b^2(t)}\,\sigma_{xx}. \qquad (4.55)$$

The right hand sides of both Eq. 4.53 and Eq. 4.55 naturally depend on a new parameter called the trap-averaged viscosity coefficient $\bar{\alpha}$, which is defined as

$$\bar{\alpha}\equiv\frac{1}{N\hbar}\int d^3\mathbf{r}\,\eta(\mathbf{x},t)=\frac{1}{N}\int d^3\mathbf{r}\,n(\mathbf{x},t)\,\alpha(\theta). \qquad (4.56)$$

At a glance, a problem arises with this definition because Eq. 4.56 diverges if the viscosity scales as $T^{3/2}$ and is independent of the density n at high temperature, as predicted by kinetic theory. This situation is remedied by appreciating that at any finite time the viscosity must vanish at the edge of the cloud where the density becomes low and hydrodynamic description breaks down [47]. By making this reasonable assumption required by the energy conservation, this spatial integral exists and the trap-averaged viscosity coefficient $\bar{\alpha}$ is well defined

Note that this trap-averaged viscosity coefficient $\bar{\alpha}$ is a time-independent quantity. This can be shown by taking the convective derivative of the local reduced

temperature θ, as indicated by Eq. 4.28

$$\left(\frac{\partial}{\partial t} + \mathbf{v}\cdot\nabla\right)\theta = \frac{\dot{q}}{C_1 T_F(n) n}. \tag{4.57}$$

As the viscosity already produces a first order perturbation to ideal hydrodynamics, to a zeroth order adiabatic approximation, $\dot{q}$ can be approximated as zero in evaluating the viscosity. Hence, θ has a zero convective derivative everywhere and so does $\alpha(\theta)$. Since the number of atoms in a volume element $d^3\mathbf{r}n$ is conserved along a stream tube, $\bar{\alpha}$ is then time-independent and can be used to estimate the viscosity before release.

By defining this trap-averaged viscosity coefficient $\bar{\alpha}$, Eq. 4.53 and Eq. 4.55 reduce to

$$\dot{a}_x + 2\frac{\dot{b_x}}{b_x}a_x + \frac{2}{3}\sum_j \frac{\dot{b_j}}{b_j}a_x = \frac{1}{3}\frac{\bar{\alpha}\hbar}{\langle x^2\rangle_0 b_x^2(t)}\sum_{ij}\sigma_{ij}^2 \tag{4.58}$$

$$\frac{\ddot{b}_x}{b_x} = \frac{a_x}{m} - \frac{\bar{\alpha}\hbar}{m\,\langle x^2\rangle_0\, b_x^2(t)}\,\sigma_{xx}. \tag{4.59}$$

We can readily develop four similar equations for the other two directions by $x \to y, z$. In Chapter 6, these six equations will be solved with proper initial conditions and then fit to our anisotropic experimental data to extract viscosity.

4.3 Universal hydrodynamic equations for the radial breathing mode

For the hydrodynamic experiment used to measure viscosity at low temperatures, we employ the breathing mode, which obeys the same set of hydrodynamic

equations Eq. 4.42 and Eq. 4.43 with viscous effects included. However, the experimental conditions are different from those of the anisotropic expansion. First, the breathing mode oscillation occurs in the presence of the optical trap. Hence, we need to include the trap contribution in Eq. 4.42. The other difference is that the heating rate $\dot{q}$ arising from friction force is negligible for the breathing mode. This is because the oscillation amplitude is very small and the cloud radii change by a scale transformation of the form $b_i = 1 + \epsilon_i$, with $\epsilon_i \ll 1$. As a result, the heating rate term containing $\sigma_{ij}^2 \propto \dot{\epsilon}_i^2$ can be neglected. This is in contrast to the case for the anisotropic expansion, for which heating plays a significant role during the expansion. The effect of the heating will be described in Chapter 6. Therefore, if we incorporate these two differences in our universal equations Eq. 4.42 and Eq. 4.43, we obtain six equations for the three directions, which for the x direction are

$$\dot{a}_x + 2\frac{\dot{b_x}}{b_x}\, a_x + \frac{2}{3}\sum_j \frac{\dot{b_j}}{b_j}\, a_x = 0 \tag{4.60}$$

$$\frac{a_x}{m} - \omega_x^2 - \frac{\int d^3\mathbf{r}\, \eta(\mathbf{r},t)}{m\, N \langle x^2\rangle_0\, b_x^2(t)}\, \sigma_{xx} = \frac{\ddot{b}_x}{b_x}. \tag{4.61}$$

Note the two differences between Eq. 4.60 and Eq. 4.61 and Eq. 4.53 and Eq. 4.55. The heating rate $\dot{q}$ is ignored in Eq. 4.60 in contrast to Eq. 4.53,where $\dot{q}$ is included. The ω^2 arising from the harmonic trapping potential term is added in Eq. 4.61 while it is not included in Eq. 4.55.

Using the definition of the trap-averaged viscosity coefficient Eq. 4.56, Eq. 4.60

and Eq. 4.61 yield

$$\dot{a}_x + 2\frac{\dot{b_x}}{b_x}\, a_x + \frac{2}{3}\sum_j \frac{\dot{b_j}}{b_j}\, a_x = 0 \tag{4.62}$$

$$\frac{\ddot{b}_x}{b_x} = \frac{a_x}{m} - \omega_x^2 - \frac{\bar{\alpha}\hbar}{m\langle x^2\rangle_0\, b_x^2(t)}\, \sigma_{xx}. \tag{4.63}$$

Solving Eq. 4.62 yields $a_x = m\omega_x^2/(b_x^{8/3} b_y^{2/3} b_z^{2/3})$. Using this, Eq. 4.63 yields

$$\frac{\ddot{b}_x}{b_x} = \frac{\omega_x^2}{b_x^{8/3} b_y^{2/3} b_z^{2/3}} - \omega_x^2 - \frac{\bar{\alpha}\hbar}{m\langle x^2\rangle_0\, b_x^2(t)}\sigma_{xx}. \tag{4.64}$$

σ_{xx} can be evaluated using Eq. 4.33, yielding

$$\sigma_{xx} = \frac{2\dot{b}_x}{b_x} - \frac{2}{3}\left(\frac{\dot{b}_x}{b_x} + \frac{\dot{b}_y}{b_y} + \frac{\dot{b}_z}{b_z}\right) \tag{4.65}$$

Note that the breathing mode is excited in the two radial directions and the axial direction is hardly affected, hence $\dot{b}_z/b_z \simeq 0$. Assuming a symmetric trap $b_x = b_y$, Eq. 4.64 reduces to

$$\ddot{b}_x = b_x\omega_x^2\left(b_x^{-10/3} - 1\right) - \frac{2\bar{\alpha}\hbar\dot{b}_x}{3m\langle x^2\rangle_0\, b_x^2(t)} \tag{4.66}$$

By assuming the scale transformation $b_x = 1+\epsilon_x$ with $\epsilon_x \ll 1$ for a small amplitude oscillation, we find $\dot{b}_x = \dot{\epsilon}_x$, $\ddot{b}_x = \ddot{\epsilon}_x$ and $b_x^{-10/3} = (1+\epsilon_x)^{-10/3} = 1-10/3\epsilon_x$. Hence, Eq. 4.66 yields

$$\ddot{\epsilon}_x + \frac{2\bar{\alpha}\hbar}{3m\langle x^2\rangle_0}\dot{\epsilon}_x + \frac{10}{3}\omega_x^2\epsilon_x = 0 \tag{4.67}$$

The standard damped harmonic oscillation equation is of the form

$$\frac{d^2x}{dt^2} + \frac{2}{\tau}\frac{dx}{dt} + \omega_0^2 x = 0 \tag{4.68}$$

where $1/\tau$ is experimental the damping rate and ω_0 is the oscillation frequency. If we compare Eq. 4.67 with Eq. 4.68 and take into account the slight asymmetry of our trap with $\delta \equiv (\omega_x - \omega_y)/\sqrt{\omega_x \omega_y} << 1$, we can readily determine the oscillation frequency ω_0 and the damping rate $1/\tau$ as

$$\omega_0 = \sqrt{\frac{10}{3}\omega_x \omega_y} \tag{4.69}$$

$$\frac{1}{\tau} = \frac{\hbar\bar{\alpha}}{3m\langle x^2\rangle_0}\left(1-\delta\right), \tag{4.70}$$

where ω_x and ω_y are the two transverse frequencies.

Eq. 4.70 directly relates the damping rate $1/\tau$ to the trap-averaged viscosity coefficient $\bar{\alpha}$. In Chapter 6, we will extract the damping rate $1/\tau$ and the cloud mean square size from the experimental data and then self-consistently determine the trap-averaged viscosity coefficient $\bar{\alpha}$ using Eq. 4.70.

Chapter 5

Energy and Temperature Calibrations for Unitary Fermi Gases

As discussed in Chapter 2, unitary Fermi gases exhibit universal behaviors and all the local thermodynamic and hydrodynamic quantities depended only on the density n and the temperature T. As a result, it is of great importance to accurately measure the temperature as well as the energy for unitary Fermi gases. The calibration of the energy and temperature stand as the prerequisite to understand thermodynamic or hydrodynamic experiments conducted at unitarity. Although ^{7}Li is a thermometer for ^{6}Li, there are a number of other ways to measure the temperature and energy for unitary Fermi gases.

This chapter reports our determination of the energy as well as the temperature for a unitary Fermi gas, from nearly the ground state up to the high temperature classical regime. Section 5.1 offers a powerful method to calibrate the initial energy per particle for a unitary Fermi gas by exploiting the virial theorem [42,90]. This virial theorem allows us to calculate the energy for a harmonically trapped unitary Fermi gas from the cloud dimensions and trapping frequencies, which are both measured in our experiments. Section 5.2 covers the temperature determina-

tion for different temperature regimes. At high temperatures, we use the second virial coefficient approximation to the local energy density and hence we can readily derive the temperature as well as the entropy as a function of cloud dimensions, using fundamental thermodynamic relations and the universal properties of unitary Fermi gases. For the low temperature regime, we improve the analysis of our previous energy-entropy measurements [32] to obtain the temperature as a function of the energy, which is in good agreement with theoretical predictions. These energy and temperature calibrations can be applied on our hydrodynamic experiments at different temperatures with the specific trap conditions considered, yielding very accurate determination of the energy and temperature. Based on the energy and temperature calibration, Section 5.3 derives several thermodynamic properties that are universal and therefore are applicable to other experiments conducted at unitarity.

5.1 Energy calibrations

As studied in Chapter 2, the virial theorem Eq. 2.83 holds for a trapped unitary Fermi gas in an arbitrary trapping potential for any spin mixture, without invoking the local density approximation [90]. For a harmonic trapping potential, Eq. 2.83 yields Eq. 2.85, which allows us to calculate the initial energy per particle E from the size of the trapped cloud along any direction [32, 42]. Considering the fact that our trap is slightly anharmonic, we take advantage of Eq. 2.92 for the axial z-direction,

$$E = 3m\omega_z^2\langle z^2\rangle_0[1 - \kappa\,\langle z^2\rangle_0/\sigma_{Fz}^2], \tag{5.1}$$

where ω_z is the axial trapping frequency measured from parametric resonance as discussed in Chapter 3. $\kappa = 15E_F/(4U_0)$ corrects for anharmonicity in the trapping potential [32]. $\langle z^2 \rangle_0$ is the initial mean square size of the axial density profile of the trapped cloud and $\sigma_{Fz} = \sqrt{2E_F/(m\omega_z^2)}$ is the Fermi radius for the z-direction calculated based on the Fermi energy E_F and the trapping frequency ω_z .

The initial mean square size in the axial z-direction $\langle z^2 \rangle_0$ is determined using the following method. As discussed in Chapter 3, we first obtain the density profile from our two dimensional absorption images taken by a CCD camera. We then fit a distribution to the density profile. The type of distribution varies with the temperature of the cloud, as studied in Chapter 2. For the anisotropic expansion experiment, since we are consistently working in the high temperature regime, we fit a Gaussian distribution Eq.4.47 to the density profile and therefore extract the axial and radial widths of the Gaussian distribution denoted as $\sigma_z(t)$ and $\sigma_x(t)$, respectively. Here we denote the transverse direction that can be observed from the images as the x-direction. The widths are measured after the cloud exoands for a time-of-flight $t \sim 400\mu$s. In order to obtain the initial width of a Gaussian distribution for the trapped cloud, we use the scale transformation $\sigma_z(0) = \sigma_z(t)/b_z(t)$ as studied in Chapter 4. The scale factor $b_z(t)$ is determined by solving the universal hydrodynamic equations Eq. 4.58 and Eq. 4.59 along with proper initial conditions. Hence, we obtain $b_z(t)$ and $\sigma_z(0) = \sigma_z(t)/b_z(t)$. For a Gaussian distribution, the initial mean square size in the axial direction $\langle z^2 \rangle_0$ and the $\sigma_z(0)$ are related as $\langle z^2 \rangle_0 = \sigma_z^2(0)/2$.

The energy also can be measured from the mean square size in the two transverse directions, i.e., $z \rightarrow x$. The initial mean square size in the transverse

Table 5.1: Initial energy calculated using longitudinal E_{axial}/E_F and transverse E_{radial}/E_F cloud size. E_F is Fermi energy. The third column is the ratio.

	E_{axial}/E_F	E_{radial}/E_F	*Ratio*
1	2.15	2.07	1.04
2	2.32	2.29	1.01
3	2.34	2.23	1.05
4	2.52	2.48	1.02
5	2.58	2.5	1.03
6	2.67	2.67	1.00
7	2.93	2.84	1.03
8	3.14	3.08	1.02
9	3.34	3.22	1.04
10	3.72	3.62	1.03
11	3.78	3.39	1.12
12	4.06	3.81	1.07
13	4.28	4.00	1.07
14	4.65	4.55	1.02

x-direction $\langle x^2 \rangle_0$ is determined by following the same method as described for the axial direction. Table. 5.1 shows a good agreement between energies calculated using both the longitudinal and transverse directions. In the analysis of the anisotropic expansion experiment, we consistently use the axial direction to calculate the initial energy, as this dimension is the largest.

For the radial breathing mode experiment at low temperatures, we calculate the initial energy per particle from the cloud dimensions using Eq. 5.1 as well. Note that there are two differences between the energy calibrations of these two experiments. One is that the anharmonicity correction term $\kappa = 15E_F/(4U_0) \sim 0.25$ for the radial breathing mode is much larger than $\kappa = 15E_F/(4U_0) \sim 0.08$ for

the anisotropic expansion experiment, since we use a much shallower trap for the breathing mode experiment in order to efficiently cool down to the nearly ground state. The other difference is that for the radial breathing mode, we use the transverse x-direction to calculate the energy. We measure the radial cloud size $\sigma_x(t) = \sigma_x(0)b_x(t)$ by expanding the cloud for $t \sim 1\,\mathrm{ms}$ and then fitting a Gaussian distribution to the density profile, which is sufficiently accurate except for the few lowest temperature points for which profiles are zero-temperature Thomas-Fermi. We hence self-consistently determine $b_x(t)$ and $\bar{\alpha}$ using the hydrodynamic equations Eq. 4.60 and Eq. 4.61, along with Eq. 4.70 as a constraint. The details of this procedure will be discussed in Chapter 6. Once we obtain $b_x(t)$, $\sigma_x(0) = \sigma_x(t)/b_x(t)$ and $\langle x^2 \rangle_0 = \sigma_x^2(0)/2$, the energy can be calculated from Eq. 5.1.

5.2 Temperature calibration

While the energy can be calculated from the cloud size by exploiting the virial theorem, the temperature calibration is not as straightforward as the energy calibration. In this section, we use two methods to calibrate the temperature, one for high temperatures and one for low temperatures. In Section 5.2.1, the second virial coefficient approximation is utilized for the high temperature regime, which allows us to determine the temperature from the cloud dimensions. Using this second virial approximation, the entropy density can also be readily calculated in the high temperature regime,as discussed in Section 5.2.2. Section 5.2.3 improves the analysis of the previous measurements on the energy-entropy curve [32] for the low temperature regime. The temperature is then determined by $T = \partial E/\partial S$.

5.2.1 Temperature calibration for the high temperature regime

For the high temperature regime where the anisotropic expansion is conducted, the second virial expansion is believed to be adequate to describe the thermodynamic properties [56]. At high temperature, the grand partition function $\mathcal{Z} = \mathrm{Tr} e^{-(H-\mu N)/k_B T}$ can be expanded in the small parameter $z = e^{\mu/k_B T}$, which is called the fugacity [56]. To the second order, where interaction effects first appear, the energy density can be written as [56]

$$\mathcal{E} = (3/2) n k_B T (1 + B_2 \, n \lambda_T^3), \tag{5.2}$$

where n is the local density and $\lambda_T = h/\sqrt{2\pi m k_B T}$ is the thermal wavelength. $B_2 = 1/2^{7/2} - b_2/\sqrt{2}$ is the second virial coefficient for a unitary gas, with $b_2 = 1/2$, which is universal and known to be accurate for experiments in this temperature regime [31, 34]. Here, the first term in B_2 arises from degeneracy for each spin state of an equal mixture and the second term comes from interactions between them.

As discussed in Chapter 2, force balance in the trap requires [32, 42]

$$\int \mathcal{E} d^3\mathbf{r} = \int \frac{1}{2} n \mathbf{r} \cdot \nabla U d^3\mathbf{r}. \tag{5.3}$$

We evaluate the left side by using Eq. 5.2

$$\begin{aligned} \int \mathcal{E} d^3\mathbf{r} &= \int \frac{3}{2} n k_B T \left(1 + B_2 n \lambda_T^3\right) d^3\mathbf{r} \\ &= \frac{3}{2} N k_B T + \int \frac{3}{2} n^2 k_B T B_2 \lambda_T^3 d^3\mathbf{r}. \end{aligned} \tag{5.4}$$

Using a Gaussian distribution Eq. 4.47 for the density profile yields

$$\begin{aligned}\int \mathcal{E} d^3\mathbf{r} &= \frac{3}{2}Nk_BT + \frac{3}{2}k_BTB_2\lambda_T^3\left(\frac{N}{\pi^{3/2}\sigma_x\sigma_y\sigma_z}\right)^2\left(\frac{\pi^{3/2}\sigma_x\sigma_y\sigma_z}{2^{3/2}}\right) \\ &= \frac{3}{2}Nk_BT + \frac{3}{2}k_BTB_2\lambda_T^3\frac{N^2}{2^{3/2}\pi^{3/2}\sigma_x\sigma_y\sigma_z}. \end{aligned} \tag{5.5}$$

The thermal de Broglie wavelength is $\lambda_T = \hbar^2\sqrt{2\pi m k_B T}$, resulting in

$$\begin{aligned}\int \mathcal{E} d^3\mathbf{r} &= \frac{3}{2}Nk_BT\left(1 + \frac{NB_2\hbar^3}{(mk_BT)^{3/2}\sigma_x\sigma_y\sigma_z}\right) \\ &= \frac{3}{2}Nk_BT\left(1 + \frac{3\bar{\omega}^3NB_2\hbar^3}{3\bar{\omega}^3(mk_BT)^{3/2}\sigma_x\sigma_y\sigma_z}\right) \\ &= \frac{3}{2}Nk_BT\left(1 + \frac{(3/2)^{3/2}E_F^3B_2}{3(k_BT)^{3/2}\left(\frac{3}{2}m\omega_x^2\sigma_x^2\right)^{1/2}\left(\frac{3}{2}m\omega_y^2\sigma_y^2\right)^{1/2}\left(\frac{3}{2}m\omega_z^2\sigma_z^2\right)^{1/2}}\right) \\ &= \frac{3}{2}Nk_BT\left(1 + \frac{\sqrt{3}B_2}{2\sqrt{2}(k_BT)^{3/2}}E_F^{3/2}\frac{E_F^{3/2}}{E^{3/2}}\right). \end{aligned} \tag{5.6}$$

Using $E = 3/2m\omega_z^2\sigma_z^2$ and $E_F = 1/2m\omega_z^2\sigma_{Fz}^2 = k_BT_F$, Eq. 5.6 can be simplified,

$$\begin{aligned}\int \mathcal{E} d^3\mathbf{r} &= \frac{3}{2}Nk_BT\left(1 + \frac{\sqrt{3}B_2}{2\sqrt{2}}\left(\frac{T_{FI}}{T}\right)^{3/2}\left(\frac{\sigma_{Fz}^2}{3\sigma_z^2}\right)^{3/2}\right) \\ &= \frac{3}{2}Nk_BT\left(1 + \frac{B_2}{6\sqrt{2}}\left(\frac{T_{FI}}{T}\right)^{3/2}\left(\frac{\sigma_{Fz}^2}{\sigma_z^2}\right)^{3/2}\right) \\ &= \frac{3}{2}NE_F\frac{T}{T_{FI}}\left(1 + \frac{B_2}{6\sqrt{2}}\left(\frac{T_{FI}}{T}\right)^{3/2}\left(\frac{\sigma_{Fz}^2}{\sigma_z^2}\right)^{3/2}\right). \end{aligned} \tag{5.7}$$

Here $T_{FI} = \hbar^2(3\pi^2n_I)^{2/3}/2mk_B$ is the Fermi temperature for an ideal Fermi gas as discussed in Chapter 2. Using Eq. 2.90, we can evaluate the right side of Eq. 5.3,

which yields

$$\begin{aligned}\int \frac{1}{2} n\mathbf{r}\cdot\nabla V d^3\mathbf{r} &= \frac{3}{2}Nm\omega_z^2\langle z^2\rangle\left(1-\frac{5}{6}\frac{3m\omega_z^2\langle z^2\rangle}{U_0}\right)\\ &= \frac{3}{2}NE_F\frac{\sigma_z^2}{\sigma_{Fz}^2}\left(1-\frac{5}{2}\frac{\sigma_z^2}{\sigma_{Fz}^2}\frac{E_F}{U_0}\right). \end{aligned} \tag{5.8}$$

By equating Eq. 5.7 and Eq. 5.8, we obtain the temperature T_0 normalized to the ideal Fermi temperature T_{FI}

$$\frac{T_0}{T_{FI}} = \frac{\sigma_z^2}{\sigma_{Fz}^2}\left[1-\frac{5}{2}\frac{E_F}{U_0}\frac{\sigma_z^2}{\sigma_{Fz}^2}-\frac{B_2}{6\sqrt{2}}\frac{\sigma_{Fz}^6}{\sigma_z^6}\right]. \tag{5.9}$$

Note that Eq. 5.9 includes first order corrections arising from B_2 and trap anharmonicity. The trap anharmonicity term $5E_F\sigma_z^2/2U_0\sigma_{Fz}^2$ increases as energy increases while the B_2 term increases as energy decreases.

The local reduced temperature at the trap center θ_0 for a unitary Fermi gas can be obtained by rescaling to the local Fermi temperature $T_F(n_0)$ at the trap center

$$\theta_0 = \frac{T_0}{T_F(n_0)} = \frac{T_0}{T_{FI}}\left(\frac{n_I}{n_0}\right)^{2/3}, \tag{5.10}$$

where n_I and n_0 are the central density for an ideal gas and unitary gas, respectively. For a ground state ideal gas, the density profile is well described by a zero temperature Thomas-Fermi distribution as shown in Eq. 2.65. Hence, for T_{FI} we use the central density $n_I = 8N/(\pi^2\sigma_{Fx}\sigma_{Fy}\sigma_{Fz})$. For a unitary Fermi gas at high temperatures, we fit a Gaussian distribution Eq. 4.47 with the central density $n_0 = N/(\pi^{3/2}\sigma_x\sigma_y\sigma_z)$. As a result, Eq. 5.10 can be written as

$$\theta_0 = \frac{T_0}{T_F(n_0)} = \frac{4}{\pi^{1/3}}\left(\frac{\sigma_z}{\sigma_{Fz}}\right)^2\left(\frac{T_0}{T_{FI}}\right), \tag{5.11}$$

where we use $\sigma_x/\sigma_{Fx} = \sigma_y/\sigma_{Fy} = \sigma_z/\sigma_{Fz}$. In this way, we can obtain the local reduced temperature from the size of the cloud at high temperature. Since $\sigma_z^2/\sigma_{Fz}^2 \propto E/E_F$ and $T_0/T_{FI} \propto E/E_F$, Eq. 5.11 yields $\theta \propto (E/E_F)^2$.

Using Eq. 5.9 and Eq. 5.11, we can calibrate the temperature for the high temperature anisotropic expansion experiment from the measured cloud size. However, this method is valid only in a high temperature regime where the second virial expansion holds and breaks down at low temperatures. For the low temperatures, we will use another method to calibrate the temperature.

5.2.2 Determination of Entropy density in the high temperature regime

Besides the temperature, the entropy density can also be derived using the second virial approximation for a unitary Fermi gas in the high temperature regime. We begin by considering the phase space density $n\lambda_T^3$. Using the definition of thermal de Broglie wavelength $\lambda_T = h/\sqrt{2\pi m k_B T}$, the phase space density can be written as

$$n\lambda_T^3 = \frac{nh^3}{(2\pi m k_B T)^{3/2}}. \tag{5.12}$$

By considering the Fermi temperature $T_F = \hbar^2(3\pi^2 n)^{2/3}/2mk_B$, the number density n can be expressed in terms of Fermi temperature T_F as $n = (2mk_B T_F)^{3/2}/(3\pi^2\hbar^3)$.

Hence, Eq. 5.12 yields,

$$\begin{aligned} n\lambda_T^3 &= \frac{h^3}{(2\pi m k_B T)^{3/2}} \frac{(2\pi m k_b T_F)^{3/2}}{3\pi^2 \hbar^3} \\ &= \frac{8}{3\sqrt{\pi}} \left(\frac{T_F}{T}\right)^{3/2} \\ &= \frac{8}{3\sqrt{\pi}} \theta^{-3/2}. \end{aligned} \tag{5.13}$$

Inserting this equation into Eq. 5.2, the energy density $\mathcal{E}$ can be written as

$$\begin{aligned} \mathcal{E} &= (3/2) n k_B T (1 + B_2\, n\lambda_T^3) \\ &= (3/2) n k_B T_F \frac{T}{T_F} \left(1 + \frac{8}{3\sqrt{\pi}} B_2 \theta^{-3/2}\right) \\ &= (3/2) n \epsilon_F \left(\theta + \frac{8}{3\sqrt{\pi}} B_2 \theta^{-1/2}\right). \end{aligned} \tag{5.14}$$

Note the fundamental thermodynamic relation

$$\left(\frac{\partial \mathcal{E}}{\partial T}\right)_n = T \left(\frac{\partial s}{\partial T}\right)_n. \tag{5.15}$$

In order to relate the local reduced temperature θ in this relation, Eq. 5.15 can be written as

$$\begin{aligned} \left(\frac{\partial \mathcal{E}}{\partial \theta}\right)_n \left(\frac{\partial \theta}{\partial T}\right) &= T \left(\frac{\partial s}{\partial \theta}\right)_n \left(\frac{\partial \theta}{\partial T}\right) \\ \frac{1}{T} \left(\frac{\partial \mathcal{E}}{\partial \theta}\right)_n &= \left(\frac{\partial s}{\partial \theta}\right)_n. \end{aligned} \tag{5.16}$$

Using Eq. 5.16, the entropy density s can be obtained by taking derivatives of the energy density $\mathcal{E}$ with respect to the local reduced temperature θ and then integrated with respective to θ. We first take derivatives of the energy density $\mathcal{E}$

in Eq. 5.14 , yielding

$$\frac{\partial s}{\partial \theta} = \frac{1}{T}\frac{\partial \mathcal{E}}{\partial \theta} = \frac{3nk_B}{2\theta}\left(1 - \frac{4}{3\sqrt{\pi}}B_2\theta^{-3/2}\right). \tag{5.17}$$

Integrating the right side of Eq. 5.17 with respect to θ, the entropy density s can be written as

$$s = nk_B\left(\ln\theta^{3/2} + \frac{4}{3\sqrt{\pi}}B_2\theta^{-3/2} + C\right), \tag{5.18}$$

where C is an integration constant, which is independent of the density n and the temperature T. This constant is determined by considering the fact that Eq. 5.18 has to recover the Sackur-Tetrode entropy for classical gases when it approaches the high temperature classical limit $\theta \gg 1$. The Sackur-Tetrode entropy for a $50-50$ mixture classical gas is

$$s = nk_B\left(-\ln\frac{n\lambda_T^3}{2} + \frac{5}{2}\right). \tag{5.19}$$

Using the relation between the phase space density and the local reduced temperature θ in Eq. 5.13 and comparing Eq. 5.19 to Eq. 5.18, the constant C is hence determined as

$$C = \frac{5}{2} - \ln\frac{4}{3\sqrt{\pi}}. \tag{5.20}$$

Note that the B_2 term in Eq. 5.18 vanishes as $\theta^{-3/2} \ll 1$ in the high temperature limit. Eq. 5.18 then yields

$$s = nk_B\left(\frac{5}{2} + \ln\theta^{3/2} + \frac{4}{3\sqrt{\pi}}B_2\theta^{-3/2} - \ln\frac{4}{3\sqrt{\pi}}\right). \tag{5.21}$$

If we write the local reduced temperature in terms of the phase space density $n\lambda_T^3$, Eq. 5.21 reduces to

$$s = nk_B \left(\frac{5}{2} - \ln \frac{n\lambda_T^3}{2} + \frac{B_2}{2} n\lambda_T^3 \right). \tag{5.22}$$

Eq. 5.21 or Eq. 5.22 is the entropy density s for a unitary Fermi gas with two balanced species at high temperatures, for which the fugacity is small and the second virial coefficient approximation is valid.

With the help of Eq. 5.22, we can readily calculate the trap-averaged entropy per particle S

$$\begin{aligned} S &= \frac{1}{N} \int d^3\mathbf{r}\, s \\ &= \frac{k_B}{N} \int d^3\mathbf{r}\, n \left(\frac{5}{2} - \ln \frac{n\lambda_T^3}{2} + \frac{B_2}{2} n\lambda_T^3 \right). \end{aligned} \tag{5.23}$$

If we fit a Gaussian distribution $n = n_0 \exp(-x^2/\sigma_x^2 - y^2/\sigma_y^2 - z^2/\sigma_z^2)$ to the density profile at high temperatures, the integral in Eq. 5.23 can be written as

$$S = \frac{k_B}{N} \left(\int d^3\mathbf{r}\, n \left(\frac{5}{2} - \ln \frac{n_0\lambda_T^3}{2} \right) + \frac{B_2\lambda_T^3}{2} \int d^3\mathbf{r}\, n^2 + \int d^3\mathbf{r}\, n \ln \frac{n_0}{n} \right), \tag{5.24}$$

where $n_0(t) = N/(\pi^{3/2}\sigma_x\sigma_y\sigma_z)$ is the central density. The first integral on Eq. 5.24 can be easily evaluated as

$$\int d^3\mathbf{r}\, n \left(\frac{5}{2} - \ln \frac{n_0\lambda_T^3}{2} \right) = N \left(\frac{5}{2} - \ln \frac{n_0\lambda_T^3}{2} \right). \tag{5.25}$$

Table 5.2: The energy E/E_F, the temperature T/T_{FI}, the local reduced temperature at the trap center for a unitary Fermi gas $T/T_F(n_0)$ and the trap-averaged entropy per particle S in units of k_B for the anisotropic expansion measurement in the high temperature regime. E/E_F is calibrated from the axial cloud size using Eq. 5.1. T/T_{FI} is calculated from the cloud dimensions using Eq. 5.9 derived from the second virial coefficient approximation. $T/T_F(n_0)$ is then obtained by scaling the central density using Eq. 5.11. S/k_B is obtained using Eq. 5.28. E_F is the ideal gas Fermi energy and T_{FI} is the corresponding Fermi temperature.

	E/E_F	T/T_{FI}	$T/T_F(n)$	S/k_B
1	2.15(2)	0.770(6)	1.54(3)	4.93(3)
2	2.32(4)	0.815(9)	1.78(5)	5.15(4)
3	2.34(4)	0.820(9)	1.80(5)	5.17(4)
4	2.52(4)	0.874(12)	2.07(6)	5.38(4)
5	2.58(2)	0.891(7)	2.15(4)	5.43(3)
6	2.67(5)	0.917(13)	2.31(8)	5.54(5)
7	2.93(5)	0.995(12)	2.77(8)	5.81(4)
8	3.14(3)	1.060(8)	3.15(4)	6.00(2)
9	3.34(5)	1.120(12)	3.56(10)	6.19(4)
10	3.72(5)	1.240(13)	4.41(12)	6.51(4)
11	3.78(5)	1.250(12)	4.57(10)	6.56(3)
12	4.06(7)	1.340(15)	5.25(19)	6.77(5)
13	4.28(10)	1.41(20)	5.84(28)	6.93(7)
14	4.65(10)	1.53(20)	6.90(31)	7.18(7)

The second integral involving n^2 can be evaluated as

$$\frac{B_2\lambda_T^3}{2}\int d^3\mathbf{r}\, n_0^2 \exp\left(-\frac{2x^2}{\sigma_x^2}-\frac{2y^2}{\sigma_y^2}-\frac{2z^2}{\sigma_z^2}\right)=\frac{Nn_0B_2\lambda_T^3}{2^{5/2}}. \tag{5.26}$$

The last integral is calculated to be

$$\int d^3\mathbf{r}\, n\left(\frac{x^2}{\sigma_x^2}+\frac{y^2}{\sigma_y^2}+\frac{z^2}{\sigma_z^2}\right)=\frac{3Nk_B}{2}. \tag{5.27}$$

Using Eq. 5.25 through Eq. 5.27 and Eq. 5.13, Eq. 5.24 yields the trap-averaged entropy per particle S as a function of the local reduced temperature at the trap center θ_0

$$S=k_B\left[4-\ln\left(\frac{4}{3\sqrt{\pi}}\right)+\frac{3}{2}\ln\theta_0+\sqrt{\frac{2}{\pi}}\frac{B_2}{3}\,\theta_0^{-3/2}\right]. \tag{5.28}$$

Table. 5.2 gives the energy E/E_F, the temperature T/T_{FI}, the local reduced temperature at the trap center $T/T_F(n_0)$ and the trap-averaged entropy per particle S in units of k_B for the high temperature regime.

5.2.3 Temperature calibration for the low temperature regime

The second virial coefficient method used for the high temperature calibration is not valid for the low temperature regime, since the fugacity e^{μ/k_BT} or the phase space density $n\lambda^3$ is not a small quantity at low temperatures. Instead, we take advantage of our previous measurements of energy versus entropy [29, 32], which has the same shallow trap depth as that used for the low temperature breathing mode measurements. The basic idea of the energy versus entropy measurements is that if the energy per particle E and the entropy per particle S are measured,

an E versus S curve can be generated and the temperature is then determined by using the basic thermodynamic relation $T = \partial E/\partial S$. Experimentally, the energy E of a unitary Fermi gas is calculated from the cloud size at unitarity by using the virial theorem as discussed above. The entropy S cannot be obtained directly from the cloud size at unitarity. However, we can adiabatically sweep the magnetic field from 840 G up to 1200 G, which brings the gas from the unitary regime into a weakly interacting regime. The entropy for a weakly interacting Fermi gas can be calculated from the cloud size using ideal gas approximation and can be more accurately calculated by including the small interactions using an exact many-body calculation [31]. Hence, we can obtain the entropy for a unitary Fermi Fermi gas from the entropy of a weakly interacting Fermi gas because the entropy is conserved throughout this adiabatic sweep. The adibaticity of this sweep is confirmed by comparing the mean square size of the cloud at 840G after a 2 second round-trip sweep to that obtained without a sweep after a hold time of 2 seconds at 840G [29]. The difference is found to be within 3% [29]. The details of the experimental procedures and results of the energy-entropy measurements have been reported by our group in Ref. [29, 32]. Here we can make two improvements in the analysis to better determine the temperature of a unitary Fermi gas at low temperatures. First, we parameterize the measured energy per particle E and measured entropy per particle S curve using the data for E_{840}/E_F, S^*_{1200}/k_B given in Table 1 of Ref. [32], as listed in Table. 5.3. The E_{840}/E_F is corrected for anharmonicity with $E_F/U_0 \sim 0.1$. The S^*_{1200}/k_B data is corrected for the finite interaction strength using many-body calculations at 1200 G [57], which is more accurate than the ideal gas entropy S_{1200}/k_B used to determine the temperature in Ref. [32]. Second, since the temperature is the first derivative of energy with

Table 5.3: Energy, and entropy measured in a trapped unitary Fermi gas. E_{840}/E_F is the energy per particle of a unitary Fermi gas at 840 G, calculated using Eq. 5.1. S^*_{1200}/k_B is the corresponding entropy per particle of the gas after an adiabatic sweep of magnetic field from 840 G to 1200 G, calculated using an exact many-body calculation for $k_F a = -0.75$ [31]. This data is taken from Ref. [32].

	E_{840}/E_F	S^*_{1200}/k_B
1	0.548(4)	0.91(23)
2	0.589(5)	1.18(22)
3	0.634(5)	1.36(20)
4	0.667(8)	1.43(18)
5	0.71(1)	1.72(18)
6	0.75(1)	1.79(15)
7	0.79(1)	2.03(16)
8	0.84(2)	2.32(18)
9	0.86(1)	2.31(16)
10	0.91(1)	2.57(17)
11	0.94(1)	2.75(19)
12	0.98(1)	2.80(17)
13	1.03(1)	2.90(15)
14	1.15(1)	3.20(14)
15	1.18(1)	3.28(14)
16	1.31(2)	3.48(9)
17	1.39(2)	3.73(11)
18	1.42(1)	3.74(8)
19	1.52(1)	3.92(7)
20	1.62(4)	4.01(1)
21	1.70(2)	4.26(6)
22	1.83(4)	4.53(7)

respect to entropy, it is important to include some points at the highest end of the experimental data as constraints otherwise the temperature of the few highest points would be inaccurate. We note that the highest energy data point from Ref. [32] is at $E/E_F = 2$, where the aforementioned high temperature second virial expansion method is proven to be valid [31, 34]. With the help of Eq. 5.28, we are able to calculate the trap-averaged entropy per particle S as a function of the local reduced temperature at the trap center θ_0. Since the local reduced temperature θ_0 is related to the cloud size through Eq. 5.9 and Eq. 5.11 and the energy can be written in terms of the cloud size using the virial theorem Eq. 5.1, we can obtain a theoretical energy-entropy function for the high temperature regime, where the second virial approximation is valid. We then join the experimental $E(S)$ data with the theoretical calculations of E and S to constrain the high temperature end, as shown in Fig. 5.1.

After making these improvements, we are able to determine the temperature by fitting a smooth curve to the $E(S)$ data and then apply $T = \partial E/\partial S$. Here this smooth curve is divided into two regions by the normal-superfluid transition point S_c. As discussed in Ref. [32], we can either fit a smooth curve with a continuous or a discontinuous heat capacity at S_c determined by the best fit, which approximately determines the critical energy E_c and critical temperature T_c for the normal-super fluid transition point. For simplicity, we use a smooth curve with a discontinuous heat capacity [32] with simple power laws above and below S_c

$$\begin{aligned} E_<(S) &= E_0 + aS^b; \quad 0 \le S \le S_c \\ E_>(S) &= E_1 + cS^d; \quad S \ge S_c, \end{aligned} \tag{5.29}$$

where E and S are in units of E_F and k_B, respectively. Note that we initially have seven fitting parameters. However, the energy and temperature have to be continuous at the transition point S_c

$$\begin{aligned} E_<(S_c) &= E_>(S_c) \\ \left(\frac{\partial E_<}{\partial S}\right)_{S_c} &= \left(\frac{\partial E_>}{\partial S}\right)_{S_c}. \end{aligned} \tag{5.30}$$

This reduces the seven fitting parameters down to five and our power law fitting function Eq. 5.29 takes the form

$$\begin{aligned} E_<(S) &= E_0 + aS^b; \quad 0 \le S \le S_c \\ E_>(S) &= E_0 + aS_c^b\,[1 - b/d + b/d(S/S_c)^d]; \quad S \ge S_c. \end{aligned} \tag{5.31}$$

where E_0, S_c, a, b and d are the five independent parameters that can be determined by fitting this curve to the energy-entropy curve.

Note that the ground state energy $E_0 = \sqrt{1+\beta}E_{ideal}$, where $E_{ideal} = 0.75$ is the ideal gas ground state energy and β is the universal energy parameter which scales the ground state energy for an ideal Fermi gas to a unitary Fermi gas, as discussed in Chapter 2. By setting $\beta = -0.60(2)$ [32], We can fix the ground state energy $E_0 = 0.47$, which yields only four free parameters for the fitting curve Eq. 5.31.

Then we use a χ^2 fit by giving equal weighting to the low temperature experimental data points and the high temperature calculated points. The best χ^2 yields the four free parameters as shown in Table. 5.4. The critical energy obtained from the fit is $E_c = 0.78(12)\,E_F$. Then, $T = \partial E/\partial S$ yields $T_c = 0.24(8)\,T_{FI}$. Note that

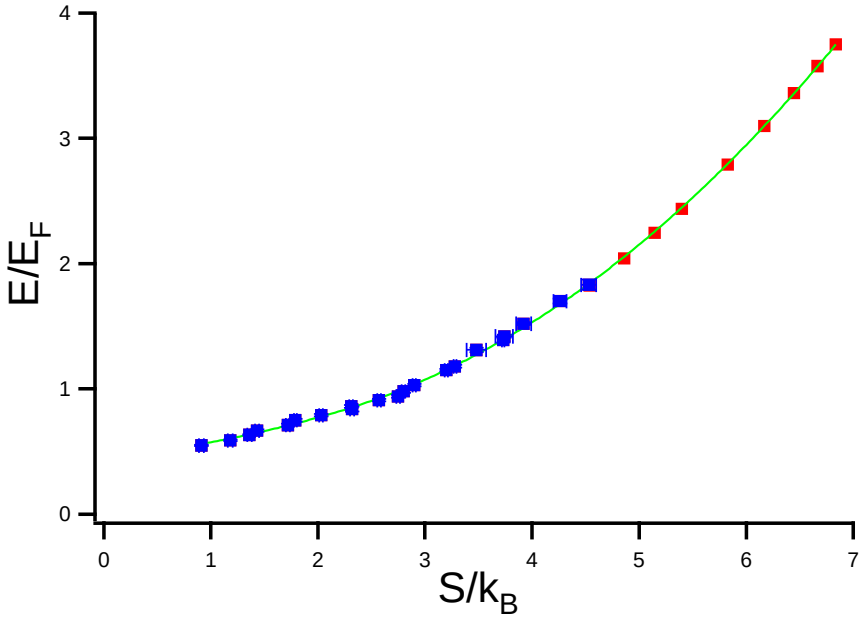

Figure 5.1: Total energy per particle of a unitary Fermi gas at 840 G versus the entropy per particle. The blue dots show the entropy obtained by adiabatically sweeping the magnetic field from $840G$ to $1200G$ and using an exact many-body calculation [31] for the entropy at 1200 G, where $k_F a = -0.75$ [See Table. 5.3]. The red dots are the theoretical calculations using the second virial coefficient approximation including the trap anharmonicity for the trap condition of Ref. [29]. The green curve is the power law fit with a discontinuous heat capacity, as described in Eq. 5.31.

Table 5.4: Fitted values for a, b, d and S_c for the power law curve Eq. 5.31.

	Value
a	0.10(1)
b	1.57(15)
d	2.23(3)
S_c	2.04(39)

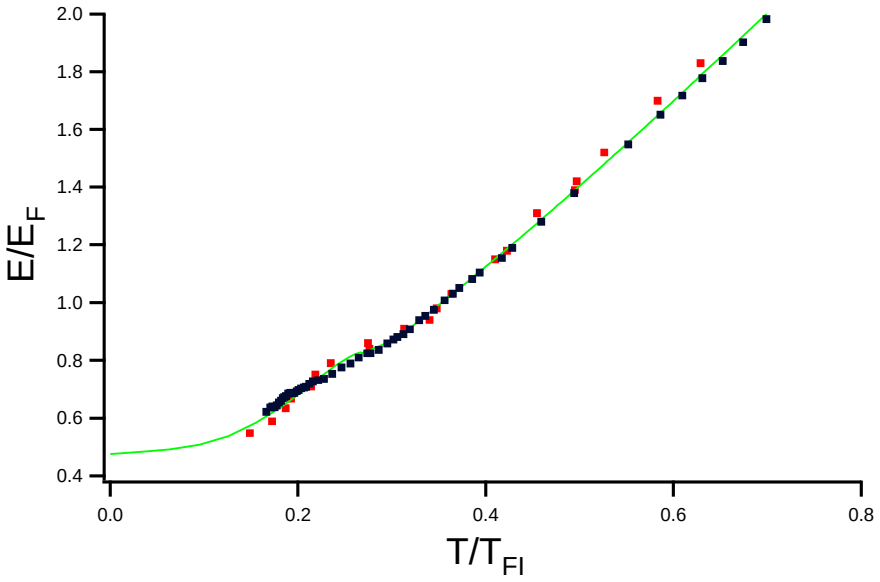

Figure 5.2: Measured energy versus the temperature obtained from the calibration of Eq. 5.31 (red squares); For comparison, we show the data obtained by the ENS group [34] (black squares) and the theory of Hu et al. [58] (green curve).

the relatively large error bar for S_c and hence T_c arises from joining measured data with the calculated high temperature points, and fitting $E_>(S)$ by a single power law. However, this method yields a smooth temperature calibration that reproduces the temperatures used in the virial calculation to better than 3%.

Applying $T = \partial E/\partial S$, we can determine E/E_F versus T/T_{FI}, shown in Fig. 5.2. Fig. 5.2 shows that our new calibration agrees very well with other measurements [34] as well as the NSR theory [58]. Using this temperature calibration, we can obtain the temperature for the radial breathing mode experiments, which are conducted at low temperatures. The central density n_0, prior to release is determined from column density of the trapped cloud by fitting the spatial profile with a Gaussian distribution, which is adequate except at the lowest temperature where the density profile is a zero-temperature Thomas-Fermi Distribution. We

then calculate the local reduced temperature at the trap center θ_0 from the same equation Eq. 5.11 as used for the high temperature calibration. Table. 5.5 gives the energy E/E_F, the temperature T/T_{FI}, the local reduced temperature at the trap center $T/T_F(n_0)$ and the trap-averaged entropy per particle S in units of k_B for the radial breathing mode experiments. Together with Table. 5.2 for the high temperature measurements, this provides a complete calibration of the energy and temperature for a unitary fermi gas.

5.3 Derivation of universal thermodynamic functions

With the help of the power law fit for a heat capacity jump curve as shown in Eq. 5.31 and the fitted values as in Table. 5.4, we can readily generate several universal thermodynamic functions.

The first one is the energy as a function of temperature [32],

$$\begin{aligned} E_<(T) &= E_c + \frac{S_c T_c}{b}\left(\left(\frac{T}{T_c}\right)^{\frac{b}{b-1}} - 1\right);\ 0 \le T \le T_c \\ E_>(T) &= E_c + \frac{S_c T_c}{d}\left(\left(\frac{T}{T_c}\right)^{\frac{d}{d-1}} - 1\right);\ T \ge T_c. \end{aligned} \tag{5.32}$$

Using the fitted values in Table. 5.4, we can plot E/E_F as a function of T/T_{FI} in Fig. 5.3.

The second universal function is the entropy as a function of the tempera-

Table 5.5: The energy E/E_F, the temperature T/T_{FI}, the local reduced temperature at the trap center for a unitary Fermi gas $T/T_F(n)$ and the trap-averaged entropy per particle S in units of k_B for the radial breathing mode experiments. E/E_F is determined from the radial cloud size using Eq. 5.1. T/T_{FI} is obtained using Eq. 5.31 and the fitted parameters listed in Table. 5.4. $T/T_F(n_0)$ is then obtained by scaling the central density using Eq. 5.11. S/k_B is obtained using Eq. 5.31. E_F is the ideal gas Fermi energy and T_{FI} is the corresponding Fermi temperature.

	E/E_F	T/T_{FI}	$T/T_F(n_0)$	S/k_B
1	0.55(1)	0.142(20)	0.072(10)	0.84(8)
2	0.56(1)	0.149(22)	0.078(12)	0.91(7)
3	0.59(1)	0.166(27)	0.092(15)	1.10(6)
4	0.67(1)	0.200(33)	0.126(21)	1.54(6)
5	0.83(2)	0.264(6)	0.208(5)	2.24(8)
6	1.00(2)	0.347(15)	0.331(15)	2.80(5)
7	1.03(2)	0.360(17)	0.354(16)	2.88(4)
8	1.08(2)	0.381(19)	0.395(20)	3.01(5)
9	1.08(2)	0.381(19)	0.393(20)	3.01(4)
10	1.12(2)	0.397(20)	0.428(22)	3,12(5)
11	1.14(3)	0.405(21)	0.445(23)	3,17(7)
12	1.15(2)	0.409(21)	0.453(24)	3.19(5)
13	1.25(2)	0.446(26)	0.539(31)	3.43(5)
14	1.43(3)	0.507(32)	0.704(44)	3.80(5)
15	1.60(3)	0.560(37)	0.879(58)	4.12(5)
16	1.60(3)	0.560(37)	0.881(58)	4.12(5)
17	1.70(3)	0.589(40)	0.989(67)	4.30(5)
18	1.83(3)	0.626(43)	1.143(79)	4.51(5)
19	1.81(4)	0.620(43)	1.117(77)	4.48(6)
20	1.98(9)	0.665(47)	1.322(94)	4.74(13)
21	2.16(4)	0.711(52)	1.562(114)	5.00(5)
22	2.37(5)	0.761(57)	1.860(138)	5.29(6)

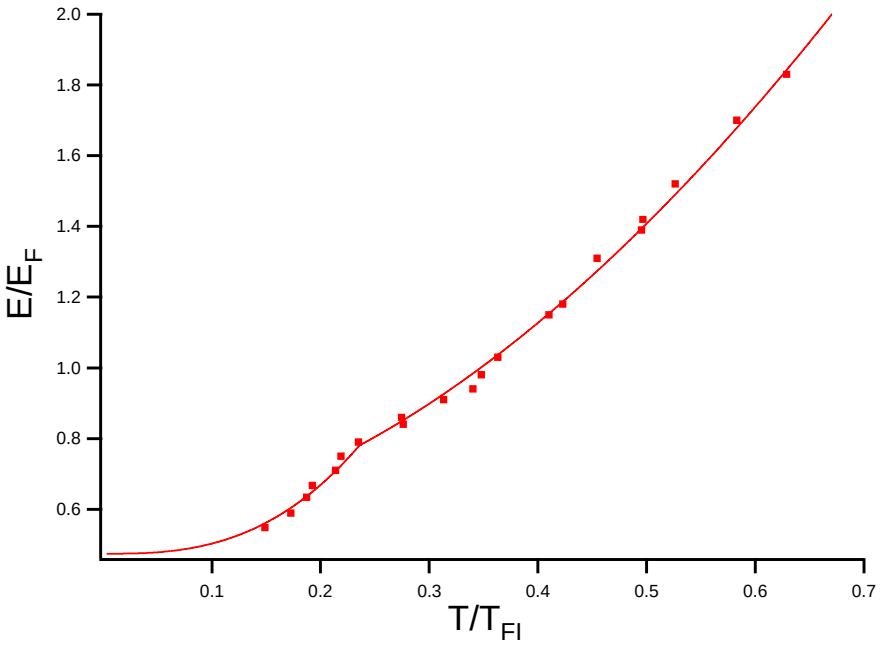

Figure 5.3: Energy E/E_F as a function of the temperature T/T_{FI} for a unitary Fermi gas, using Eq. 5.32 and the fitting parameters listed in Table. 5.4. Red dots are the measured energy versus the temperature obtained from the calibration of Eq. 5.31. E_F is the ideal gas Fermi energy and T_{FI} is the corresponding Fermi temperature.

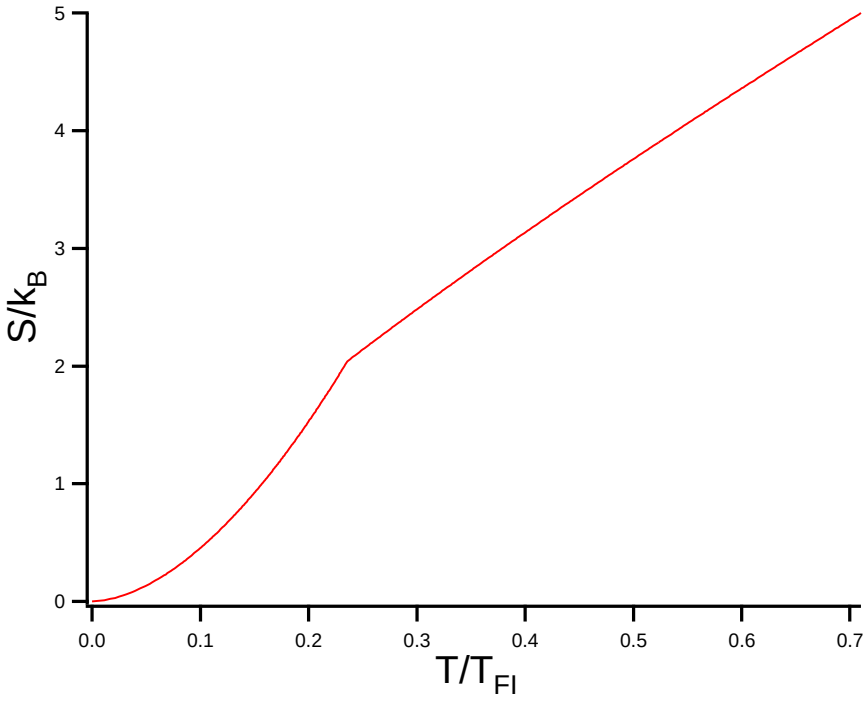

Figure 5.4: Entropy per particle S/k_B as a function of the temperature T/T_{FI} for a unitary Fermi gas, using Eq. 5.33 and the fitting parameters listed in Table. 5.4. E_F is the ideal gas Fermi energy and T_{FI} is the corresponding Fermi temperature. k_B is the Boltzmann constant.

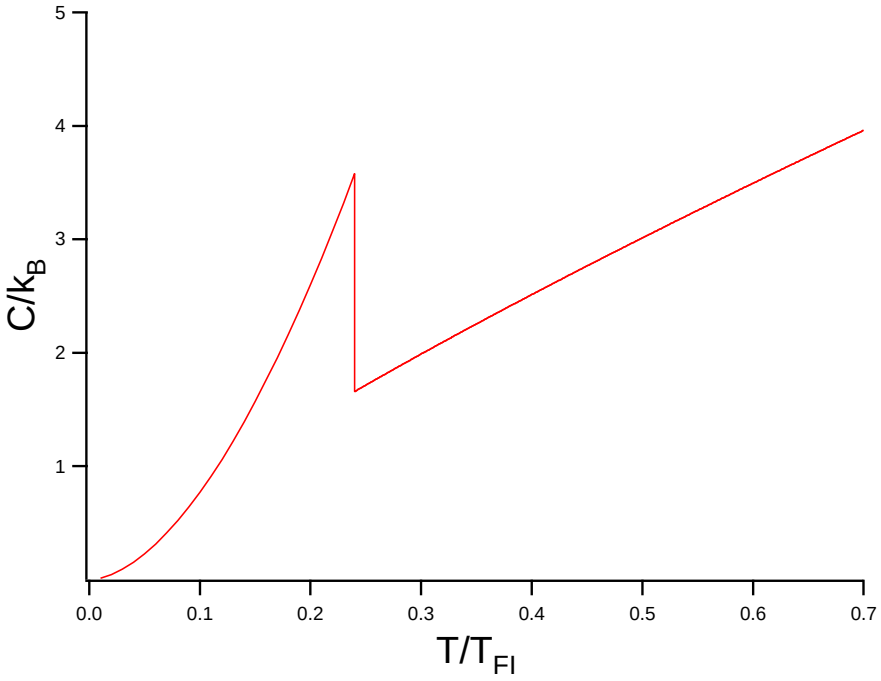

Figure 5.5: Heat capacity in units of k_B as a function of the temperature T/T_{FI} for a unitary Fermi gas, using Eq. 5.34 and the fitting parameters listed in Table. 5.4. E_F is the ideal gas Fermi energy and T_{FI} is the corresponding Fermi temperature. k_B is the Boltzmann constant.

ture [32],

$$\begin{aligned} S_<(T) &= Sc\left(\frac{T}{T_c}\right)^{\frac{1}{b-1}}\ ;\ 0 \le T \le T_c \\ S_>(T) &= Sc\left(\frac{T}{T_c}\right)^{\frac{1}{d-1}}\ ;\ T \ge T_c. \end{aligned} \tag{5.33}$$

The plot of the entropy against the temperature is shown in Fig. 5.4. Note that both the energy and the entropy are continuous at the transition point T_c

The third one is the heat capacity, which is defined as $C = dE/dT$. By virtue of the energy versus temperature Eq. 5.32, we obtain a universal function for the

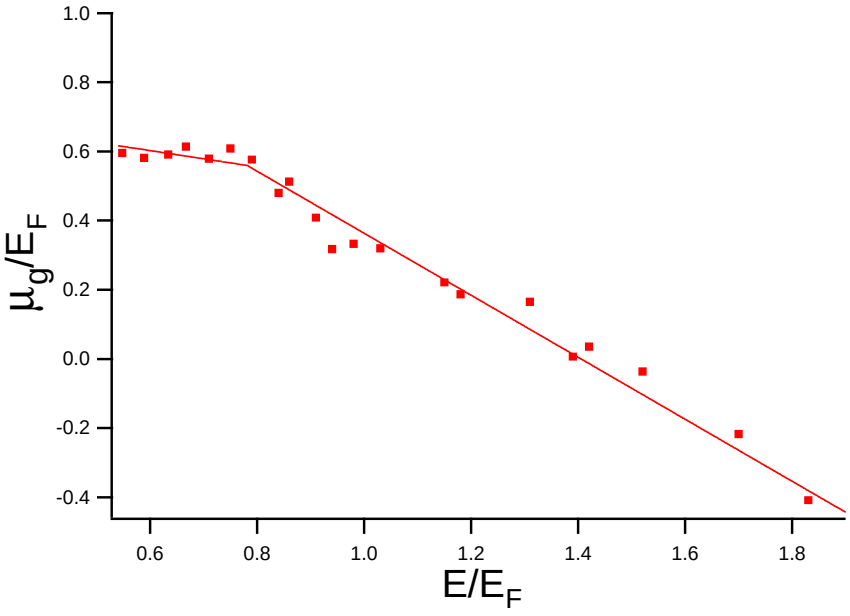

Figure 5.6: The global chemical potential as a function of the energy for a unitary Fermi gas. The data points (red dots) are calculated from the measured E-S data and the fitted T from Eq. 5.31. The red line is the fitted curve from Eq. 5.36 with the fitting parameter listed in Table. 5.4. E_F is the ideal gas Fermi energy

heat capacity [32]

$$\begin{aligned} C_<(T) &= \frac{S_c}{b-1}\left(\frac{T}{T_c}\right)^{\frac{1}{b-1}}; \ 0 \le T \le T_c \\ C_>(T) &= \frac{S_c}{d-1}\left(\frac{T}{T_c}\right)^{\frac{1}{d-1}}; \ T \ge T_c. \end{aligned} \tag{5.34}$$

Note that the heat capacity has a jump at the normal-superfluid transition point due to the construction of the power law fitting curve Eq. 5.31. The heat capacity as a function of the temperature is plotted in Fig. 5.5.

The last universal function is the global chemical potential μ_g. Assuming the local density approximation holds, the global chemical potential for a harmoni-

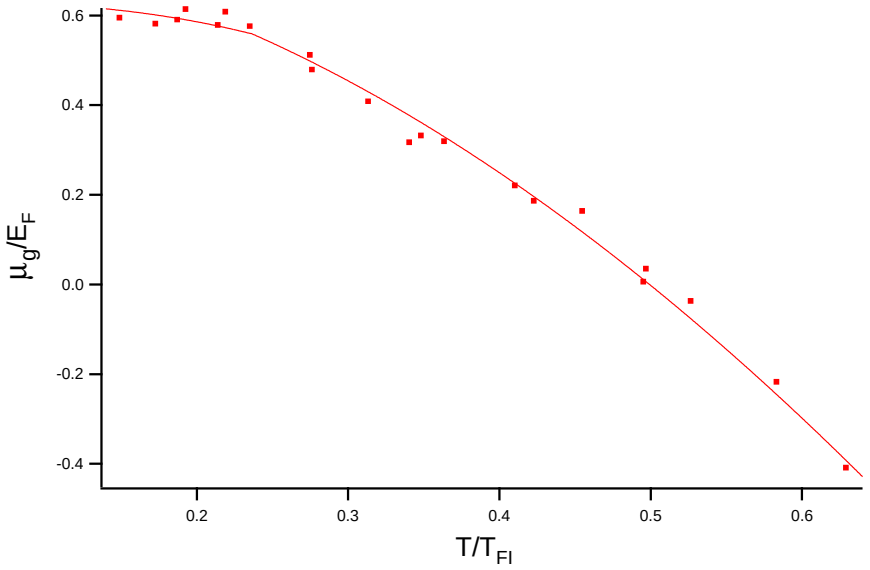

Figure 5.7: The global chemical potential as a function of the temperature for a unitary Fermi gas. The data points (red dots) are calculated from the measured E-S data and the calibrated T from Eq. 5.31. The red line is the curve from Eq. 5.36 with fitting parameter values listed in Table. 5.4.

cally trapped unitary Fermi gas is of the form of

$$\mu_g = \frac{4}{3}E - T\,S. \tag{5.35}$$

The derivation of this equation can be found in Ref. [32]. Using the power law fit with a heat capacity jump Eq. 5.31, the global chemical potential of a harmonically trapped unitary Fermi gas can be calculated from Eq. 5.35 as

$$\begin{aligned} \mu_g(E) &= \frac{4}{3}E_0 + \left(\frac{4}{3} - b\right)(E - E_0);\;\; E_0 \leq E \leq E_c \\ \mu_g(E) &= \mu_g(E_c) + \left(\frac{4}{3} - d\right)(E - E_c);\;\; E \geq E_c, \end{aligned} \tag{5.36}$$

where $\mu_g(E_c) = 4E_0/3 + (4/3 - b)(E_c - E_0)$.

The global chemical potential is plotted against the energy in Fig. 5.6. Using the energy-temperature function Eq. 5.32, we able also able to obtain the global chemical potential as a function of the temperature, as shown in Fig. 5.7

From the four universal functions above, we observe a jump of the heat capacity and the change of the slop of the energy, entropy and global chemical potential, all of which indicate the superfluid-normal fluid transition point. We can better observe the superfluid-normal fluid transition by plotting the energy data from Table. 5.3 relative to the ground state energy E_0 as $E - E_0$ with $E_0 = 0.47$ versus T/T_{FI} and then comparing them to the ideal Fermi gas theory, as shown in Fig. 5.8. The energy $E - E_0$ is plotted as a function of temperature on a ln-ln scale. The change of the slope of the energy temperature curve for a unitary Fermi gas, as compared to that of the ideal Fermi gas theory, reveals the superfluid transition near $T/T_{FI} \sim 0.2$. As expected, the experimental data for the

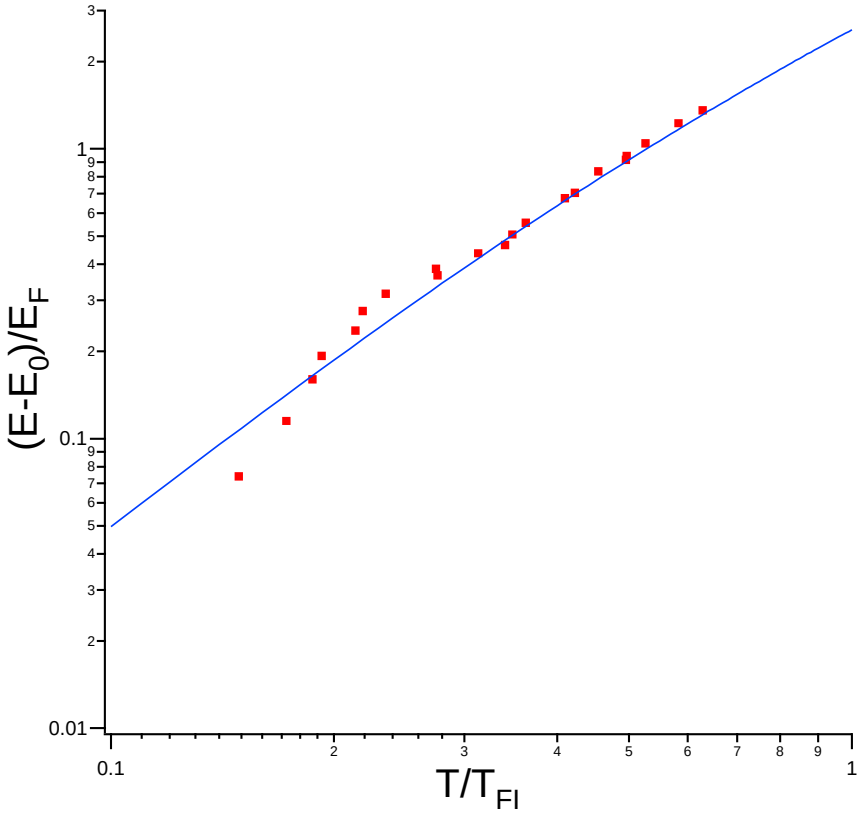

Figure 5.8: Energy versus temperature for a unitary and an ideal Fermi gas plotted on a ln-ln scale. The energy of the a unitary Fermi gas (red dots) is obtained from the cloud dimensions and the temperature is calibrated using the power law fit for a heat capacity jump Eq. 5.31. The energy of the unitary Fermi gas is related to its ground state energy $E = E - E_0$ with $E_0 = 0.47$. The blue curve is the ideal Fermi gas theory. The energy of the ideal Fermi gas is also plotted relative to its ground state energy $E = E - E_0$ with $E_0 = 0.74$.

unitary Fermi gas converges to the ideal Fermi gas value as it approaches the high temperature limit.

Chapter 6

Results of Quantum Viscosity Measurement

Having described the details of the methods for the two hydrodynamic experiments in Chapter 3 and derived the universal hydrodynamic equations Chapter 4, we are now able to present the results of hydrodynamic experiments. To check the applicability of using the hydrodynamic theory for the hydrodynamic experiments, the Knudsen number is estimated in Section 6.1, considering the experimental conditions. Section 6.2 discusses the results of the high temperature anisotropic expansion measurement. We monitor the time evolution of the aspect ratio of the cloud after release from the trap. The viscosity is then extracted as the only free parameter by solving the two universal hydrodynamic equations and fitting the predicted evolution to the experimental data. With the help of energy and temperature calibrations discussed in Chapter 5, we are able to plot the viscosity as a function of the energy and temperature. The predicted high temperature scaling is then demonstrated, which paves the road for the low temperature viscosity measurement. Section 6.3 reports the results of the low temperature radial breathing mode measurements. The damping rate and the cloud size are extracted from the experimental data. The viscosity is then calculated from the damping rate and the cloud size using our universal hydrodynamic

equations. While the energy is calibrated using the same method as that for the high temperature regime, the temperature is determined using a different method at low temperatures, as discussed in Chapter 5. The viscosity is then plotted as a function of the energy and temperature. Section 6.4 shows that the low temperature data joins very smoothly with the high temperature data when the heating is properly included, which enables the measurement of viscosity from nearly the ground state up to the two-body Boltzmann regime. The effect of the bulk viscosity is discussed in Section 6.5. In Section 6.6, we use the measured shear viscosity and previously measured entropy to estimate the ratio of η/s and then compare to the string theory conjecture.

6.1 Knudsen number

As discussed in Chapter 4, the hydrodynamic theory is valid when the mean free path l_{mfp} is much smaller than the characteristic size R of the system that is studied. In other words, the Knudsen number K_n defined in Eq. 4.44 has to be much smaller than unity.

For a unitary Fermi gas, $l_{mfp} \sim 1/(n\bar{\sigma})$, where n is the number density and $\bar{\sigma}$ is the average s-wave cross section. At high temperatures, the thermal de Broglie wavelength $\lambda_T = h/\sqrt{2\pi m k_B T}$ sets the length scale so that $\bar{\sigma} = 4\lambda_T^2$. The density profile at high temperature is well described by a Gaussian distribution, as given by Eq 2.66. We use the central density n_0 to estimate the Knudsen number. Note that $n_0 = N/(\pi^{3/2}\sigma_x\sigma_y\sigma_z)$ for the total number density. For the high temperature

regime, the cloud widths are directly related to the temperature as

$$\frac{3}{2}m\omega_i^2\sigma_i^2 = E = 3k_BT. \tag{6.1}$$

For a cigar-shaped trap, which is used for both of our hydrodynamic experiments, the characteristic cloud size is nominally the radial width $\sigma_\perp \simeq \sigma_x \simeq \sigma_y$. Hence, the Knudsen number can be written as

$$K_n = \frac{l_{mfp}}{R} = \frac{1}{4\lambda_T^2 n_0 \sigma_\perp}. \tag{6.2}$$

Using the definition of the thermal de Broglie wavelength $\lambda_T = h/\sqrt{2\pi m k_B T}$ and the central density $n_0 = N/(\pi^{3/2}\sigma_x\sigma_y\sigma_z)$, Eq. 6.2 yields

$$K_n = \frac{\pi^{1/2}\sigma_z\sigma_\perp m k_B T}{8N\hbar^2}. \tag{6.3}$$

Inserting Eq. 6.1 to Eq. 6.3, one obtains

$$K_n = \frac{\pi^{1/2}k_B^2T^2}{4n\hbar^2\omega_z\omega_\perp}. \tag{6.4}$$

Using $T_{FI} = E_F/k_B = (3N)^{1/3}\hbar(\omega_z\omega_\perp^2)^{1/3}/k_B$, Eq. 6.5 reduces to

$$K_n = \frac{3\pi^{1/2}}{4(3N\lambda_z)^{1/3}}\left(\frac{T}{T_{FI}}\right)^2. \tag{6.5}$$

where $\lambda_z = \omega_z/\omega_\perp$.

As discussed later in this chapter, for the high temperature anisotropic expansion, $N \sim 4 \times 10^5$ and $\lambda_z \sim 0.035$. Using Table. 5.2 for the high temperature anisotropic expansion, we find that the largest $T/T_{FI} \simeq 1.5$. This yields

$K_n \sim 0.09$, which is much smaller than unity.

For our anisotropic expansion, as the cloud expands, both the mean free path l_{mfp} and the characteristic cloud size R decreases because the density drops. However, since the cloud expands very fast in the two traverse directions and stands still in the longitudinal direction, l_{mfp} drops faster than R, yielding a more hydrodynamic system as the cloud expands. We will see this behavior in the following section when we show the results for the anisotropic expansion.

6.2 Anisotropic expansion results

The experimental procedure for the anisotropic expansion has been discussed in Chapter 3. Before we show the experimental results, we need to accurately calibrate the experimental parameters, which is of importance in order to consistently extract viscosity from the hydrodynamic equations. These parameters include the optical trap frequencies ω_i, the full trap depth U_0 and the atom number N.

The trap frequencies, which set the scale for the size and energy of the trapped gas and determine the expansion dynamics, are measured using parametric resonance in both axial and radial directions as discussed in Chapter 3. For the deep optical trap used for the high temperature anisotropic expansion measurements, we obtain $\omega_z = 2\pi \times (182.7 \pm 0.5)$ Hz, $\omega_x = 2\pi \times (5283 \pm 10)$ Hz, $\omega_y = 2\pi \times (5052 \pm 10)$ Hz, and $\bar{\omega} = (\omega_x\omega_y\omega_z)^{1/3} = 2\pi \times (1696 \pm 9)$ Hz [39]. These frequencies are already corrected for anharmoncity. The full trap depth U_0 can be estimated using Eq. 3.14, which yields $U_0 = k_B \times 460\,\mu$K for the deep trap used in our anisotropic expansion [39]. The total number of atoms is determined from the column density of our absorption image, discussed in Section 3.1.7. The

total number of atoms varies with the energy, ranging from $N = 4.0 \times 10^5$ at $E = 2.3\,E_F$ to $N = 6.0 \times 10^5$ at $E = 4.6\,E_F$, where less evaporation is employed. The Fermi energy is $E_F = (3N)^{1/3}\,\hbar\bar{\omega}$. For $N = 6.0 \times 10^5$, E_F is 9.9μK, small compared to the trap depth $U_0 = k_B \times 460\,\mu$K. As we discussed before, this deep trap $U_0 \gg E_F$ permits the use of large energy for the atomic cloud without a large anharmoncity.

Using these system parameters, along with the universal hydrodynamic equations, we are able to extract the viscosity. Section 6.2.1 shows the elliptical flow behavior of the anisotropic expansion, from which we extract the aspect ratio. In Section 6.2.2, we monitor the time evolution of the aspect ratio for different energy points and extract viscosity by solving the universal hydrodynamic equations derived in Chapter 4, using proper initial conditions. Using the energy and temperature calibrations for the high temperature regime discussed in Chapter 5, we show the viscosity as a function of the energy and temperature. The predicted high temperature scaling is then demonstrated in Section 6.2.3 and the effect of the heating is discussed in Section 6.2.4.

6.2.1 Aspect ratio

After conducting the anisotropic expansion experiment discussed in Chapter 3, we obtain two dimensional cloud absorption images for different energy points. A strip of expansion images for a data point at $E/E_F = 2.3$ is shown in Fig. 6.1, which vividly shows that one direction (radial) expands much faster than the other one (axial) in terms of the aspect ratio, as the signature of the elliptical flow. This absorption image contains both thermodynamic and hydrodynamic information for the cloud that can be extracted by fitting a spatial density distribution to the

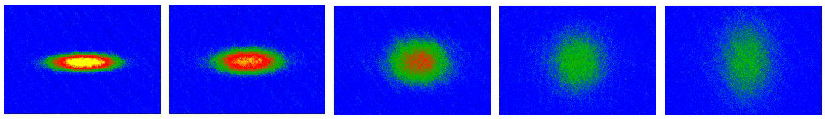

Figure 6.1: Cloud absorption images for 0.2, 0.3, 0.6, 0.9 and 1.2 ms expansion time at $E = 2.3E_F$.

observed profile. As previously discussed, the spatial density distribution varies as the temperature of the cloud changes [70]. Since we are working in the high temperature regime, we fit a two dimensional gaussian distribution to the density profile and obtain the axial width $\sigma_z(t)$ and radial width $\sigma_x(t)$ as a function of time of flight t. The axial and radial widths are plotted against the time-of-flight for the data point at $E/E_F = 3.3$, as shown in Fig. 6.2 and Fig. 6.3, respectively.

These two plots quantitatively demonstrate that the cloud expands much faster, by a much larger factor, in the radial direction than the axial one. What is more useful for us, in extracting viscosity from the hydrodynamic theory, is a simple parameter called the aspect ratio, which is defined as the ratio of the radial width σ_x to the axial width σ_z. The aspect ratio $\sigma_x(t)/\sigma_z(t)$ as a function of the time-of-flight for $E/E_F = 3.3$, corresponding to the data shown in Fig. 6.2 and Fig. 6.3, is plotted in Fig. 6.4. Note that we restrict the maximum time-of-flight to 1.4 ms in order to obtain a high signal-to-background ratio as well as too see the inversion of the aspect ratio.

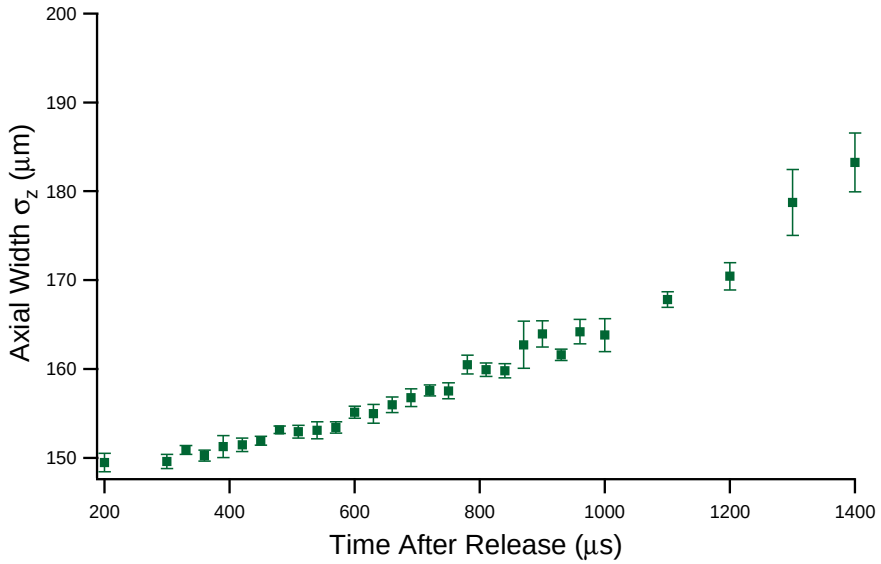

Figure 6.2: The axial width σ_z as a function of time-of-flight. The data was taken at $E = 3.3E_F$. The bars denote statistical errors from the measurement.

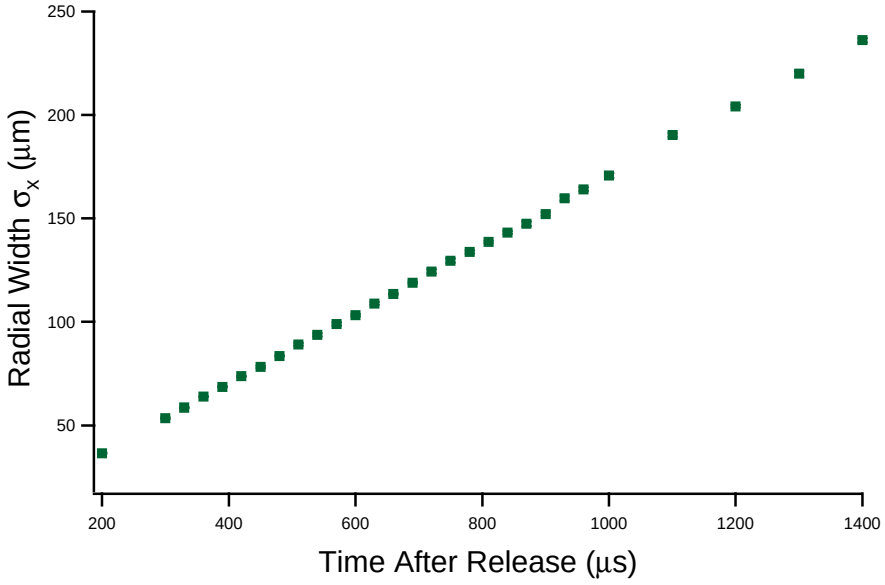

Figure 6.3: The radial width σ_x as a function of time-of-flight. The data was taken at $E = 3.3E_F$. The bars denote statistical errors from the measurement.

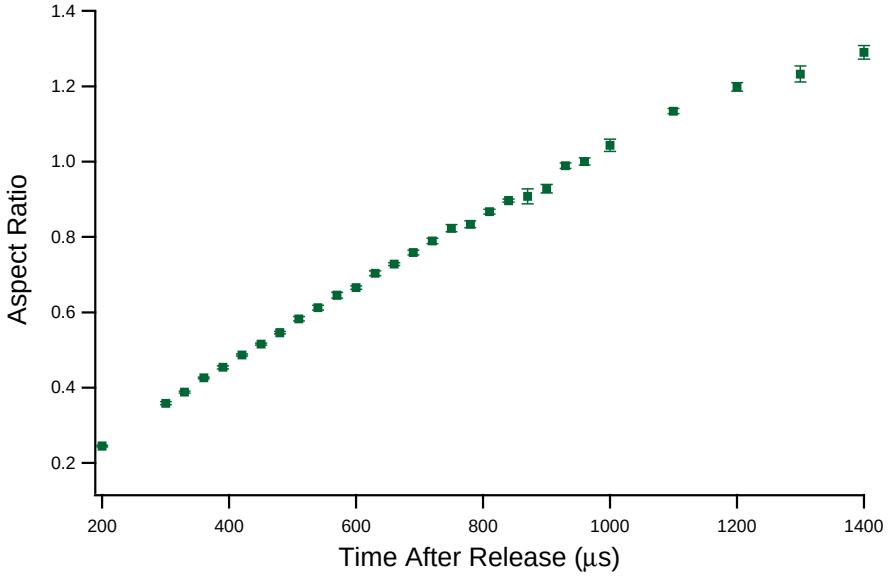

Figure 6.4: Plot of the aspect ratio as a function of the time-of-flight. The data was taken at $E = 3.3E_F$. The bars denote statistical errors from the measurement.

6.2.2 Viscosity versus energy

With the help of the energy calibrations discussed in Chapter 5, we can plot the aspect ratio $\sigma_x(t)/\sigma_z(t)$ as a function of the time-of-flight t for different initial energies, as is shown in Fig. 6.5. Qualitatively, the expansion rate decreases at higher energies as the viscosity increases. In order to quantitatively extract viscosity from the experimental data, we need to solve Eq. 4.58 and Eq. 4.59 with proper initial conditions. Since the cloud is at rest before release, we set $b_i(0) = 1$ and $\dot{b}_i(0) = 0$. The force arising from the scalar pressure is well balanced by the trapping potential before release. Therefore, the initial condition for the force per particle is determined by the trapping potential $a_i(0) = m\omega_i^2$. By solving the universal hydrodynamic equations Eq. 4.58 and Eq. 4.59 with these initial conditions, we determine the ratio $\sigma_x(t)/\sigma_z(t) = (\sigma_x(0)/\sigma_z(0))\,(b_x(t)/b_z(t)) = (\omega_z/\omega_x)\,b_x(t)/b_z(t)$

as a function of time and then compare to the experimental data, yielding very good fits, as shown in Fig. 6.5. Here, the trap-averaged viscosity coefficient $\bar{\alpha}$ is the only free parameter, which is determined by minimizing χ^2. We also find that the friction force produces a curvature that matches the aspect ratio versus time data very well. The black curve in Fig. 6.5 is the solution to the ideal hydrodynamics with no free parameter fit. The fact that it fits the nearly ground state data ($E/E_F = 0.6$) very well shows that the trap frequencies are accurately measured using parametric resonance.

As discussed above, the system becomes more and more hydrodynamic as the cloud expands as a consequence of elliptical flow . Shown in Fig. 6.5, the green dashed line is the theoretical prediction of a ballistic expansion using Eq. 4.45 with the same trap conditions. The cloud expands ballistically at the very beginning (red, blue and pink data overlapping with the green ballistic curve) and becomes more and more hydrodynamic (red, blue and pink data departing from the green ballistic curve). Hence, we believe that, even though we are working in the high temperature regime, the hydrodynamic description is valid and viscosity is well defined for the expansion time scales we study.

The trap-averaged viscosity coefficient $\bar{\alpha}$ as a function of E/E_F in the high temperature regime is displayed in Fig. 6.6. We observe $\bar{\alpha}$ changes by a factor of 8 as the energy varies by approximately a factor 2.

6.2.3 High temperature universal scaling

As discussed in Chapter 1, shear viscosity has a universal temperature scaling Eq. 1.4 for the high temperature regime. Although it was derived using a variety of theory, this high temperature universal scaling has not been demonstrated until

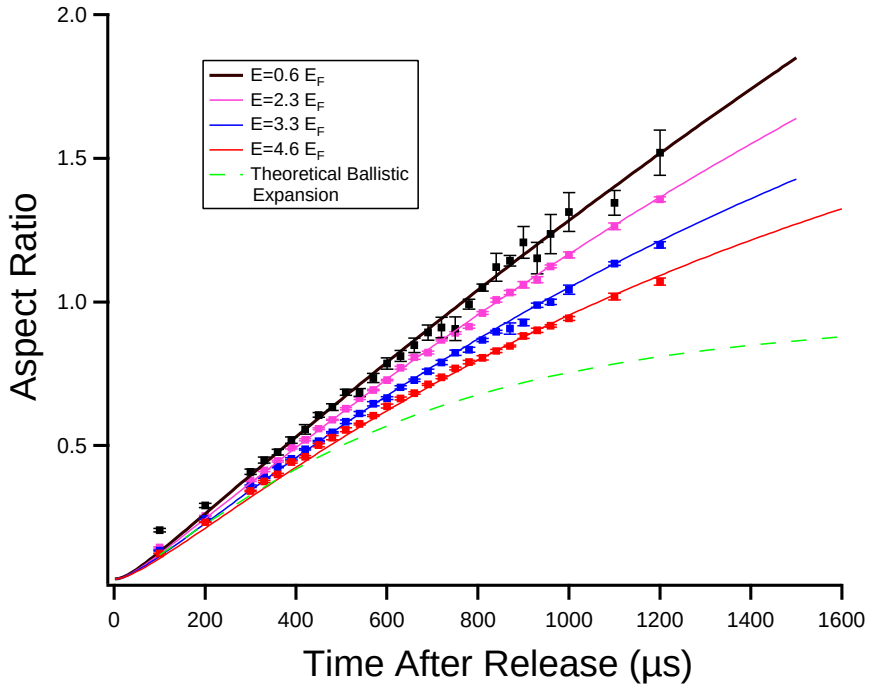

Figure 6.5: Aspect ratio versus expansion time for different energies $E = 0.6E_F$, $E = 2.3E_F$, $E = 3.3E_F$ and $E = 4.6E_F$. Black curve is solution to the perfect hydrodynamic equations with no free parameter. Pink, blue and red curves are fitted curves for $E = 2.3E_F$, $E = 3.3E_F$ and $E = 4.6E_F$, using the shear viscosity as the only free parameter. Error bars denote statistical fluctuations in the aspect ratio. The green dashed line is the theocratical ballistic expansion curve from Eq. 4.45 with the same trap conditions as the anisotropic hydrodynamic expansion.

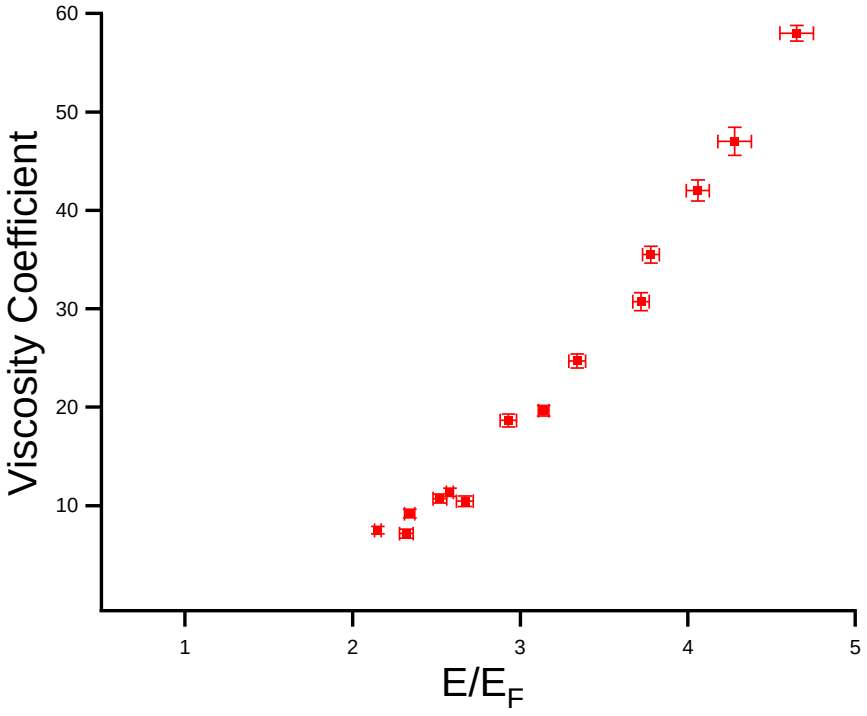

Figure 6.6: The trap-averaged viscosity coefficient as a function of energy in the high temperature regime. Bars denote statistical arising from the uncertainty in cloud size and $\bar{\alpha}$.

a major breakthrough in the recent viscosity measurements from our group [39]. The perfect $T^{3/2}$ is observed and the coefficient is found to be in a very good agreement with the predicted value. By demonstrating this high temperature scaling, we have shown that the observed slowdown of the anisotropic expansion is due to viscosity, instead of some specious effects. Hence, this high temperature scaling stands as a benchmark to measure viscosity at low temperatures. Following our work, later spin transport measurements [92] explored the predicted high temperature scaling before the low temperature regime was studied.

To demonstrate this high temperature universal scaling of viscosity, we need to use the measured trap-averaged viscosity coefficient $\bar{\alpha}$ above and the temperature calibration from the second virial approximation Eq. 5.11 in Chapter 5. However, the reduced temperature given by Eq. 5.11 is a local quantity. Hence, we need a corresponding local viscosity coefficient to test the high temperature scaling. As discussed before, the trap-averaged viscosity Eq. 4.56 is well defined, since $\eta \to 0$ as the density goes to zero at the dilute cloud edges [47]. Thus, we can expect that $\bar{\alpha}$ is dominated by the hydrodynamic region near the cloud center, $\bar{\alpha} \simeq \alpha_0$, where the viscosity at the trap center is $\eta_0 = \alpha_0 \hbar n_0$. Hence, at high temperatures, we can write the viscosity coefficient at the trap center α_0 as [36]

$$\alpha_0 = \alpha_{3/2} \theta_0^{3/2}, \tag{6.6}$$

where $\theta_0 = T/T_F(n_0)$ is the local reduced temperature at the trap center and $\alpha_{3/2}$ is a universal coefficient that can be determined by fitting this function to our high temperature data.

As discussed before, in the zeroth-order adiabatic approximation, Eq. 4.28

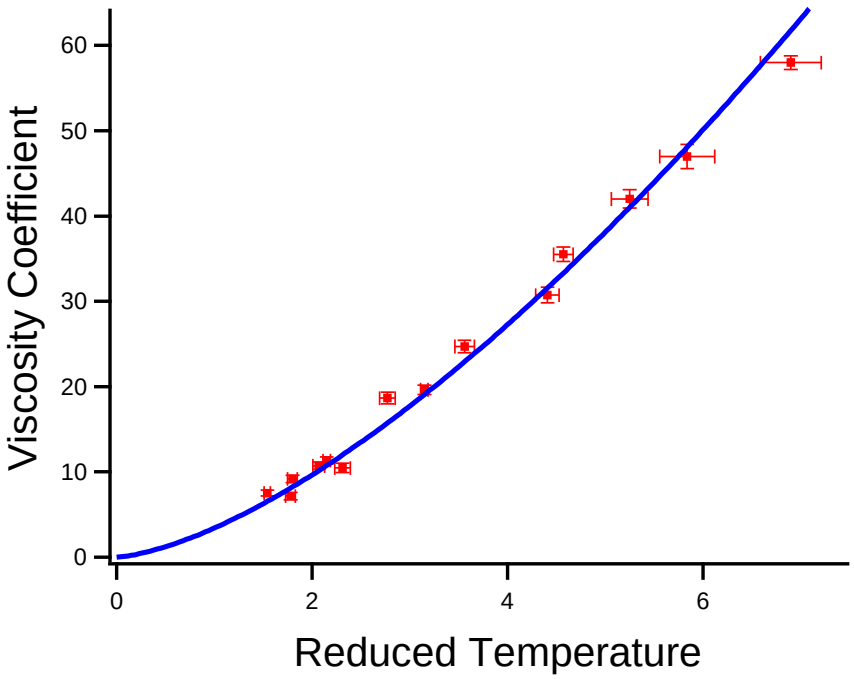

Figure 6.7: Trap-averaged viscosity coefficient $\bar{\alpha} = \int d^3\mathbf{x}\eta/(\hbar N)$ versus reduced temperature θ_0 at the trap center before release of the cloud. The blue curve shows the fit $\alpha_0 = \alpha_{3/2}\theta_0^{3/2}$, demonstrating the predicted universal high-temperature scaling $\eta \propto T^{3/2}$. Bars denote statistical error arising from the uncertainty in θ_0 and $\bar{\alpha}$.

requires that the local reduced temperature θ has a zero convective derivative everywhere and the local reduced temperature at the trap center θ_0 has a zero time derivative. As a result, $\bar{\alpha}$ as well as α_0 is constant. Table. 6.1 gives the energy, local reduced temperature and trap-averaged viscosity coefficient. The universal high temperature scaling is demonstrated in Fig. 6.7, where the fit gives $\alpha_{3/2} = 3.4(0.03)$. A tiny statistical error 0.03 confirms the perfect $T^{3/2}$ scaling. The fitted $\alpha_{3/2}$ is close to the predicted value $\alpha_{3/2} = 45\pi^{3/2}/(64\sqrt{2}) = 2.77$ using a variational calculation for a Fermi gas in a 50-50 mixture of two spin states [36]. We expect that this $\alpha_{3/2}$ would decrease if the really local viscosity is used instead

Table 6.1: Energy, temperature and viscosity coefficient inn the high temperature regime. Energy E/E_F, temperature normalized by an ideal Fermi gas temperature T/T_{FI}, local reduced temperature at the trap center for a unitary Fermi gas $T/T_F(n_0)$ and trap-averaged viscosity coefficient $\bar{\alpha}$ in the high temperature regime obtained from the anisotropic expansion experiment.

	E/E_F	T/T_{FI}	$T/T_F(n)$	$\bar{\alpha}$
1	2.15(2)	0.770(6)	1.54(3)	7.49(36)
2	2.32(4)	0.815(9)	1.78(5)	7.14(46)
3	2.34(4)	0.820(9)	1.80(5)	9.17(44)
4	2.52(4)	0.874(12)	2.07(6)	10.71(46)
5	2.58(2)	0.891(7)	2.15(4)	11.34(41)
6	2.67(5)	0.917(13)	2.31(8)	10.45(55)
7	2.93(5)	0.995(12)	2.77(8)	18.64(66)
8	3.14(3)	1.060(8)	3.15(4)	19.63(54)
9	3.34(5)	1.120(12)	3.56(10)	24.69(72)
10	3.72(5)	1.240(13)	4.41(12)	30.73(91)
11	3.78(5)	1.250(12)	4.57(10)	35.50(85)
12	4.06(7)	1.340(15)	5.25(19)	42.00(108)
13	4.28(10)	1.41(20)	5.84(28)	47.00(143)
14	4.65(10)	1.53(20)	6.90(31)	58.00(80)

of making $\bar{\alpha} \simeq \alpha_0$ assumption. An estimate based on the relaxation model [60] shows that $\bar{\alpha} = 1.3\alpha_0$ at high T, yielding $\alpha_{3/2} = 2.6$, which is in better agreement with the predicted value $\alpha_{3/2} = 2.77$ [36].

6.2.4 Effect of heating in the anisotropic expansion

As shown in our universal hydrodynamic equations, friction forces generate energy dissipation in the form of heat. For the anisotropic expansion experiment, the effect of the heating needs careful discussion.

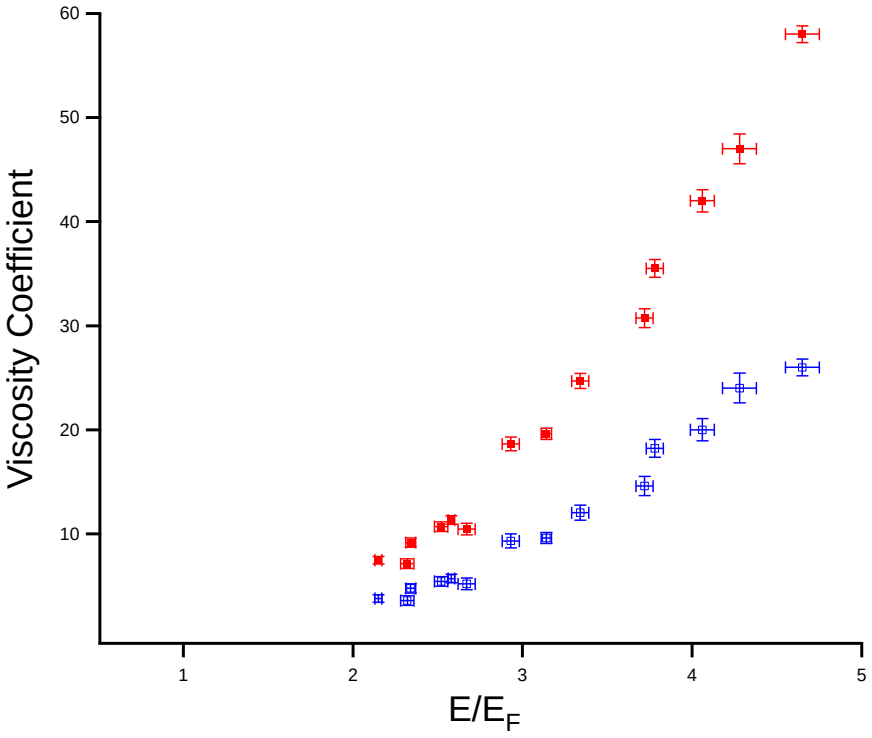

Figure 6.8: Effect of the heating rate in Eq. 4.43 on the measured viscosity coefficient $\bar{\alpha}$ versus initial energy per atom at high temperature using anisotropic expansion experiments. Red solid circles/blue open squares: heating is included/excluded. Bars denote errors arising from the uncertainty in E and the cloud dimensions.

Let's begin by considering the ideal hydrodynamic case. After release from the trap, the cloud expands and therefore gains kinetic energy. Since there is no energy dissipation and the total energy is conserved, the newly earned kinetic energy comes from the internal energy of the cloud. If viscous forces are taken into account, part of the kinetic energy is converted into heating during expansion. Where can the heat go? It cannot be absorbed by a huge heat reservoir, since the cloud is isolated. By the numerical simulation [43] and our hydrodynamic theory, it is shown that the heat actually goes back to the cloud, resulting in an increase of the internal energy density $\mathcal{E}$ and hence the pressure $P = 2/3\mathcal{E}$ as compared to the ideal case. The increase in pressure P leads to the acceleration relative to that obtained by neglecting the heating. Hence, a larger viscosity is needed to balance the acceleration caused by heating. Put simply, the effect of the heating leads to reacceleration of the cloud and therefore increase the shear viscosity.

Fig. 6.8 demonstrates the effect of heating for the anisotropic expansion. The trap-averaged viscosity coefficient measured without heating is reduced by a factor of 2 compared to that obtained when heating is included. Hence, the heating plays a significant role throughout the hydrodynamic expansion for our anisotropic expansion experiment.

6.3 Radial Breathing mode results

The demonstration of the high temperature scaling provides a benchmark for measuring viscosity. However, what interests us most is the low temperature regime where richer physics appears, i.e., pair formation and superfluidity. We now come back to the raw radial breathing mode data taken in 2004 [41]. Those

data were used as the first evidence for superfluidity [41] and to estimate trap-averaged viscosity [38]. However, since the high temperature scaling had not been demonstrated, we could not even prove that we were measuring viscosity. Further, we did not understand the effect of heating at that time. Now we have demonstrated the high temperature scaling and we also have a consistent and accurate method of calibrating energy and temperature as discussed in Chapter 5. Hence, we can consistently and accurately the viscosity by reanalyzing the raw radial breathing mode data and then joining them with the high temperature data. In Section 6.3.1, the damping rate is extracted by fitting an exponentially damped sinusoid to the experimental data, which is simply related to the viscosity and the measured cloud size. In Section 6.3.2, we self consistently obtain the trap-averaged viscosity from the damping rate and cloud dimension using the universal hydrodynamic equations. Hence, the viscosity is determined as a function of the energy. Section 6.3.3 shows that heating, in contrast to the high temperature anisotropic expansion, is negligible for the low temperature breathing mode.

To obtain the results, we need to calibrate and measure the system parameters . The optical trap frequencies are measured using parametric resonance in Ref. [41], yielding $\omega_\perp = \sqrt{\omega_x \omega_y} = 2\pi \times 1696(10)$ Hz, $\omega_x/\omega_y = 1.107(4)$, and $\omega_z = 2\pi \times 71(3)$ Hz [41]. Hence, $\bar{\omega} = (\omega_x \omega_y \omega_z)^{1/3} = 2\pi \times 589(5)$ Hz is the mean oscillation frequency. The total number of atoms is $N \simeq 2.0 \times 10^5$ and the typical Fermi temperature $T_F = (3N)^{1/3}\hbar\bar{\omega}/k_B$ of a corresponding noninteracting gas is $\simeq 2.4\,\mu$K, and the trap depth is $U_0/k_B = 35\,\mu$K [41].

6.3.1 Damping rate

While the aspect ratio is extracted from the anisotropic expansion to measure viscosity in the high temperature regime, the radial breathing mode experiment, as discussed in Chapter 4, focuses on the damping rate of the oscillating atomic cloud that is directly related to the trap-averaged viscosity coefficient $\bar{\alpha}$ through Eq. 4.70. We extract the cloud width as a function of t_{hold} by fitting a Gaussian distribution to the cloud density profile, which is sufficiently accurate except for the very lowest temperature points where the cloud profile has a zero-temperature Thomas-Fermi distribution. The damping rate $1/\tau$ as well as the oscillation frequency ω_0 can be both obtained by fitting an exponentially damped sinusoid to the breathing oscillation data

$$\sigma(t) = \sigma_0 + A \exp(-t/\tau) \sin(\omega_0 t + \phi) \tag{6.7}$$

where A is the oscillation amplitude and ϕ is the phase angle. τ and ω_0 are the damping time and the oscillation frequency, respectively.

Fig. 6.9 shows the cloud width versus time for a radial breathing mode at $E/E_F = 1$. The transverse width of the cloud is plotted as a function of t_{hold}. Fitting an exponentially damped sinusoid Eq 6.7 to the data yields $\tau = 1.45$ ms and $\omega_B = 2\pi \times 3038$ Hz.

Since the virial theorem also holds for the low temperature regime, we are able to calculate the initial energy per particle from the initial cloud dimensions. Fig. 6.10 shows the damping rate $1/\tau$ normalized by the transverse trap frequency $\omega_\perp$ as a function of energy E/E_F. There is a very interesting plateau observed at the higher temperatures of this breathing mode data [38, 41], which shows that

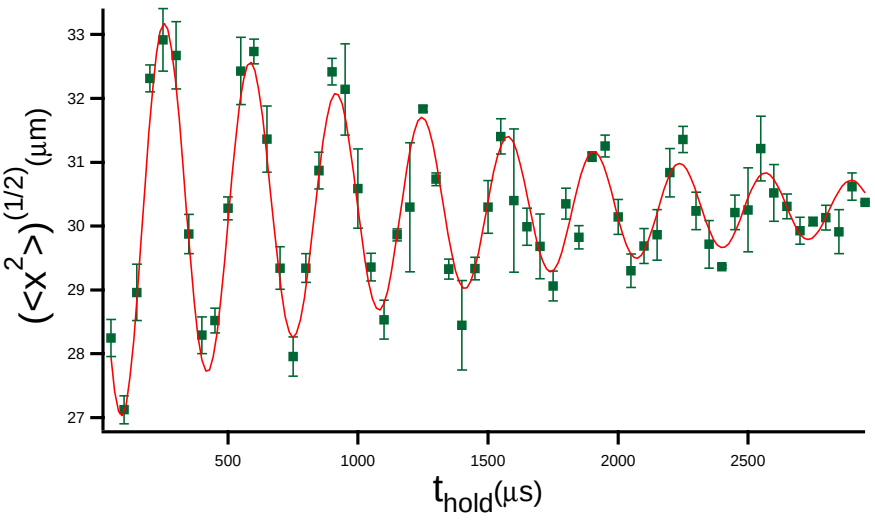

Figure 6.9: Excitation of a radial breathing mode for a unitary Fermi gas at $E/E_F = 1$. The red curve is a damped sinusoid fit to the data which gives damping time $\tau = 1.45$ms. Bars denote statistical errors on measuring the size of the cloud.

the trap-averaged viscosity coefficient $\bar{\alpha}$ prefers a term $\propto E$ in this temperature regime, since $1/\tau \propto \bar{\alpha}/E$ according to Eq. 4.70. This flattening is reflected in the temperature scaling that will be discussed in Section 6.4.

6.3.2 Viscosity versus energy

As we see from Eq. 4.70, the initial transverse cloud size $\langle x^2 \rangle_0$ and the damping rate are both needed to obtain the trap-averaged viscosity $\bar{\alpha}$. The damping rate $1/\tau$ is obtained by fitting a damped sinusoid to the data as discussed above. The transverse mean square size of the trapped cloud before excitation is given by the scale transformation $\langle x^2 \rangle_0 = \langle x^2 \rangle / b_x^2(t)$, where $\langle x^2 \rangle$ is determined by imaging at a time t after the cloud is released and $b_x(t)$ is the calculated hydrodynamic expansion factor including viscosity. For the radial breathing mode, we use time-

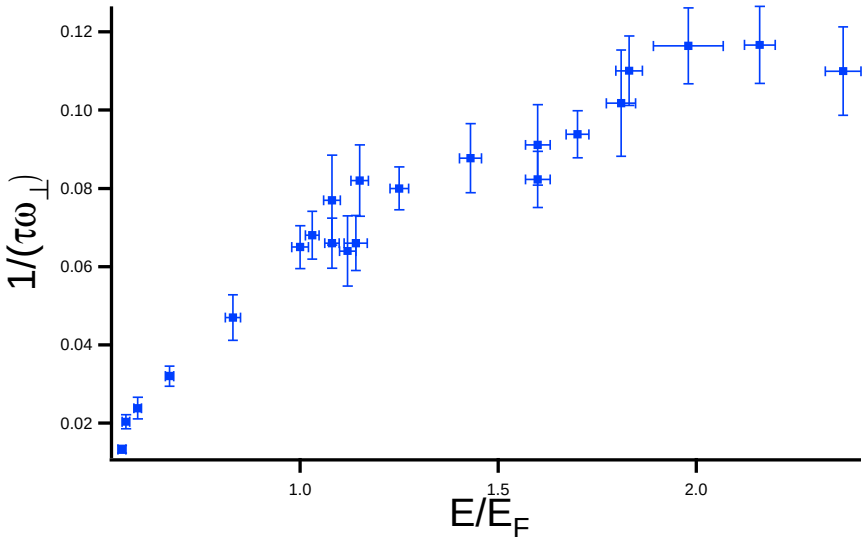

Figure 6.10: Energy dependence of the damping rate for the radial breathing mode. Bars denote statistical error arising from the uncertainty in the damping time τ, trap frequency $\omega_\perp$ and the cloud size.

of-flight $t = 1$ms. We self-consistently determine $b_x(t)$ and $\bar{\alpha}$ from the fitted damping rate $1/\tau$ and the measured cloud size after expansion, using Eq. 4.70 as a constraint. Since the viscosity is small at low temperatures, we obtain an initial estimate for $\langle x^2 \rangle_0$ by calculating $b_x(t)$ for zero viscosity. This yields an initial approximation for $\langle x^2 \rangle_0$ as well as $\bar{\alpha}$. These initial values are then used in Eqs. 4.60 and 4.61 (with the trap term $\omega_i^2 = 0$ and including the heating rate) to determine a better approximation to $b_x(t)$, which in turn yields a better value for $\langle x^2 \rangle_0$ and $\bar{\alpha}$. This procedure is easily repeated and quickly converges, yielding an optimal value for $\bar{\alpha}$ as well as $\langle x^2 \rangle_0$. $\langle x^2 \rangle_0$ is used to determine the initial energy, as discussed in Chapter 5. The fitted trap-averaged viscosity coefficient $\bar{\alpha}$ is plotted as a function of energy in Fig. 6.11. Table. 6.2 gives the energy, local reduced temperature and trap-averaged viscosity coefficient for the low temperature measurements.

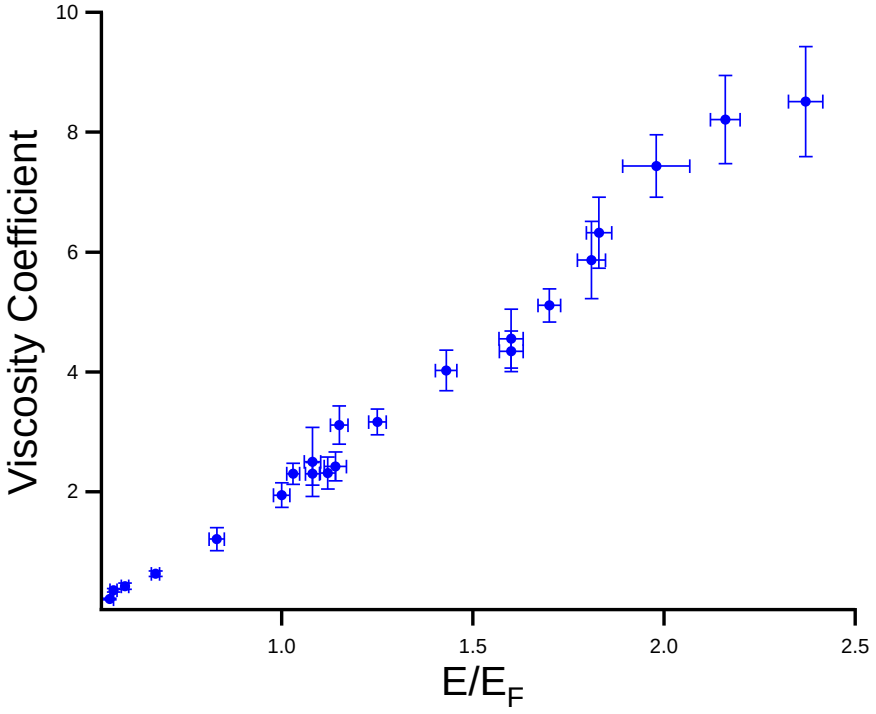

Figure 6.11: Energy dependence of the trap-averaged viscosity coefficient $\bar{\alpha}$ for the low temperature regime. Bars denote statistical error arising from the uncertainty in the damping time τ, trap frequency $\omega_\perp$ and the cloud size.

Table 6.2: Energy E/E_F, local reduced temperature at the trap center for an ideal Fermi gas T/T_{FI}, local reduced temperature at the trap center for a unitary Fermi gas $T/T_F(n)$ and trap-averaged viscosity coefficient $\bar{\alpha}$ in the low temperature regime using the radial breathing mode experiment.

	E/E_F	T/T_{FI}	$T/T_F(n)$	$\bar{\alpha}$
1	0.55(1)	0.142(20)	0.072(10)	0.21(2)
2	0.56(1)	0.149(22)	0.078(12)	0.36(3)
3	0.59(1)	0.166(27)	0.092(15)	0.42(5)
4	0.67(1)	0.200(33)	0.126(21)	0.63(4)
5	0.83(2)	0.264(6)	0.208(5)	1.21(20)
6	1.00(2)	0.347(15)	0.331(15)	1.94(21)
7	1.03(2)	0.360(17)	0.354(16)	2.30(18)
8	1.08(2)	0.381(19)	0.395(20)	2.50(58)
9	1.08(2)	0.381(19)	0.393(20)	2.30(19)
10	1.12(2)	0.397(20)	0.428(22)	2.31(27)
11	1.14(3)	0.405(21)	0.445(23)	2.42(24)
12	1.15(2)	0.409(21)	0.453(24)	3.11(32)
13	1.25(2)	0.446(26)	0.539(31)	3.17(21)
14	1.43(3)	0.507(32)	0.704(44)	4.02(34)
15	1.60(3)	0.560(37)	0.879(58)	4.34(34)
16	1.60(3)	0.560(37)	0.881(58)	4.56(49)
17	1.70(3)	0.589(40)	0.989(67)	5.11(28)
18	1.83(3)	0.626(43)	1.143(79)	6.32(59)
19	1.81(4)	0.620(43)	1.117(77)	5.87(65)
20	1.98(9)	0.665(47)	1.322(94)	7.43(52)
21	2.16(4)	0.711(52)	1.562(114)	8.21(74)
22	2.37(5)	0.761(57)	1.860(138)	8.51(92)

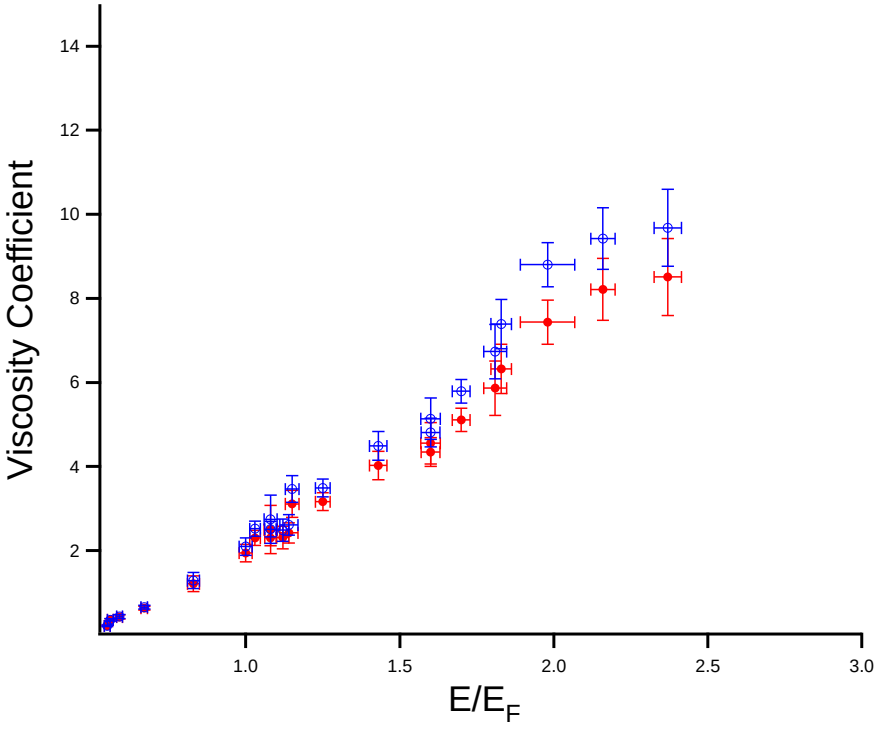

Figure 6.12: Effect of the heating rate in Eq. 4.43 on the measured viscosity coefficient $\bar{\alpha}$ versus initial energy per atom at low temperatures using breathing mode experiments. Red solid circles/blue open squares: heating is included/excluded. Bars denote errors arising from the uncertainty in E and the cloud dimensions.

6.3.3 Effect of heating in the radial breathing mode

The heating plays an important role in the high temperature anisotropic expansion through reaccelerating the cloud and causing a factor of ~ 2 difference, as shown in Fig. 6.8. However, the heating arising from friction force is negligible for the low temperature breathing mode. As explained before, the heating term contains $\sigma_{ij}^2 \propto \dot{\epsilon}_i^2$ and $\epsilon_i \ll 1$ is much smaller than unity because the breathing mode oscillation amplitude is very small compared to the original size of the cloud. As a result, the heating hardly affects the extraction of $\bar{\alpha}$ from our data. Fig. 6.12 shows the effect of heating for the radial breathing mode experiment.

Note that even though heating term is not included in our universal hydrodynamic equations for the breathing oscillation, it still affects the self-consistent determinations of $b_i(t)$ and $\langle x^2 \rangle_0$ because they are both determined by the expansion dynamics of the cloud. This expansion dynamics is governed by Eq. 4.58 and Eq. 4.59, which actually care about heating. This is why Fig. 6.12 shows that $\bar{\alpha}$ slightly differs when heating is included compared to when heating is excluded. This difference decreases with temperature and finally disappears when the ground state is approached, since negligible viscosity near the ground state causes negligible heating.

6.4 Viscosity in the whole regime

Having found the trap-averaged viscosity for the high and low temperature hydrodynamic experiments, we are interested in combining them together. Section 6.4.1 discusses the viscosity versus energy for the whole regime and Section 6.4.2 studies the viscosity versus temperature for the whole regime.

6.4.1 Viscosity versus energy

By combining Fig. 6.6 and Fig. 6.11, we obtain Fig. 6.13, which shows a smooth joining of the trap-averaged viscosity coefficient $\bar{\alpha}$ as a function of initial energy E/E_F. Hence we are able to determine the viscosity coefficient from nearly the ground state to the two-body Boltzmann regime.

As discussed before, the high temperature measurements demonstrate the predicted viscosity-temperature scaling, which sets a benchmark for the low temperature measurements. The smooth joining between high and low temperature mea-

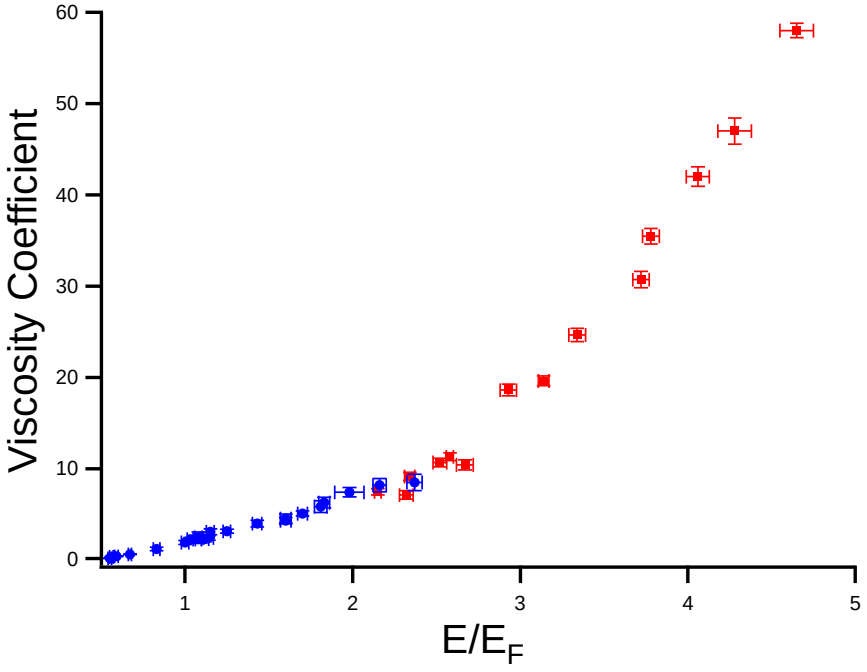

Figure 6.13: Trap-averaged viscosity coefficient $\bar{\alpha} = \int d^3\mathbf{x}\, \eta/(\hbar N)$ versus initial energy per atom. Blue circles: Breathing mode measurements; Red squares: Anisotropic expansion measurements. Bars denote statistical error arising from the uncertainty in E and the cloud dimensions.

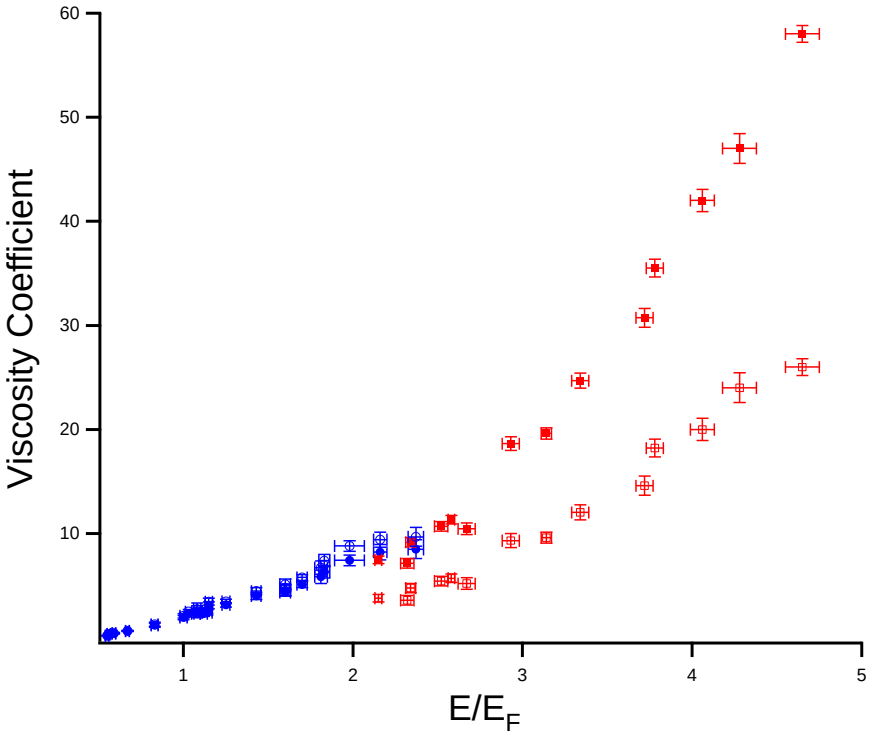

Figure 6.14: Effect of the heating rate in Eq. 4.43 on the measured viscosity coefficient $\bar{\alpha}$ versus initial energy per atom. Solid(open) circles/squares: heating is included(excluded). Blue circles: low energy breathing mode data; Red squares: high energy expansion data. The high and low temperature data smoothly join only when heating is included. Bars denote errors arising from the uncertainty in E and the cloud dimensions.

surements shows that the universal hydrodynamic equations correctly describe the experiments and that the damping of the radial breathing mode experiments is due to the viscosity rather than some other special effects.

Heating plays very different roles in these two experiments, as discussed individually for each experiment above. By combing Fig. 6.8 and Fig. 6.12, we find a very good agreement between these two very different hydrodynamic measurements when the heating is properly included, as seen in Fig. 6.14. Ignoring the heating effect results in a huge discontinuity between these two experiments.

6.4.2 Viscosity versus reduced temperature

While the high temperature scaling is demonstrated, we are interested in extending this temperature scaling to a wider range. Using the temperature calibrations for different temperature regimes, as discussed in Chapter 5, we display the trap-averaged viscosity as a function of the local reduced temperature from nearly the ground state up to the two-body Boltzmann regime, as shown in Fig. 6.15. We can compare our experimental results to the recent theoretical calculations on the local viscosity from Ref. [54], as shown in Fig. 6.16. Both the experimental data and the theoretical calculations are found to scale as $T^{3/2}$ in the high temperature regime, consistent with Eq. 6.6. However, we observe that the damping rate of the radial breathing mode reaches a plateau at the higher temperatures [38, 41], as shown in Fig. 6.9. This flattening can be explained if $\bar{\alpha}$ has a term $\propto E$, since $1/\tau \propto \bar{\alpha}/E$, according to Eq. 4.70. Since $\theta_0^{1/2} \propto E$ at higher temperatures, we fit the data of Fig. 6.15 with the two-parameter fit function,

$$\bar{\alpha} = \bar{\alpha}_{3/2}\,\theta_0^{3/2} + \bar{\alpha}_{1/2}\,\theta_0^{1/2}, \tag{6.8}$$

where $\bar{\alpha}$ is the trap averaged viscosity and θ_0 is the local reduced temperature at the trap center. Fitting all of the data for the normal fluid regime ($E > 0.7\,E_F$), we find $\bar{\alpha}_{3/2} = 2.96(3)$ and $\bar{\alpha}_{1/2} = 1.87(8)$, where the errors are statistical from the fit. In this case, $\bar{\alpha}_{3/2} = 2.96$ is closer to the local value predicted for the high temperature two-body unitary regime, where $\alpha_{3/2} = 2.77$.

We can also use the same two-parameter fit for the predicted local viscosity

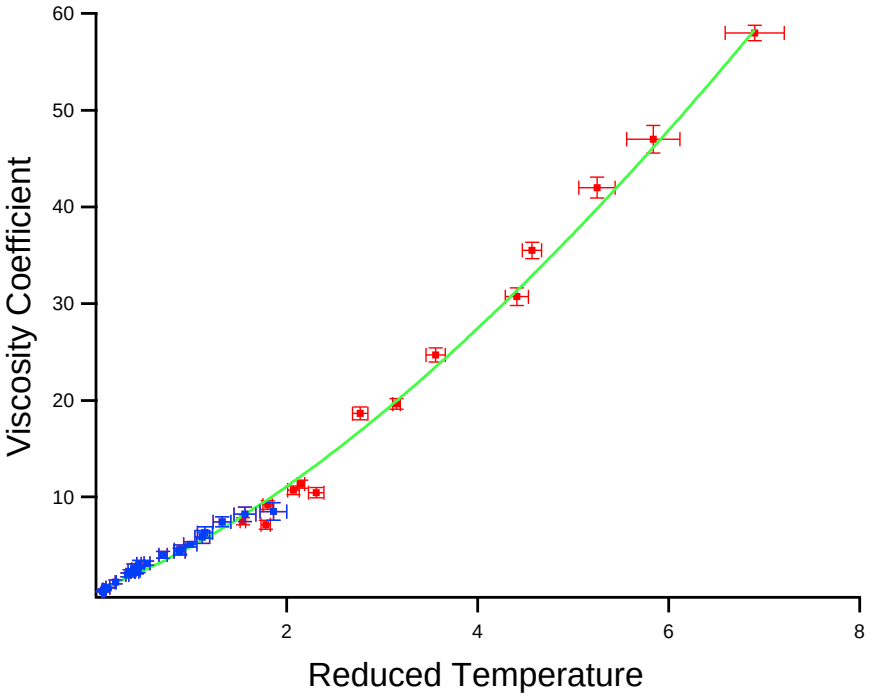

Figure 6.15: Trap-averaged viscosity coefficient $\bar{\alpha} = \int d^3\mathbf{x}\,\eta/(\hbar N)$ versus reduced temperature $\theta_0 = T_0/T_F(n_0)$ at the trap center, prior to release. Blue dots: Breathing mode measurements; Red dots: Anisotropic expansion measurements. Bars denote statistical errors arising from the uncertainty in $\bar{\alpha}$, E and the cloud dimensions. The green curve shows the fit $\bar{\alpha} = \bar{\alpha}_{3/2}\,\theta_0^{3/2} + \bar{\alpha}_{1/2}\,\theta_0^{1/2}$ with $\bar{\alpha}_{3/2} = 2.96(3)$ and $\bar{\alpha}_{1/2} = 1.87(8)$, for the temperature from nearly the superfluid transition point up to the two-body unitary regime.

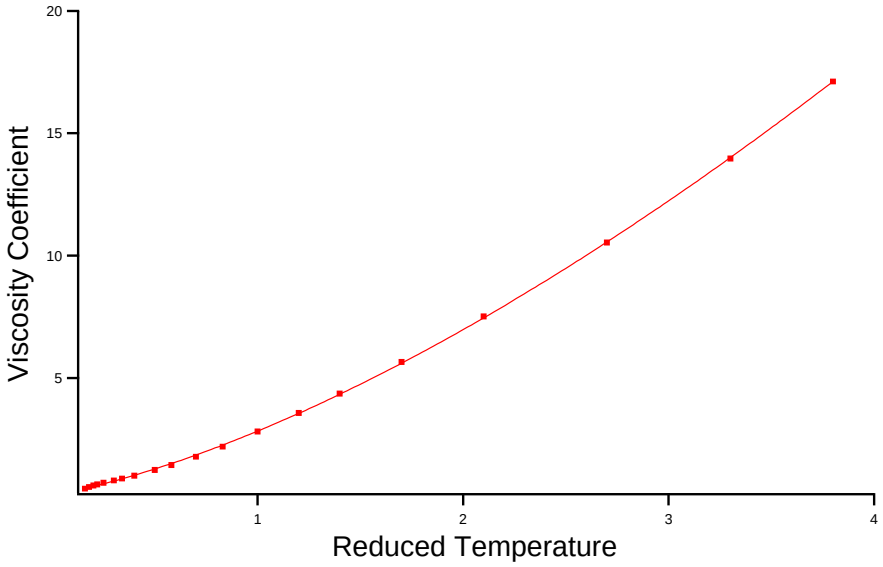

Figure 6.16: The theoretical prediction for the local shear viscosity α in the normal fluid phase versus the local reduced temperature $\theta = T/T_F(n)$ from Ref. [54]. The red curve shows the fit $\alpha = \alpha_{3/2}\,\theta^{3/2} + \alpha_{1/2}\,\theta^{1/2}$ with $\alpha_{3/2} = 2.11$ and $\alpha_{1/2} = 0.74$.

in the normal fluid regime [54], as displayed in Fig. 6.16,

$$\alpha = \alpha_{3/2}\,\theta^{3/2} + \alpha_{1/2}\,\theta^{1/2}, \tag{6.9}$$

where α is the local shear viscosity and $\theta = T/T_F(n)$ is the local reduced temperature. We obtain $\alpha_{3/2} = 2.11$ and $\alpha_{1/2} = 0.74$.

The coefficient $\bar{\alpha}_{1/2} = 1.87$ obtained from the data is much larger than the local value obtained from the prediction $\alpha_{1/2} = 0.74$. However, to compare these parameters in a meaningful way, we need the trap-average of the reduced temperature,

$$\langle\theta^{1/2}\rangle = \frac{1}{N}\int n\,\theta^{1/2} d^3\mathbf{r}. \tag{6.10}$$

Note that the local reduced temperature is inversely proportional to the local

Fermi temperature $T_F \propto n^{2/3}$. Hence, $\theta = \theta_0 (n/n_0)^{-2/3}$. If assuming a Gaussian distribution for the cloud density profile, we can write Eq. 6.10 as

$$\begin{aligned} \langle \theta^{1/2} \rangle &= \frac{1}{N} \int n(\mathbf{r}) \theta^{1/2} d^3\mathbf{r} \\ &= \theta_0^{1/2} \frac{4}{\sqrt{\pi}} \int_0^\infty q^2 e^{-2q^2/3} dq, \end{aligned} \tag{6.11}$$

where a dimensionless parameter q is defined as $q = (n/n_0)^{2/3}$. Evaluating this integral yields $\langle \theta^{1/2} \rangle = 1.84\, \theta_0^{1/2}$. Hence, the fit to the calculated viscosity yields $\bar{\alpha}_{1/2} = 1.84\, \alpha_{1/2} = 1.84 \times 0.74 = 1.36$, somewhat lower than the fit to the data. However, we can scale the fit coefficients for the predicted viscosity by a factor $2.77/2.11 = 1.31$ so that $\alpha_{3/2}$ agrees by construction with the accepted high temperature two-body limit. Then the predicted $\bar{\alpha}_{1/2}$ increases to $1.31 \times 1.36 = 1.78$, in good agreement with the measurements.

In the low temperature normal fluid regime, Fermi liquid theory [61] predicts that the local viscosity should have an upturn $\propto 1/\theta^2$. After the trap-averaging of θ^{-2} using Eq. 6.11, we find the predicted viscosity near the critical temperature is about a factor of 2 larger than the observed value, with a temperature dependence that is not consistent with our data. The temperature dependence of viscosity near the transition point are still far from being well understood. More work needs to be done to understand the quasi-particle excitations and the formation of pairs in this low temperature regime.

6.5 Bulk viscosity at unitarity

Having measured the shear viscosity from nearly the ground state to the two-body Boltzmann regime using the anisotropic expansion and the radial breathing mode, it is very important to discuss the bulk viscosity, which is not included in Eq. 4.42 and Eq. 4.43 to extract the shear viscosity. The Boltzmann equation for a classical monoatomic gas, with only two-body collisions taken into account, implies zero bulk viscosity [80], as required by the energy conservation. The two-body Boltzmann regime is reached when the mean free path $l_{mfp} = 1/(n\bar{\sigma})$ is comparable to the interparticle spacing $L = n^{-1/3}$. More explicitly,

$$\frac{l_{mfp}}{L} = \frac{1}{n^{2/3}\bar{\sigma}}. \tag{6.12}$$

Using the averaged s-wave cross section $\bar{\sigma} = 4\lambda_T^2$ for the high temperature regime, Eq. 6.12 yields

$$\frac{l_{mfp}}{L} = \frac{3^{2/3}\pi^{1/3}}{16}\frac{T}{T_F(n)}, \tag{6.13}$$

where $T_F(n) = \hbar^2(3\pi^2 n)^{2/3}/2mk_B$ is the local Fermi temperature.

When three-body collisions are included, the Boltzmann equation generally yields a nonzero bulk viscosity. However, as predicted in [45,46], the bulk viscosity vanishes for a unitary Fermi gas in the normal fluid regime even when Boltzmann equation is not valid as a consequence of scale invariance. This is why we did not include the bulk viscosity in Eq. 4.42 and Eq. 4.43 to extract the shear viscosity. In Section 6.5.1, we can show that, by including the bulk viscosity ζ in Eq. 4.42 and Eq. 4.43, the best fit to our anisotropic expansion data in the high temperature regime is the one for which the bulk viscosity exactly vanishes. Section 6.5.2

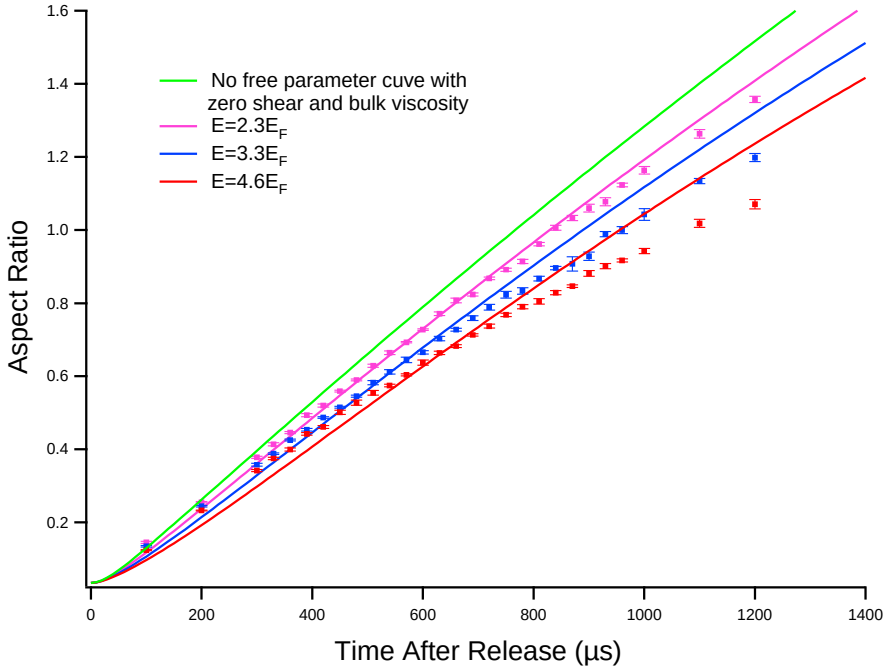

Figure 6.17: Aspect ratio versus expansion time for different energies $E = 2.3E_F$(pink dots), $E = 3.3E_F$(blue dots) and $E = 4.6E_F$(red dots). The green curve is solution for perfect zero viscosity hydrodynamic equations with no free parameters. Pink, blue and red curves are the best χ^2 fits for $E = 2.3E_F$, $E = 3.3E_F$ and $E = 4.6E_F$, using the bulk viscosity as the only free parameter with zero shear viscosity. Error bars denote statistical fluctuations in the aspect ratio.

discusses the bulk viscosity below the superfluid transition point by introducing Landau's two fluid model [88]. In this two fluid model, the bulk viscosity has three components, two of which vanish and the third one exists if there is a relative motion between the superfluid and normal fluid phases.

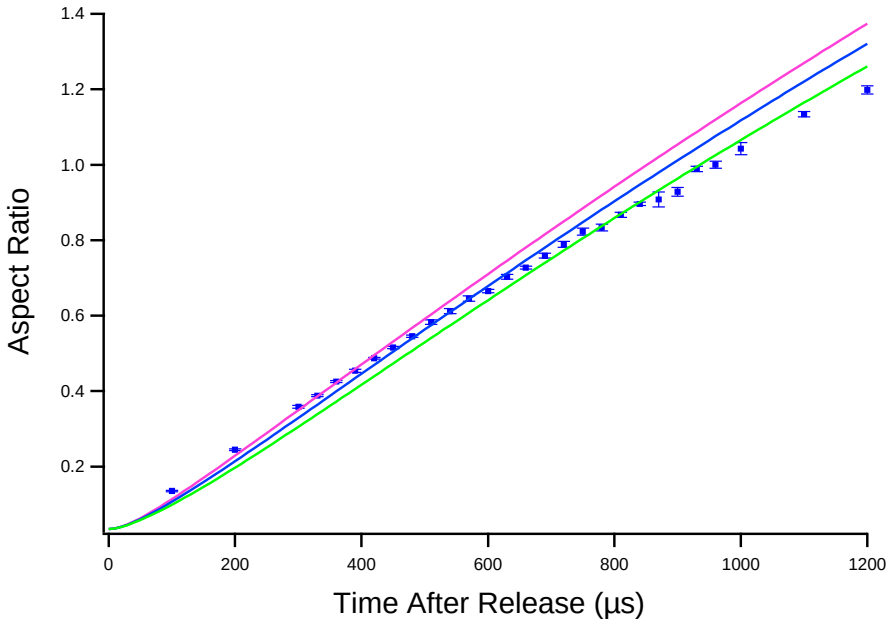

Figure 6.18: Aspect ratio versus expansion time for $E = 3.3E_F$(blue dots). Blue curve is the best χ^2 fit to the data with $\bar{\alpha}_B = 16.7$. Pink and green are the two curves by manually setting $\bar{\alpha}_B = 10$ and $\bar{\alpha}_B = 25$, which both yield larger χ^2. Error bars denote statistical fluctuations in the aspect ratio.

6.5.1 Vanishing of the bulk viscosity in the normal fluid phase

The bulk viscosity is believed to vanish in the normal fluid phase at unitarity [45, 46], so we extract the shear viscosity by excluding the bulk viscosity term in the stress tensor $\delta\mathbf{\Pi}_{ij}$ in Chapter 4. To study the possible effects of the bulk viscosity in the high temperature anisotropic expansion measurement, we include the bulk viscosity $\zeta = \alpha_B \hbar n$ in the hearting rate Eq. 4.35 and the hydrodynamic equations Eq. 4.42 and Eq. 4.43, with the same forms as used above for the density profile, the velocity field and the force per particle to extract the shear viscosity. Note that what we determine from these equations are the trap-averaged bulk viscosity coefficient $\bar{\alpha}_B$ and the trap-averaged shear viscosity coefficient $\bar{\alpha}_S$.

We first switch off the shear viscosity η in Eq. 4.42 and Eq. 4.43, leaving the bulk viscosity ζ as the only free parameter [55]. We then determine the bulk viscosity by applying a χ^2 fit to our high temperature anisotropic data, yielding Fig. 6.17. Here we use the same data points as used for Fig. 6.5, for which the shear viscosity is the only free parameter. Comparing Fig. 6.17 with Fig. 6.5, we find that the pure shear viscosity fits produce the right curvature, which matches the experimental data much better than the pure bulk viscosity fits. This curvature arises from the fact that the anisotropic shear viscosity stress tensor $\eta\sigma_{ij}$ tends to slow down the radial expansion and speed up the axial expansion. In contrast, the bulk viscosity stress tensor $\zeta\nabla\cdot\mathbf{v}$ is a scalar, which symmetrically slows the expansion in all directions. The curvature of the data becomes more pronounced at higher energies, so the pure bulk viscosity fits become even worse at higher energies, which can be seen by comparing the qualities of the pink, blue and red

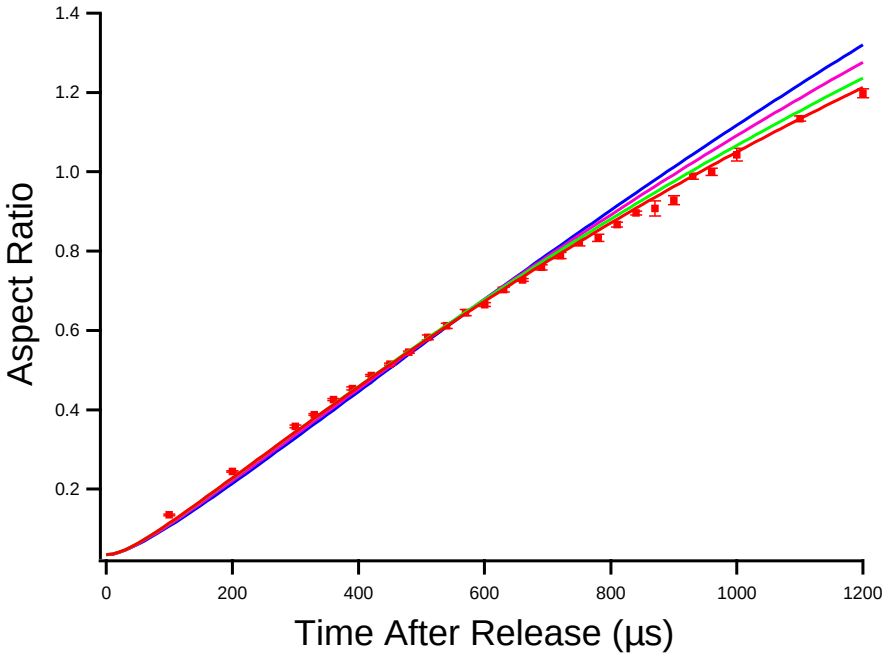

Figure 6.19: Curve fits to the aspect ratio versus expansion time for $E = 3.3E_F$ using pure bulk viscosity. Red dots are the experimental data. The blue curve is the pure bulk viscosity fit with $\bar{\alpha}_B = 16.7$ and $\chi^2 = 8.6$. The pink is the best fit for the shear viscosity $\bar{\alpha}_S$ manually set at 10, yielding $\bar{\alpha}_B = 9.3$ and $\chi^2 = 4.6$. The green is the best fit for the shear viscosity $\bar{\alpha}_S$ manually set at 20, yielding $\bar{\alpha}_B = 2.3$ and $\chi^2 = 2.2$. The red is the globally best fit with $\chi^2 = 1.6$, yielding the shear viscosity $\bar{\alpha}_S = 24.4$ and $\bar{\alpha}_B = 0$. Error bars denote statistical fluctuations in the aspect ratio.

fits to the corresponding data in Fig. 6.17.

Fig. 6.18 displays a few pure bulk viscosity curves to the data for $E/E_F = 3.3$, which corresponds to the blue data point in Fig. 6.17. The blue curve is the best χ^2 pure bulk viscosity fit to this specific data point (That is why it is painted in the same color as the experimental data). The other two curves are obtained by manually dialing the bulk viscosity in our universal hydrodynamic equations with the shear viscosity set at zero. The purpose of doing this is to see if we can obtain a better fit in terms of shape or curvature to the data even though a larger

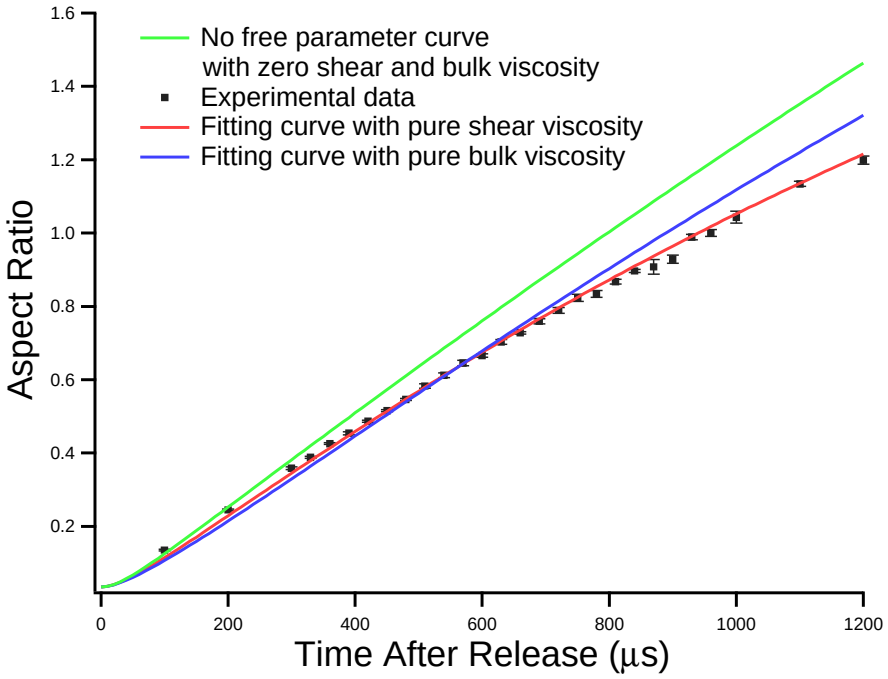

Figure 6.20: Comparison between the best χ^2 fit with pure shear viscosity and the best χ^2 fit with pure bulk viscosity [40]. The green curve is the no free parameter prediction with zero shear and bulk viscosity. The black dots are the anisotropic expansion data at $E/E_F = 3.3$. Error bars denote statistical fluctuations in the aspect ratio. The red curve is the best χ^2 fit with pure shear viscosity coefficient $\bar{\alpha}_S = 24.4$ and reduced $\chi^2 = 1.6$. The blue curve is the best χ^2 fit with pure bulk viscosity coefficient $\bar{\alpha}_B = 16.7$ and reduced $\chi^2 = 8.6$.

χ^2 is obtained. We find that, from Fig. 6.18, none of the three pure bulk viscosity curves exhibits the observed curvature of our data. The pink curve catches a few points at the very beginning but misses a plenty of points later. The green one fits the data points for larger time-of-flight but badly mismatch lots of points at the beginning and in the middle. As discussed, the right curvature arises from the anisotropy of the shear viscosity stress tensor, which is not shared by that for the bulk viscosity.

To study the interplay of the shear and bulk viscosity, we switch on the shear

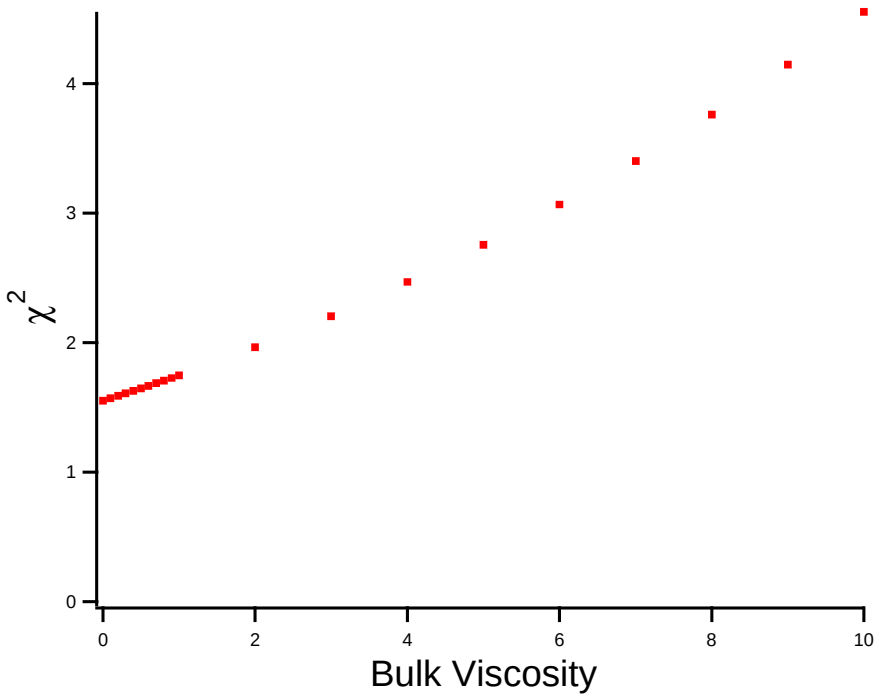

Figure 6.21: χ^2 per degree of freedom versus bulk viscosity with shear viscosity as the only free parameter [40].

viscosity η in Eq. 4.42 and Eq. 4.43. We manually choose a value for the shear viscosity and apply a χ^2 fit to our data with the bulk viscosity as the only free parameter, as shown in Fig. 6.19. The data is taken at $E/E_F = 3.3$, exactly the same as shown in Fig. 6.18. The blue curve is the pure bulk viscosity fit with the $\chi^2 = 8.6$, the same curve as the blue curve in Fig. 6.18. The pink and green ones are the best χ^2 fitting curves with shear viscosity manually set at $\bar{\alpha}_S = 10$ and $\bar{\alpha}_S = 20$, respectively. The corresponding fitted bulk viscosity are $\bar{\alpha}_B = 9.3$ and $\bar{\alpha}_B = 2.3$, respectively. The corresponding χ^2 are $\chi^2 = 4.6$ and $\chi^2 = 2.2$, respectively. We find that, by increasing the shear viscosity, the fitted bulk viscosity value drops and the corresponding χ^2 value decreases, which results in a better fitting curve to the data. This can also be shown in Fig. 6.19. By increasing the value of shear viscosity (from blue to green), we find that the fitting curves gradually produce the right curvature that match with the data. Eventually, we reach the red curve with pure shear viscosity, for which the $\chi^2 = 1.6$ and $\bar{\alpha}_S = 24.4, \bar{\alpha}_B = 0$. This is the globally best χ^2, which indicates the vanishing bulk viscosity. To clearly see the comparison between the pure bulk and pure shear fits, we take out other curves that mediate the blue (pure bulk) and red (pure shear) curves in Fig. 6.19, as shown in Fig. 6.20, where the green one is the no free parameter curve with zero shear and bulk viscosity. From Fig. 6.20, we can directly compare the curvature as well as the χ^2 between these two cases and we can easily find that the pure shear viscosity curve fits our anisotropic expansion data much better than the pure bulk viscosity curve.

Most importantly, we demonstrate that the bulk viscosity vanishes in the normal fluid phase by manually choosing the bulk viscosity and applying a χ^2 fit to our data using the shear viscosity as the only free parameter [55] for the data

point $E/E_F = 3.3$. As shown in Fig. 6.21, zero bulk viscosity gives the minimum reduced χ^2, which means that the high temperature anisotropic expansion data is best fitted with a zero bulk viscosity. This quantitatively shows the vanishing bulk viscosity from our anisotropic expansion experiment conducted at high temperatures, which is consistent with the prediction of vanishing bulk viscosity in the normal fluid phase at unitarity [45, 46]. Using Eq. 6.13, we find that $l_{mfp}/L \sim 0.7$ for $E/E_F \sim 3.3$. This means that we are not rigorously in the two-body Boltzmann regime, which requires $l_{mfp}/L \sim 1$. Hence, the vanishing bulk viscosity at this point could be due to the scale invariance instead of as a consequence of two-tody Boltzmann effect. Further study is required to unveil the property of bulk viscosity at unitarity.

6.5.2 Bulk viscosity below T_c

For the case below the superfluid transition, we need to use Landau's two fluid model [88]. If we denote ρ_n and ρ_s as the normal and superfluid density, Eq 4.1 through Eq 4.3 can be rewritten including both the normal fluid velocity $\mathbf{v}_n$ and density ρ_n, and superfluid velocity $\mathbf{v}_s$ and density ρ_s as [76, 88]

$$\begin{aligned}
\mathbf{j}^{\epsilon} &= \rho s T \mathbf{v}_n + (\mu + \frac{1}{2}\mathbf{v}_s^2)(\rho_s \mathbf{v}_s + \rho_n \mathbf{v}_n) + \rho_n \mathbf{v}_n \mathbf{v}_n \cdot (\mathbf{v}_n - \mathbf{v}_s); \\
\mathbf{g} &= \rho_n \mathbf{v}_n + \rho_s \mathbf{v}_s; \\
\mathbf{\Pi}_{ij} &= P\delta_{ij} + \rho_n v_{n,i} v_{n,j} + \rho_s v_{s,i} v_{s,j},
\end{aligned} \tag{6.14}$$

where s is the entropy per mass and $v_{k,i} = \partial_i v_k$. If we include dissipative corrections, the heating rate arising from the viscous forces can be modified as [88]

$$\begin{aligned}\dot{q} &= \eta \textstyle\sum_{ij} \sigma_{ij}^2/2 + 2\zeta_1 \left(\nabla \cdot \mathbf{v}_n\right) \nabla \cdot [\rho_s(\mathbf{v}_n - \mathbf{v}_s)] \\ &\quad + \zeta_2(\nabla \cdot \mathbf{v}_n)^2 + \zeta_3 \left\{\nabla \cdot [\rho_s(\mathbf{v}_n - \mathbf{v}_s)]\right\}^2 . \end{aligned} \tag{6.15}$$

Note that instead of one parameter ζ, three components of bulk viscosity ζ_1, ζ_2 and ζ_3 are incorporated in this two fluid model. It has been predicted that for a unitary Fermi gas $\zeta_2 = 0$ [45]. Considering the well known inequality $\zeta_1^2 \leq \zeta_2\zeta_3$ [88], the only bulk viscosity term that does not vanish for a unitary Fermi gas below the critical point is ζ_3, which describes the relative motion of the normal and superfluid components. In our low temperature viscosity experiments, the radial breathing mode is excited by releasing the cloud for a short period of time and then recapturing. In this case, even below the transition point T_c, the breathing mode is likely to be an in-phase oscillation of the normal and superfluid parts so that $\mathbf{v}_s = \mathbf{v}_n$. This is consistent with the observed smooth behavior of the breathing frequencies for $E < E_F$. Hence, we expect that the damping is dominated by the shear viscosity of the normal fluid. However, when the temperature is sufficiently low, the normal fluid density gets very small and therefore the mean free path gets very large, which may make the normal fluid decouple from the superfluid. If this happens, the damping would acquire significant contributions from the non-zero bulk viscosity ζ_3 and experiments can be conducted to measure ζ_3.

6.6 Comparison to the string theory conjecture

To compare our unitary Fermi gas to the perfect fluid defined by the string theory conjecture Eq. 1.5, we need to estimate the ratio of the shear viscosity to the entropy density

$$\begin{aligned} \frac{\eta}{s} &= \frac{\alpha\hbar n}{s} \\ &= \frac{\hbar}{k_B}\frac{\alpha}{\frac{s}{nk_B}} \\ &= \frac{\hbar}{k_B}\frac{\bar{\alpha}}{S}, \end{aligned} \tag{6.16}$$

where $\bar{\alpha}$ is the trap-averaged viscosity coefficient and S is the average entropy per particle of the trapped gas in units of k_B.

$\bar{\alpha}$ is obtained from the anisotropic expansion measurement for the high temperature and radial breathing mode for the low temperature, respectively. S is obtained using our power law fit Eq. 5.31 for the low temperature and the second virial coefficient approximation Eq. 5.28 for the high temperature.

Fig. 6.22 shows that the calculated entropy per particle in the high temperature regime joins smoothly with that obtained from the fit for the low temperature measurements. Combining Fig. 6.22 and Fig. 6.13, we can therefore estimate η/s, which is plotted as a function of E/E_F in Fig. 6.23 and the data are listed in Table. 6.3. Fig. 6.24 magnifies the low temperature behavior, for which we find that $\eta/s \simeq 0.4\hbar/k_B$ is about five times that of the string theory limit $hbar/(4\pi k_B) = 0.08\hbar/k_B$ near the critical point $E/E_F = 0.7 - 0.8$ [39]. This is consistent with with recent predictions [65]. Hence, the unitary Fermi gas exhibits nearly perfect fluidity at low temperatures.

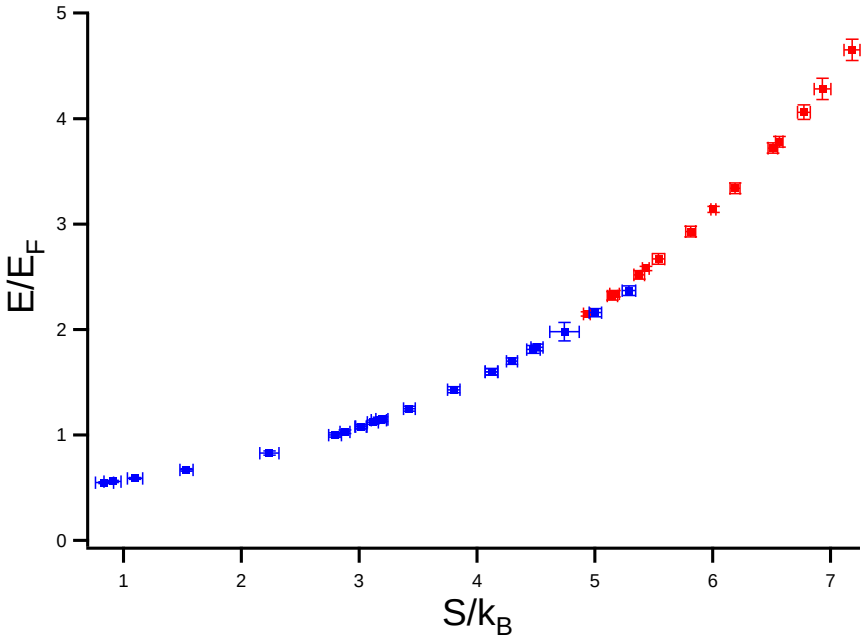

Figure 6.22: Trap-averaged entropy per particle versus average energy per particle for the trapped gas. Blue: Low temperature data obtained from the fit in Fig. 5.1, where error bars arise from the energy uncertainty. Red: High temperature calculation for the deep trap used in the anisotropic expansion experiments, based on the second virial coefficient. Error bars arise from the energy uncertainty.

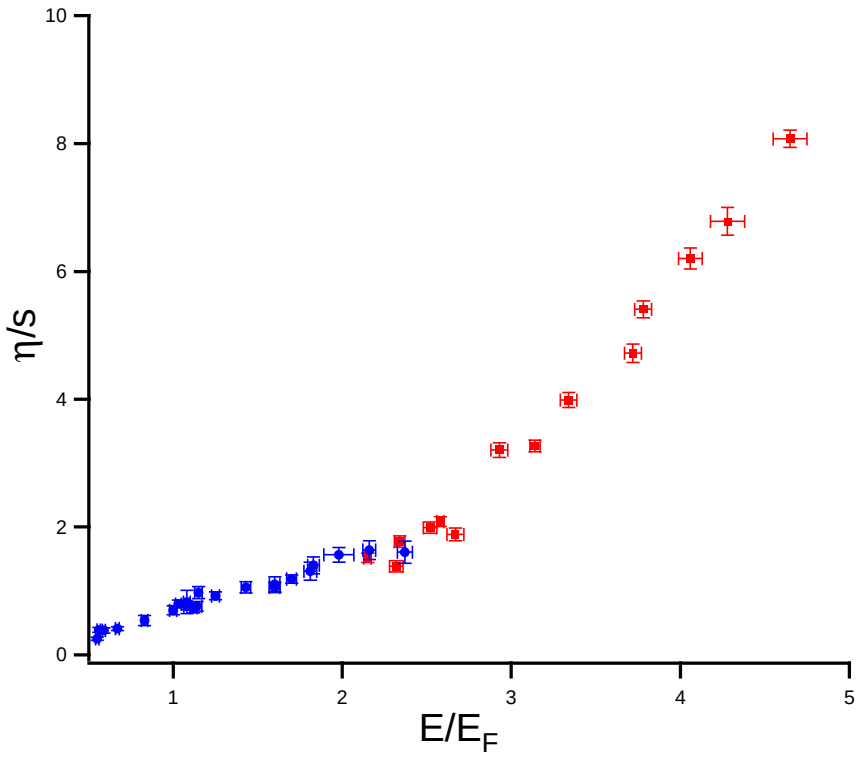

Figure 6.23: Estimated ratio of the shear viscosity to the entropy density. Blue circles: Breathing mode measurements; Red squares: Anisotropic expansion measurements. Bars denote statistical error arising from the uncertainty in E, $\bar{\alpha}$, and S [39].

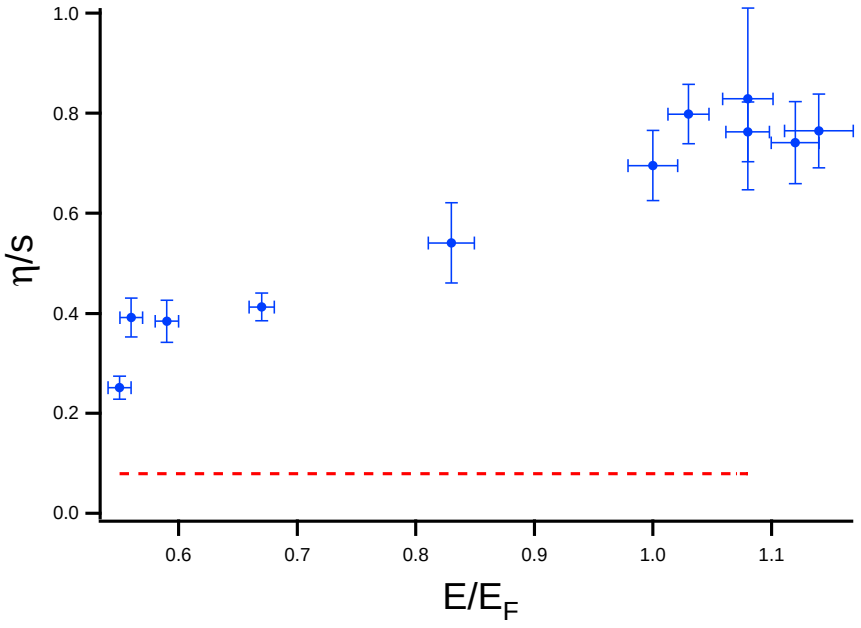

Figure 6.24: Estimated ratio of the shear viscosity to the entropy density at low temperatures. The red dashed line denotes the string theory limit Eq. 1.5. Bars denote statistical error arising from the uncertainty in E, $\bar{\alpha}$, and S [39].

The apparent decrease of the η/s ratio as the energy approaches the ground state $0.48\,E_F$ [32] does not require that the local ratio $\to 0$ as $T \to 0$, since contributions from the cloud edges significantly increase S compared to the local s at the center. More precise conclusions require local measurements of the shear viscosity as well as entropy density.

While η/s is estimated for a unitary Fermi gas, we are interested in comparing it with other fluids that can exhibit perfect fluidity. Ref [65] predicts for a Bose gas $\eta/s \geq 1.7$ times the string theory limit. However, the small η/s requires strongly interactions. Strongly interacting Bose gases are not stable due to the three-body recombination. For a liquid helium, this ratio is about 10 times the string theory limit near the endpoint of the liquid gas phase transition [76]. For quark gluon plasma, recent results show that this ratio can go even closer to the string theory limit [79]. It is still an ongoing searching for the most perfect fluid among a number of fluids in nature.

Table 6.3: Energy E/E_F, local reduced temperature at the trap center for a unitary Fermi gas $T/T_F(n)$ and η/s in units of $\hbar/k_B$.

	E/E_F	$T/T_F(n)$	η/s
1	0.55(1)	0.072(10)	0.25(2)
2	0.56(1)	0.078(12)	0.39(4)
3	0.59(1)	0.092(15)	0.38(4)
4	0.67(1)	0.126(21)	0.41(3)
5	0.83(2)	0.208(5)	0.54(8)
6	1.00(2)	0.331(15)	0.70(7)
7	1.03(2)	0.354(16)	0.80(6)
8	1.08(2)	0.395(20)	0.83(18)
9	1.08(2)	0.393(20)	0.76(6)
10	1.12(2)	0.428(22)	0.74(8)
11	1.14(3)	0.445(23)	0.76(7)
12	1.15(2)	0.453(24)	0.97(10)
13	1.25(2)	0.539(31)	0.92(6)
14	1.43(3)	0.704(44)	1.06(9)
15	1.60(3)	0.879(58)	1.05(8)
16	1.60(3)	0.881(58)	1.11(12)
17	1.70(3)	0.989(67)	1.19(6)
18	1.83(3)	1.143(79)	1.40(13)
19	1.81(4)	1.117(77)	1.31(14)
20	1.98(9)	1.322(94)	1.57(11)
21	2.16(4)	1.562(114)	1.64(15)
22	2.37(5)	1.860(138)	1.61(17)
23	2.15(2)	1.54(3)	1.52(7)
24	2.32(4)	1.78(5)	1.39(9)
25	2.34(4)	1.80(5)	1.77(9)
26	2.52(4)	2.07(6)	1.99(9)
27	2.58(2)	2.15(4)	2.09(8)
28	2.67(5)	2.31(8)	1.89(10)
29	2.93(5)	2.77(8)	3.21(12)
30	3.14(3)	3.15(4)	3.27(9)
31	3.34(5)	3.56(10)	3.99(12)
32	3.72(5)	4.41(12)	4.72(14)
33	3.78(5)	4.57(10)	5.41(13)
34	4.06(7)	5.25(19)	6.20(17)
35	4.28(10)	5.84(28)	6.78(22)
36	4.65(10)	6.92(31)	8.08(13)

Chapter 7

Summary and Outlook

7.1 Summary

This dissertation reports the measurement of quantum shear viscosity from nearly the ground state up to the two-body Boltzmann regime in a unitary Fermi gas, which presents the first measurement of a transport coefficient for a unitary Fermi gas. To measure the shear viscosity at unitarity, two experiments are employed for different temperature regimes: the anisotropic expansion at high temperatures and the radial breathing mode at low temperatures. The universal hydrodynamic equations derived from first principles accurately describe the hydrodynamic behaviors of a universal Fermi gas and hence are used to extract shear viscosity form experiments. The high temperature scaling for the shear viscosity is demonstrated using the anisotropic expansion experiment. The demonstration of this predicted scaling is of great importance because it sets a benchmark for understanding the low temperature shear viscosity measurement. The smooth joining between the high temperature and low temperature shear viscosity measurements shows that both the friction force and heating are properly included in our universal hydrodynamic equations. Besides the measurement of the shear viscosity, the predicted vanishing bulk viscosity for a normal phase unitary Fermi gas is also demonstrated

for the first time using our anisotropic expansion experiment. The ratio of the shear viscosity to the entropy density can be estimated using the results of the viscosity measurements and the previously measured entropy density. It is found that this ratio is about 5 times the string theory limit at the normal-superfluid transition point, which shows that the unitary Fermi gas exhibits nearly perfect fluidity at low temperatures.

This dissertation also presents consistent and accurate calibrations of the energy and the temperature for a unitary Fermi gas. For the energy calibration, the virial theorem is utilized, which allows to calculate the energy from the cloud dimensions for a harmonically trapped unitary Fermi gas. For the temperature calibrations, two methods are used for different temperature regimes. At high temperatures, the second virial coefficient approximation is applied to the energy density for a unitary Fermi gas. By using fundamental thermodynamic relations and considering the trap condition, other thermodynamic quantities, including the temperature, can be readily obtained. At low temperatures, the previously measured entropy-energy curve is optimized and re-analyzed, yielding an accurate determination of the temperature for a unitary Fermi gas.

The hydrodynamic equations and the energy and temperature calibrations are originally derived and used for the viscosity measurements. However, they are all universal and hence can also be applied to studying hydrodynamics and thermodynamics of other strongly coupled systems.

7.2 Outlook

While the trap-averaged shear viscosity is measured for a unitary Fermi gas in this dissertation, other interesting topics on viscosity can be explored in future. These topics include the direct measurement of the shear viscosity for an off-resonant Fermi gas, the measurement of bulk viscosity for a unitary Fermi gas and the shear and bulk viscosities in reduced dimensions.

7.2.1 Shear viscosity off-resonance

As already discussed, the shear viscosity is inversely proportional to the s-wave scattering cross section, yielding a smaller shear viscosity at unitarity as compared to that for a weakly interacting Fermi gas. The shear viscosity for the unitary regime is particularly important, because the unitary Fermi gas is scale-invariant and universal. However, it is still important to study the shear viscosity off resonance, where scale-invariant no longer holds.

When tuned off resonance, our hydrodynamic equations are still expected to hold and the anisotropic expansion experiment is also expected to be effective to extract viscosity at high temperatures. However, some complications are introduced to deal with the analysis. First, the scattering length a presents another length scale in addition to the interparticle spacing $1/k$ and the s-wave cross section is then $\sigma = 4\pi a^2/(1 + k^2a^2)$. Hence, the shear viscosity should have some dependence on the scattering length. Further, the equation of state $P = 2\mathcal{E}/3$ does not hold for an off-resonant gas. For the high temperature regime, we are still able to make use of the second virial approximation by more general b_2, including the formation of bound molecules and the off-resonance scattering phase

shift. Detailed discussions can be found in [27].

7.2.2 Bulk viscosity at unitarity

Bulk viscosity is predicted to vanish for a scale invariant system such as the unitary Fermi gas. Our high temperature anisotropic expansion data shows the very different effects on expansion dynamics arising from the shear and bulk viscosity and supports the vanishing bulk viscosity. However, it is not a direct measurement of bulk viscosity. To directly measure the bulk viscosity in the normal fluid phase at unitarity, we can excite the radial and axial breathing mode at the same energy for the same trap conditions and measure the damping rate for each mode. As discussed earlier in this thesis, the breathing mode at unitarity obeys the universal hydrodynamic equations. If bulk viscosity is included, the damping rate of the radial breathing mode τ_{radial} is related to the trap-averaged shear viscosity $\bar{\alpha}_S$ and bulk viscosity $\bar{\alpha}_B$ as

$$\frac{1}{\tau_{radial}} = \frac{\hbar\left(\bar{\alpha}_S + 3\bar{\alpha}_B\right)}{3m\langle x^2\rangle_0}\left(1-\delta\right) \tag{7.1}$$

and the damping rate of the axial breathing mode τ_{axial} is related to the trap-averaged shear viscosity $\bar{\alpha}_S$ and bulk viscosity $\bar{\alpha}_B$ as

$$\frac{1}{\tau_{axial}} = \frac{\lambda^2\hbar\left(\frac{12}{5}\bar{\alpha}_S + \frac{9}{10}\bar{\alpha}_B\right)}{3m\langle x^2\rangle_0}\left(1-\delta\right). \tag{7.2}$$

Here $\lambda = \omega_z/(\sqrt{\omega_x\omega_y})$ and $\delta \equiv (\omega_x - \omega_y)/\sqrt{\omega_x\omega_y} << 1$ for a slight asymmetric trap. Note that these two relations have different coefficient for the shear and bulk viscosity. Therefore, the ratio of these two damping rate $\tau_{radial}/\tau_{axial}$ reveals

the ratio of the shear and bulk viscosity $\gamma = \bar{\alpha}_B/\bar{\alpha}_S$ as

$$\frac{\tau_{radial}}{\tau_{axial}} = \lambda^2 \frac{\frac{12}{5} + \frac{9}{10}\gamma}{1 + 3\gamma} \tag{7.3}$$

If bulk viscosity really vanishes at unitarity with $\gamma \ll 1$, the ratio of the two damping rates is expected to be $12\lambda^2/5$.

For the bulk viscosity below the normal-superfluid transition, as discussed before, the two fluid model utilizes three components for the bulk viscosity, two of which vanish anyway for a unitary Fermi gas. The third one that describes the relative motion of the two fluids does not vanish if the relative motion of the two fluids is excited. As said before, our radial breathing mode is actually an in-phase oscillation between the two fluids even below critical temperatures. In order to measure the non-vanishing bulk viscosity component below the critical point, we need to purposely excite an out-phase oscillation between the two fluids. By taking advantage of the fact that the cloud is actually a superfluid core surrounded by normal fluid as the local reduced temperature is low around the center and high at edges, a possible way to experimentally excite this relative motion is to add a local perturbation using a blue-detuned repulsive beam on the cloud edge [100]. As a result of this perturbation, the normal fluid part can be decoupled from the superfluid part and therefore a relative motion is created.

7.2.3 Shear viscosity in reduced dimensions

This dissertation shows that the three-dimensional unitary Fermi gas exhibits nearly perfect fluidity at low temperatures. It would be of great interest to see if this perfect fluidity exists in reduced dimensions, such as a two-dimensional Fermi

gas with a tightly confined direction in a pancake shape. It is suggested that electrons in graphene might behave as a nearly perfect fluid [96]. To investigate this, it is necessary to measure the viscosity for a two-dimensional Fermi gas. A recent experiment measures the damping of the collective modes in a 2D geometry and estimates the shear viscosity [97]. Recent theoretical work also investigates the experiential results and shows qualitative agreement [98, 99]. However, much more work is needed to characterize shear and bulk viscosities in a two-dimensional Fermi gas.

Appendix A

Derivation of the universal high temperature scaling

At high temperatures where the two-body Boltzmann regime is approached, the Boltzmann equation can be used to calculate the temperature dependence of the shear viscosity. A universal $T^{3/2}$ temperature scaling of shear viscosity has been predicted in the high temperature two-body Boltzmann regime for a unitary Fermi gas [36], as shown in Eq. 1.3. In this appendix, I will briefly show the derivation of this universal temperature scaling by virtue of the Boltzmann equation [101]. Section A.1 introduces the method developed in Ref. [101] to find the approximate solutions to the Boltzmann equation. Section A.2 obtains the temperature scaling of shear viscosity for a unitary Fermi gas in the two-body Boltzmann regime by incorporating the collisional properties of a unitary Fermi gas to the approximate solutions. Please refer to Ref. [101] for detailed derivations.

A.1 Approximation method of solving the Boltzmann equation

Let's start with the Boltzmann equation

$$\mathbf{D}f = \mathbf{D_c}f. \tag{A.1}$$

More explicitly, the Boltzmann equation can be written as

$$\frac{\partial f}{\partial t} + \mathbf{v}\cdot\frac{\partial f}{\partial \mathbf{r}} + \frac{\mathbf{F}}{m}\cdot\frac{\partial f}{\partial \mathbf{v}} = \int_{\mathbf{v_1}}\int_{\mathbf{v_1'}}\int_{\mathbf{v'}}(f'f_1' - ff_1)\mathbf{V}\sigma d^3\mathbf{v_1}d^3\mathbf{v_1'}d^3\mathbf{v'}, \tag{A.2}$$

where f is the number distribution of particles, $\mathbf{F}$ is the external force, σ is the collisional cross section and $\mathbf{V}$ is the relative velocity between two colliding particles. To find the distribution function $f(\mathbf{r},\mathbf{v},t)$ for the Boltzmann equation, it is useful to assume that we are looking at a situation that is not too far away from equilibrium. Then we expect that $f(\mathbf{r},\mathbf{v},t)$ does not differ too much from a Maxwell distribution $f^0(\mathbf{r},\mathbf{v},t)$, where the superscript 0 denotes equilibrium. The Maxwell distribution for the local equilibrium conditions is [101],

$$f^0(\mathbf{r},\mathbf{v},t) = n\left(\frac{m\beta}{2\pi}\right)^{3/2} e^{-\frac{1}{2}\beta m(\mathbf{v}-\mathbf{u})^2}, \tag{A.3}$$

where n, β and $\mathbf{u}$ are all independent of velocity $\mathbf{v}$. As the system is not far from equilibrium, f can be written in the form as

$$f = f^0(1+\Phi) \qquad \Phi \ll 1. \tag{A.4}$$

Since $\Phi \ll 1$, the left side of Eq. A.1 yields $\mathbf{D}f \approx \mathbf{D}f^0$ and the right side of Eq. A.2 can be written as

$$\mathbf{D_c}f = \int\int d^3\mathbf{v_1}d\Omega^{'}(f^{'}f_1^{'} - ff_1)\mathbf{V}\sigma, \tag{A.5}$$

where $ff_1 = f^0 f_1^0(1+\Phi+\Phi_1)$ and $f^{'}f_1^{'} = f^0 f_1^0(1+\Phi^{'}+\Phi_1^{'})$. Hence,the Boltzmann equation Eq. A.2 yields

$$\frac{\partial f^0}{\partial t} + \mathbf{v}\cdot\frac{\partial f^0}{\partial \mathbf{r}} + \frac{\mathbf{F}}{m}\cdot\frac{\partial f^0}{\partial \mathbf{v}} = \int\int d^3\mathbf{v}d\Omega^{'} f^0 f_1^0 \mathbf{V}\sigma \triangle \Phi, \tag{A.6}$$

where $\triangle\Phi = \Phi^{'} + \Phi_1^{'} - \Phi - \Phi_1$.

A.2 Calculating the shear viscosity coefficient

Without losing generality, we assume that the gas has a mean velocity $u_x(z)$ in the x-direction with a z-direction dependence. Hence, it has a velocity gradient $\partial u_x(z)/\partial z$. By evaluating Eq. A.6 (see Ref. [101] for details), the pressure tensor P_{xz} can be expressed as

$$P_{xz} = \frac{n^2}{\beta^3 m^2}\frac{1}{I}\frac{\partial u_x}{\partial z}, \tag{A.7}$$

where $\beta = 1/k_B T$ and I is an integral defined as

$$I = -\frac{3}{16}n^2\left(\frac{m\beta}{2\pi}\right)^3\left(\frac{\pi}{m\beta}\right)^{3/2}\int_{-\infty}^{\infty} d^3\mathbf{V}e^{-\frac{\beta m}{4}V^2}V_x^2 V_z^2 V\sigma_\eta(V). \tag{A.8}$$

The shear viscosity η is related to the pressure tensor as

$$P_{xz} = -\eta\frac{\partial u_x}{\partial z}. \tag{A.9}$$

If we define

$$I_1 = \int_{-\infty}^{\infty} d^3\mathbf{V} e^{-\frac{\beta m}{4}V^2} V_x^2 V_z^2 V \sigma_\eta(V), \tag{A.10}$$

Eq. A.8 yields

$$I = -\frac{3}{16} n^2 \left(\frac{m\beta}{2\pi}\right)^3 \left(\frac{\pi}{m\beta}\right)^{3/2} I_1. \tag{A.11}$$

Combining Eq. A.7, Eq. A.9 and Eq. A.11, the shear viscosity can be written as

$$\eta = \frac{128}{3} \frac{\pi^{3/2}}{m^{7/2}\beta^{9/2}} \frac{1}{I_1}. \tag{A.12}$$

Now we need to evaluate I_1 defined as Eq. A.10. Using the spherical coordinates with $V_x = V \sin\theta \cos\phi$ and $V_z = V \cos\theta$, we have

$$I_1 = \int_0^{2\pi} d\phi \cos^2\phi \int_0^{\pi} d\theta \sin^3\theta \cos^2\theta \int_0^{\infty} dV V^7 e^{-\frac{\beta m}{4}V^2} \sigma_\eta(V). \tag{A.13}$$

The first integral and the second integral give π and $4/15$, respectively. Hence, Eq. A.13 can be simplified as

$$I_1 = \frac{4}{15}\pi \int_0^{\infty} dV V^7 e^{-\frac{\beta m}{4}V^2} \sigma_\eta(V). \tag{A.14}$$

Here $\sigma_\eta(V)$ is the effective cross section as [101]

$$\sigma_\eta(V) = 2\pi \int_0^{\pi} \sigma(V,\theta) \sin^3\theta d\theta, \tag{A.15}$$

where $\sigma(V,\theta)$ is the differential cross section as shown in Eq. 2.41. Using the scattering amplitude defined in Eq. 2.38, Eq. A.15 reduces as

$$\sigma_\eta(V) = 2\pi \int_0^\pi \frac{2}{k^2} \sin^3\theta d\theta. \tag{A.16}$$

Evaluating this integral gives the effective cross section as

$$\sigma_\eta(V) = \frac{4}{3}\frac{4\pi}{k^2} = \frac{16\pi\hbar^2}{3m^2V^2}. \tag{A.17}$$

Eq. A.19 then yields as

$$I_1 = \frac{16\pi^2\hbar^2}{45m^2} \int_0^\infty dV V^5 e^{-\frac{\beta m}{4}V^2}. \tag{A.18}$$

Evaluating this integral yields

$$I_1 = \frac{64^2}{45}\frac{\pi^2\hbar^2}{m^5\beta^3}. \tag{A.19}$$

Using I_1, the shear viscosity in Eq. A.12 can be written as

$$\eta = \frac{15m^{3/2}k_B^{3/2}}{32\sqrt{\pi}\hbar^2} T^{3/2}, \tag{A.20}$$

which is exactly Eq. 1.3. More explicitly, if we define $\eta = \alpha\hbar\, n$, the shear viscosity coefficient α can be expressed as

$$\alpha = \frac{15m^{3/2}k_B^{3/2}}{32\sqrt{\pi}\hbar^3 n} T^{3/2}. \tag{A.21}$$

Using the local Fermi temperature $T_F(n) = \hbar^2(3\pi^2 n)^{2/3}/(2mk_B)$, the shear viscosity coefficient yields

$$\alpha = \frac{45\pi^{3/2}}{64\sqrt{2}} \left(\frac{T}{T_F(n)}\right)^{3/2} = 2.77 \left(\frac{T}{T_F(n)}\right)^{3/2}, \tag{A.22}$$

which agrees with Eq. 1.4.

Bibliography

[1] M. H. Anderson, J. R. Ensher, M. R. Matthews, C. E. Wieman, and E. A. Cornell. Observation of Bose-Einstein condensation in a dilute atomic vapor. *Science*, 269:198, 1995.

[2] C. C. Bradley, C. A. Sackett, J. J. Tollett, and R. G. Hulet. Evidence of Bose-Einstein condensation in an atomic gas with attractive interactions. *Phys. Rev. Lett.*, 75:1687, 1995. ibid. 79, 1170 (1997).

[3] K. B. Davis, M.-O. Mewes, M. R. Andrews, N. J. van Druten, D. S. Durfee, D. M. Kurn, and W. Ketterle. Bose-Einstein condensation in a gas of sodium atoms. *Phys. Rev. Lett.*, 75:3969, 1995.

[4] P. K. Kovtun, D. T. Son, and A. O. Starinets. Viscosity in strongly interacting quantum field theories from black hole physics. *Phys. Rev. Lett.*, 94:111601, 2005.

[5] L. P. Csernai, J. I. Kupusta, and L. D. McClerran. On the strongly-interacting low-viscosity matter created in relativistic nuclear collisions. *Phys. Rev. Lett.*, 97:152303, 2006.

[6] P. F. Kolb and U. Heinz. *Quark Gluon Plasma 3*, page 634. World Scientific, 2003.

[7] K. M. O'Hara, S. L. Hemmer, M. E. Gehm, S. R. Granade, and J. E. Thomas. Observation of a strongly interacting degenerate Fermi gas of atoms. *Science*, 298:2179, 2002.

[8] B. DeMarco and D. S. Jin. Onset of Fermi degeneracy in a trapped atomic gas. *Science*, 285:1703, 1999.

[9] Truscott, A. G., Strecker, K. E., McAlexander, W. I., Partridge, G. B., and Hulet, R. G. Observation of Fermi pressure in a gas of trapped atoms. *Science*, 291:2570, 2001.

[10] K. Dieckmann, C. A. Stan, S. Gupta, Z. Hadzibabic, C. H. Schunck, and W. Ketterle. Decay of an ultracold fermionic lithium gas near a Feshbach resonance. *Phys. Rev. Lett.*, 89:203201, 2002.

[11] Schreck, F., Khaykovich, L., Corwin, K. L., Ferrari, G., Bourdel, T., Cubizolles, J., and Salomon, C. Quasipure Bose-Einstein condenstae immersed in a Fermi sea. *Phys. Rev. Lett.*, 87(8):080403, 2001.

[12] S. R. Granade, M. E. Gehm, K. M. O'Hara, and J. E. Thomas. All-optical production of a degenerate Fermi gas. *Phys. Rev. Lett.*, 88(12):120405, 2002.

[13] S. Jochim, M. Bartenstein, G. Hendl, J. Hecker Denschlag, R. Grimm, A. Mosk, and M.Weidemüller. Magnetic field control of elastic scattering in a cold gas of fermionic lithium atoms. *Phys. Rev. Lett.*, 89:273202, 2002.

[14] C. A. Regal, M. Greiner, and D. S. Jin. Observation of resonance condensation of fermionic atom pairs. *Phys. Rev. Lett.*, 92:040403, 2004.

[15] M. W. Zwierlein, C. A. Stan, C. H. Schunck, S. M. F. Raupach, A. J. Kerman, and W. Ketterle. Condensation of pairs of fermionic atoms near a Feshbach resonance. *Phys. Rev. Lett.*, 92:120403, 2004.

[16] J. Kinast, S. L. Hemmer, M.E. Gehm, A. Turlapov, and J. E. Thomas. Evidence for superfluidity in a resonantly interacting Fermi gas. *Phys. Rev. Lett.*, 92:150402, 2004.

[17] M. Bartenstein, A. Altmeyer, S. Riedl, S. Jochim, C. Chin, J. Hecker Denschlag, and R. Grimm. Collective excitations of a degenerate gas at the BEC-BCS crossover. *Phys. Rev. Lett.*, 92:203201, 2004.

[18] C. Chin, M. Bartenstein, A. Altmeyer, S. Riedl, S. Jochim, J. Hecker Denschlag, and R. Grimm. Observation of the pairing gap in a strongly interacting Fermi gas. *Science*, 305:1128, 2004.

[19] M. W. Zwierlein, J. R. Abo-Shaeer, A. Schirotzek, C. H. Schunck, and W. Ketterle. Vortices and superfluidity in a strongly interacting Fermi gas. *Nature*, 435:1047, 2005.

[20] G. B. Partridge, W. Li, R. I Kamar, Y. Liao, and R. G. Hulet. Pairing and phase separation in a polarized Fermi gas. *Science*, 311:503, 2006.

[21] M. W. Zwierlein, A. Schirotzek, C. H. Schunck, and W. Ketterle. Fermionic superfluidity with imbalanced spin populations. *Science*, 311:492, 2006.

[22] B. Clancy, L. Luo, and J. E. Thomas. Observation of nearly perfect irrotational flow in normal and superfluid strongly interacting fermi gases. *Phys. Rev. Lett.*, 99:140401, 2007.

[23] S. Giorgini, L. P. Pitaevskii, and S. Stringari. Theory of ultracold atomic Fermi gases. *Rev. Mod. Phys.*, 80:1215, 2008.

[24] I. Bloch, J. Dalibard, and W. Zwerger. Many-body physics with ultracold gases. *Rev. Mod. Phys.*, 80:885, 2008.

[25] W. Ketterle and M. W. Zwierlein. *Making, probing and understanding ultracold Fermi gases*. IOS Press, Amsterdam, 2008. in Ultracold Fermi Gases, Proceedings of the International School of Physics Enrico Fermi, Course CLXIV, Varenna, 20 - 30 June 2006.

[26] The experiments are performed far from p-wave Feshbach resonances. The relevant threshold energy for p-wave scattering is then comparable to the barrier height. Using the known C_6 coefficients, the barrier height for ^{40}K is 280 μK, while for ^{6}Li, it is 8 mK. Hence, for temperatures in the μK range, as used in the experiments, p-wave scattering is negligible and s-wave scattering dominates.

[27] T.-L. Ho. Universal thermodynamics of degenerate quantum gases in the unitarity limit. *Phys. Rev. Lett.*, 92:090402, 2004.

[28] J. Kinast, A. Turlapov, J. E. Thomas, Q. Chen, J. Stajic, and K. Levin. Heat capacity of strongly-interacting Fermi gas. *Science*, 307:1296, 2005.

[29] L. Luo, B. Clancy, J. Joseph, J. Kinast, and J. E. Thomas. Measurement of the entropy and critical temperature of a strongly interacting Fermi gas. *Phys. Rev. Lett.*, 98:080402, 2007.

[30] J. T. Stewart, J. P. Gaebler, C. A. Regal, and D. S. Jin. The potential energy of a ^{40}K Fermi gas in the BCS-BEC crossover. *Phys. Rev. Lett.*, 2006.

[31] H. Hu, P. D. Drummond, and X.-J. Liu. Universal thermodynamics of strongly interacting Fermi gases. *Nature Physics*, 3:469, 2007.

[32] L. Luo and J. E. Thomas. Thermodynamic measurements in a strongly interacting Fermi gas. *J. Low Temp. Phys.*, 154:1, 2009.

[33] M. Horikoshi, S. Najajima, M. Ueda, and T. Mukaiyama. Measurement of universal thermodynamic functions for a unitary Fermi gas. *Science*, 327:442, 2010.

[34] S. Nascimbène, N. Navon, K. J. Jiang, F. Chevy, and C. Salomon. Exploring the thermodynamics of a universal Fermi gas. *Nature*, 463:1057, 2010.

[35] B. A. Gelman, E. V. Shuryak, and I. Zahed. Ultracold strongly coupled gas: A near-ideal liquid. *Phys. Rev. A*, 72:043601, 2005.

[36] G. M. Bruun and H. Smith. Shear viscosity and damping for a Fermi gas in the unitary limit. *Phys. Rev. A*, 75:043612, 2007.

[37] T. Schäfer. The shear viscosity to entropy density ratio of trapped fermions in the unitary limit. *Phys. Rev. A*, 76:063618, 2007.

[38] A. Turlapov, J. Kinast, B. Clancy, L. Luo, J. Joseph, and J. E. Thomas. Is a gas of strongly interacting atomic fermions a nearly perfect fluid? *J. Low Temp. Phys.*, 150:567, 2008.

[39] C. Cao, E. Elliott, J. Joseph, H. Wu, J. Petricka, T. Schäfer, and J. E. Thomas. Universal quantum viscosity in a unitary Fermi gas. *Science*, 331:58, 2011.

[40] C. Cao, E. Elliott, H. Wu, and J. E. Thomas. Searching for Perfect Fluids: Quantum Viscosity in a Universal Fermi Gas. *New Journal of Physics*, 13:075007,2011.

[41] J. Kinast, A. Turlapov, and J. E. Thomas. Damping of a unitary Fermi gas. *Phys. Rev. Lett.*, 94:170404, 2005.

[42] J. E. Thomas, J. Kinast, and A. Turlapov. Virial theorem and universality in a unitary Fermi gas. *Phys. Rev. Lett.*, 95:120402, 2005.

[43] T. Schäfer. Dissipative fluid dynamics for the dilute Fermi gas at unitarity: Free expansion and rotation. http://arxiv.org/abs/1008.3876v1.

[44] C. Menotti, P. Pedri, and S. Stringari. Expansion of an interacting Fermi gas. *Phys. Rev. Lett.*, 89:250402, 2002.

[45] D. T. Son. Vanishing bulk viscosities and conformal invariance of the unitary Fermi gas. *Phys. Rev. Lett.*, 98:020604, 2007.

[46] M. A. Escobedo, M. Mannarelli, and C. Manuel. Bulk viscosities for cold Fermi superfluids close to the unitary limit. *Phys. Rev. A*, 79:063623, 2009.

[47] P. Massignan, G. M. Bruun, and H. Smith. Viscous relaxation and collective oscillations in a trapped Fermi gas near the unitarity limit. *Phys. Rev. A*, 71:033607, 2005.

[48] K. M. O'Hara, S. R. Granade, M. E. Gehm, T. A. Savard, S. Bali, C. Freed, and J. E. Thomas. Ultrastable CO_2 laser trapping of lithium fermions. *Phys. Rev. Lett.*, 82:4204, 1999.

[49] M. Bartenstein, A. Altmeyer, S. Riedl, R. Geursen, S. Jochim, C. Chin, J. Hecker Denschlag, R. Grimm, A. Simoni, E. Tiesinga, C. J. Williams, and P. S. Julienne. Precise determination of ^{6}Li cold collision parameters by radio-frequency spectroscopy on weakly bound molecules. *Phys. Rev. Lett.*, 94:103201, 2005.

[50] J. Joseph, B. Clancy, L. Luo, J. Kinast, A. Turlapov, and J. E. Thomas. Measurement of sound velocity in a Fermi gas near a Feshbach resonance. *Phys. Rev. Lett.*, 98:170401, 2007.

[51] H. Guo, D. Wulin, C.-C. Chien, and K. Levin. Microscopic approach to viscosities in superfluid Fermi gases: From BCS to BEC. http://arxiv.org/abs/1008.0423v3.

[52] E. Taylor and M. Randeria. Viscosity of strongly interacting quantum fluids: spectral functions and sum rules. *Phys. Rev. A*, 81, 2010.

[53] L. Luo, B. Clancy, J. Joseph, J. Kinast, A. Turlapov, and J. E. Thomas. Evaporative cooling of unitary Fermi gas mixtures in optical traps. *New Journal of Physics*, 8:213, 2006.

[54] T. Enss, R. Haussmann, and W. Zwerger. Viscosity and scale invariance in the unitary Fermi gas. *Annals Phys.*, 326, 2011.

[55] The method of finding the bulk viscosity as a function of χ^2 was suggested to us by Thomas Schäfer, North Carolina State University, private communication.

[56] T.-L. Ho and E. Mueller. High temperature expansion applied to fermions near Feshbach resonance. *Phys. Rev. Lett.*, 92:160404, 2004.

[57] Note the the temperature calibration published in Ref. [32] employed the ideal gas approximation to the entropy, Fig. 4 and Fig. 7 of Ref. [32], while the detailed comparisons with predictions, Fig. 5 of Ref. [32], employed the corrected entropy. See Table 1 of Ref. [32].

[58] H. Hu, X.-J. Liu, and P. D. Drummond. Universal thermodynamics of a strongly interacting Fermi gas: theory versus experiment. *New J. of Phys.*, 12:063038, 2011.

[59] G. E. Astrakharchik, J. Boronat, J. Casulleras, and S. Giorgini. Equation of state of a Fermi gas in the BEC-BCS crossover: A quantum monte carlo study. *Phys. Rev. Lett.*, 93:200404, 2004.

[60] T. Schäfer and C. Chafin. Scaling flows and dissipation in the dilute Fermi gas at unitarity. http://arxiv.org/abs/0912.4236v3.

[61] G. M. Bruun. Spin diffusion in Fermi gases. *New J. Phys.*, 13:035005, 2011.

[62] U. Heinz. The quark-gluon plasma at RHIC. *Nucl. Phys. A.*, 721:30, 2003.

[63] E. Shuryak. Why does the quark-gluon plasma at RHIC behave as a nearly ideal fluid? *Prog. Part. Nucl. Phys.*, 53:273, 2004.

[64] D. A. Butts, D. S. Rokhsar. Trapped Fermi gases. *Phys. Rev. A*, 55:4346, 1997.

[65] A. LeClair. On the viscosity to entropy density ratio for unitary Bose and Fermi gases. arXiv:1012.5653v1[cond-mat.quant.gas], 2010.

[66] L. P. Csernai and J. I. Kupusta and L. D. McClerran. On the strongly-interacting low-viscosity matter created in relativistic nuclear collision. *Phys. Rev. Lett.*, 97:152303, 2006.

[67] K. M. O'Hara. Optical Trapping and Evaporative Cooling of Fermionic Atoms. PhD thesis, Duke University, 2000.

[68] S. R. Granade. All-optical Production of a Degenerate Gas of 6Li: Characterization of Degeneracy. PhD thesis, Duke University, 2002.

[69] M. E. Gehm. Preparation of an Optically-trapped Degenerate Fermi gas of 6Li: Finding the Route to Degeneracy. PhD thesis, Duke University, 2003.

[70] J. M. Kinast. Thermodynamics and Superfluidity of A Strongly Interacting Fermi Gas. PhD thesis, Duke University, 2006.

[71] B. E. Clancy. Hydrodynamics of A Roatating Strongly Interacting Fermi Gas. PhD thesis, Duke University, 2008.

[72] L. Luo. Entropy and Superfluid Critical Parameters of a Strongly Interacting Fermi gas. PhD thesis, Duke University, 2008.

[73] J. Joseph. Precision Measurement of the Sound Velocity In an Ultracold Fermi Gas Through the Bec-Bcs Crossover. PhD thesis, Duke University, 2008.

[74] J. Carlson, S.-Y. Chang, V. R. Pandharipande, and K. E. Schmidt. Superfluid Fermi gases with large scattering length. *Phys. Rev. Lett.*, 91:050401, 2003

[75] S. Y. Chang, V. R. Pandharipande, J. Carlson, and K. E. Schmidt. Quantum Monte-Carlo studies of superuid Fermi gases. *Phys. Rev. A.*, 70:043602, 2004

[76] T. Schäfer and D. Teaney. Nearly Perfect Fluidity: From Cold Atomic Gases to Hot Quark Gluon Plasma. *Rept. Prog. Phys.*, 72:126001, 2009

[77] T. Takekoshi and R. Knize. CO_2 laser trap for cesium atoms. *Opt. Lett.*, 21, p. 77,1996

[78] G. Zerza L. Windholz, M. Musso and H. Jäger. Precise Stark-effct investigations of the lithium D1 and D2 lines. *Phys. Rev. A*, 46:5812, 1992

[79] H. Song, S.A. Bass, U.W. Heinz, T. Hirano and C. Shen. 200 A GeV Au+Au collisions serve a nearly perfect quark-gluon liquid. http://arxiv.org/abs/1011.2783

[80] E. M. Lifshitz and L. P. Pitaevskii. Physical Kinetics. Pergamon, New York, 1981.

[81] S. G. Brush. "The kind of motion we call heat". North Holland, 1986.

[82] J. T. Stewart, J. P. Gaebler, C. A. Regal, and D. S. Jin. Potential energy of a 40K Fermi gas in the BCS-BEC crossover. *Phys. Rev. Lett.*, 97:220406, 2006

[83] M. J. H. Ku, A. T. Sommer, L. W. Cheuk, M. W. Zwierlein. Revealing the Superfluid Lambda Transition in the Universal Thermodynamics of a Unitary Fermi Gas. *Science*, 335:563, 2011.

[84] M. Bertenstein, A. Altmeyer, S. Riedl, R. Geursen, S. Jochim, C. Chin, J. Hecker Denshlag, R. Grimm, A. simoni, E. Tiesinga, C.J. Williams, and P. S. Julienne. Percise Determination of 6Li Cold Collision Parameters by Radio Frequency Spectroscopy and Weakly Bound Molecules. *Phys. Rev. Lett.*, 94:103201, 2005

[85] Kevin E. Strecker, Guthrie B. Partridge, and Randall G. Hulet Conversion of an Atomic Fermi Gas to a Long-Lived Molecular Bose Gas. *Phys. Rev. Lett.*, 91:080406, 2003

[86] Aurel. Bulgac and George F. Bertsch. Collective Oscillations of a Trapped Fermi Gas near the Unitary Limit. *Phys. Rev. Lett.*, 94:070401, 2005.

[87] J. E. Thomas. Class Notes of the Advacned Quantum Optics Physics Department, Duke University, 2011.

[88] L. D. Landau and E. M. Lifshitz. Fluid Mechanics 2nd Edition. Pergamon, New York, 1987.

[89] Richard. L. Liboff. Quantum Mechanics 4th Edition. Addison Wesley, 2003.

[90] J. E. Thomas. Energy measurement and virial theorem for confined universal Fermi gases. *Phys. Rev. A*, 78:013630, 2008.

[91] F. Werner. Virial theorems for trapped cold atoms. *Phys. Rev. A*, 78:025601, 2008.

[92] A. Sommer, M. Ku, G. Roati, M. W. Zwierlein. Universal spin transport in a strongly interacting Fermi gas. *Nature*, 472:201, 2011.

[93] H. Wu and J. E. Thomas. Optical control of Feshbach resonances in Fermi gases using molecular dark states. *Phys. Rev. Lett.*, 108, 010401, 2012.

[94] V. Dribinski, A. Ossadtchi, V. Mandelshtam and H. Reisler. Reconstruction of Abel-transformable images: The basis-set expansion Abel transform method. *Rev. Sci. Inst.*, 73:2634, 2002.

[95] E. L. Hazlett, Y. Zhang, R. W. Stites, K. M. O'Hara Realization of a Resonant Fermi Gas with a Large Effective Range. http://arxiv.org/abs/1112.5977.

[96] Markus Mueller, Joerg Schmalian, Lars Fritz. Graphene - a nearly perfect fluid. *Phys. Rev. Lett.*, 103, 025301, 2009.

[97] E. Vogt, M. Feld, B. Frohlich, D. Pertot, M. Koschorreck, M. Köhl. Scale invariance and viscosity of a two-dimensional Fermi Gas. *Phys. Rev. Lett.*, 108, 070404 , 2012.

[98] T. Schäfer. Shear viscosity and damping of collective modes in a two-dimensional Fermi gas. http://arxiv.org/abs/1111.7242.

[99] G. M. Bruun. Shear viscosity and spin diffusion coefficient of a two-dimensional Fermi gas. http://arxiv.org/abs/1112.2395.

[100] The method of exciting the relative motion between the two fluids was from John Thomas, North Carolina State University.

[101] F. Reif. Fundamentals of statistical and thermal physics. McGraw-Hill, New York, 1987.

Biography

Chenglin Cao was born September 22, 1983 in Suzhou, China. In 2002, he graduated from the Suzhou high school of Jiangsu province. Later that year, he entered Nanjing University to pursue a physics major. After graduated with honor in May 2006, he came to the USA and enrolled at Duke University in August 2006. After joining Dr.John Thomas's research group on ultra-cold Fermi gases, he contributed to the measurement of quantum viscosity in a unitary Fermi gas. He was awarded an A.M. in physics in May 2011. He also received the Walter Gordy Fellowship in October 2011 before graduating with a Ph.D. in May 2012.